

# **Numerical Investigation of the Chemistry of the Pore Solution in the Mill Scale Crevices of Carbon Steel Rebar**

by

**Kosta Karadakis**

This thesis is submitted to the Faculty of Graduate Studies and Research in  
partial fulfilment of requirements for the degree of

**Master of Applied Science**

Department of Civil and Environmental Engineering

Carleton University

Ottawa, Ontario, Canada

The Master of Applied Science in Civil Engineering is a joint program with the  
University of Ottawa, administered by Ottawa-Carleton Institute for Civil Engineering

© 2010, Kosta Karadakis



Library and Archives  
Canada

Published Heritage  
Branch

395 Wellington Street  
Ottawa ON K1A 0N4  
Canada

Bibliothèque et  
Archives Canada

Direction du  
Patrimoine de l'édition

395, rue Wellington  
Ottawa ON K1A 0N4  
Canada

*Your file* *Votre référence*  
ISBN: 978-0-494-63464-6  
*Our file* *Notre référence*  
ISBN: 978-0-494-63464-6

**NOTICE:**

The author has granted a non-exclusive license allowing Library and Archives Canada to reproduce, publish, archive, preserve, conserve, communicate to the public by telecommunication or on the Internet, loan, distribute and sell theses worldwide, for commercial or non-commercial purposes, in microform, paper, electronic and/or any other formats.

The author retains copyright ownership and moral rights in this thesis. Neither the thesis nor substantial extracts from it may be printed or otherwise reproduced without the author's permission.

---

In compliance with the Canadian Privacy Act some supporting forms may have been removed from this thesis.

While these forms may be included in the document page count, their removal does not represent any loss of content from the thesis.

**AVIS:**

L'auteur a accordé une licence non exclusive permettant à la Bibliothèque et Archives Canada de reproduire, publier, archiver, sauvegarder, conserver, transmettre au public par télécommunication ou par l'Internet, prêter, distribuer et vendre des thèses partout dans le monde, à des fins commerciales ou autres, sur support microforme, papier, électronique et/ou autres formats.

L'auteur conserve la propriété du droit d'auteur et des droits moraux qui protègent cette thèse. Ni la thèse ni des extraits substantiels de celle-ci ne doivent être imprimés ou autrement reproduits sans son autorisation.

---

Conformément à la loi canadienne sur la protection de la vie privée, quelques formulaires secondaires ont été enlevés de cette thèse.

Bien que ces formulaires aient inclus dans la pagination, il n'y aura aucun contenu manquant.

  
**Canada**

## Abstract

The variability and uncertainty associated with chloride thresholds can be partly explained by the surface conditions of carbon steel rebar, in particular, by the presence of mill scale on the steel surface. It has been suggested in the literature that pore solution in the crevices between mill scale and steel surface may be different from that of the bulk pore solution, and this difference may create the necessary conditions for the breakdown of the passive film. To test this hypothesis, a numerical investigation was carried out using a non-linear transient finite element algorithm, which involved the solution of coupled extended Nernst-Planck and Poisson's equations under constraints imposed by the chemical reactions and equilibrium requirements in a domain that represented typical mill scale cracks and crevices. The numerical simulations showed that the chemistry of the pore solution, in particular pH and the chloride-to-hydroxide concentration ratio,  $Cl^-/OH^-$ , within mill scale crevices provided more favourable conditions for depassivation than that of the bulk pore solution.

## Table of Contents

Title Page .....	i
Abstract.....	ii
Table of Contents.....	iii
Acknowledgements.....	vi
List of Tables .....	vii
List of Symbols.....	xvi
1) Introduction.....	1
1.1 Background.....	3
1.2 Objectives and scope.....	5
1.3 Organization of the thesis .....	7
2) Literature Review.....	10
2.1 Chloride threshold of carbon steel rebar .....	10
2.2 Passive current density of carbon steel rebar .....	16
2.3. Numerical models of localized corrosion .....	27
2.3.1 Sharland et al. (1989).....	27
2.3.2 Harb and Alkire (1991).....	28
2.3.3 Chang et al. (2000).....	30
2.3.4 Chin and Sabde (2000).....	32
2.3.5 Vankeerberghen (2004) .....	34
2.3.6 Heppner et al. (2004) .....	36

2.3.7 Summary .....	37
2.4. Key observations obtained from the literature review .....	38
3) Modelling Theory and Its Implementation .....	40
3.1 Governing equations .....	40
3.2 Chemical reaction constraints .....	45
3.3 Initial conditions .....	48
3.4 Domain and boundary conditions .....	53
3.4.1 Boundary conditions for the extended Nernst-Planck equations .....	55
3.4.2 Boundary conditions for the Poisson equation .....	58
3.5 Transport properties .....	59
3.6 Solution procedure .....	60
3.7 Results from a typical simulation .....	61
3.8 Effect of chemical activity on the simulations .....	67
4) Numerical Analysis and Discussion .....	71
4.1 Simulations in chloride-free pore solution .....	71
4.1.1 Results and discussion .....	73
4.1.1.1 Effect of passive current density .....	73
4.1.1.2 Effect of diffusion coefficient .....	77
4.1.1.3 Analysis in the CP solution .....	81
4.1.1.4 Summary .....	82
4.2 Simulations in pore solutions with chlorides – constant $i_p$ .....	83
4.2.1 Results and discussion .....	87
4.2.1.1 Effect of the mill scale crack thickness and crevice length .....	87

4.2.1.2	Effect of passive current density.....	91
4.2.1.3	Effect of chloride in the bulk concrete pore solution.....	97
4.2.1.4	Effect of the diffusion coefficients of the species.....	104
4.2.1.5	Summary .....	107
4.3	Simulations in pore solutions with chlorides – variable $i_p$ .....	108
4.3.1	Results and discussion .....	113
4.3.1.1	Effect of current density after threshold, $i_t$ .....	113
4.3.1.2	Effect of crevice length.....	118
4.3.1.3	Effect of the amount of chloride in the bulk concrete pore solution .....	123
4.3.1.4	Effect of the diffusion coefficients of the species.....	128
4.3.1.5	Summary .....	131
5)	Conclusions and Future Work .....	133
5.1	Conclusions.....	134
5.2	Recommendations for future work .....	136
6)	References.....	139
Appendix A:	Solution Process of COMSOL™ .....	151
Appendix B:	Model Implementation in COMSOL™ .....	156
Appendix C:	Mesh Analysis .....	169
C.1	Simulations with chemical activity effects included.....	169
C.2	Simulations with chemical activity effects ignored .....	175
C.3	Concluding remarks .....	181

## **Acknowledgements**

I would like to sincerely thank my supervisor Professor O. Burkan Isgor for his continued support and patience throughout this research. His positive attitude was a relief, especially during the difficult times, and his attention to detail made this thesis what it is. For all of his help, I am truly thankful.

I would also like to thank my colleague Mr. Pouria Ghods for his numerous contributions to this thesis. His willingness to help did not go unnoticed.

Lastly, I would like to thank my family for their love and encouragement during this research. They were always there to cheer me up when I needed it and they provided me with everything I needed in order to achieve, without asking anything in return.

## List of Tables

<b>Table 2.1:</b> Summary of reported chloride threshold values (taken from Angst et al. 2009). Abbreviations are given in Table 2.2.....	15
<b>Table 2.2:</b> Abbreviations in Table 2.1 and Figure 2.1 (taken from Angst et al. 2009)....	15
<b>Table 2.3:</b> Summary of experimental studies on the passive current density <sup>(1)</sup> .....	26
<b>Table 3.1:</b> Valence and radii of the ionic species modelled in the study (Dean 1999)....	41
<b>Table 3.2:</b> Concentrations, activity coefficients and activities of species in the bulk CH solution.....	52
<b>Table 3.3:</b> Concentrations, activity coefficients and activities of species in the bulk CP solution.....	53
<b>Table 3.4:</b> Transport properties of all species in the concrete pore solutions.....	60
<b>Table 3.5:</b> Constants and analysis parameters used in the numerical model.....	61
<b>Table 3.6:</b> Bulk CH solution when chemical activity effects were ignored (mol/m <sup>3</sup> )....	68
<b>Table 4.1:</b> Dimensions of the domain for the simulations carried out in Section 4.1.....	72
<b>Table 4.2:</b> Input parameters for all simulation cases in Section 4.1.....	73
<b>Table 4.3:</b> Input parameters for all simulation cases carried out in Section 4.2.....	86
<b>Table 4.4:</b> Input parameters for all simulations carried out in Section 4.3.....	112
<b>Table C.1:</b> Comparison of finite element meshes when activity effects were included.	171
<b>Table C.2:</b> Concentrations at the tip of the crevice when activity effects were included .....	175
<b>Table C.3:</b> Mesh comparison properties when activity effects were ignored.....	176
<b>Table C.4:</b> Concentrations at the tip of the crevice when activity effects were ignored	177
<b>Table C.5:</b> Mesh comparison when activity effects were ignored.....	180

## List of Figures

<b>Figure 1.1.</b> SEM cross-section images of turned-and-polished and as-received rebar samples: (a) oxide-free surface of a turned-and-polished rebar specimen; (b) low magnification image of as-received specimens before chloride exposure; (c) high magnification image of as-received sample before chloride exposure; (d) as-received rebar specimen after immersion in chloride-contaminated concrete pore solution showing corrosion initiation (area “D”) under the mill scale (courtesy of Ghods et al. 2009c). .....	4
<b>Figure 1.2.</b> Pourbaix diagram for iron-water system at 25°C (reproduced from Esmaeilpoursaee 2007) .....	7
<b>Figure 2.1.</b> Summary of reported chloride threshold values (taken from Angst et al. 2009). Abbreviations are given in Table 2.2.....	14
<b>Figure 2.2.</b> Variation of the current density of grit blasted steel rods at different Cl <sup>-</sup> /OH <sup>-</sup> in cement paste (taken from Lambert et al. 1991).....	19
<b>Figure 2.3.</b> Corrosion current density of as-received carbon steel rods in saturated Ca(OH) <sub>2</sub> solutions with different concentrations of chloride ion (taken from Moreno et al. 2004).....	20
<b>Figure 2.4.</b> Corrosion current density of carbon steel in (a) mortar (b) synthetic pore solution with a pH > 13 (taken from Poursaee and Hansson 2007).....	23
<b>Figure 2.5.</b> Anodic polarization curve of (a) as-received carbon steel in different synthetic pore solutions (taken from Ghods et al. 2009e) (b) polished carbon steel in simulated pore solution with pH = 13.3 (reproduced from Ghods et al. 2008a). .....	24

<b>Figure 2.6.</b> Finite element domain used to simulate crevice corrosion (taken from Sharland et al.1989). .....	28
<b>Figure 2.7.</b> Finite element domain used to simulate the dissolution of a hemispherical corrosion pit (taken from Harb and Alkire 1991). .....	29
<b>Figure 2.8.</b> Finite element domain used to simulate the initiation stage of crevice corrosion (reproduced from Chang et al. 2000). .....	31
<b>Figure 2.9.</b> Numerical model of an idealized crevice formed between the metal surface and coating (taken from Chin and Sabde 2000). .....	33
<b>Figure 2.10.</b> Schematic representation of the modelled crevice formed between a quartz disk at the top and an aluminium disk at the bottom. $H$ is the height of the crevice, $R_o$ is the radius and $C_L$ is the centreline representing the axis of cylindrical symmetry (taken from Vankeerberghen 2004). .....	35
<b>Figure 2.11.</b> Finite element domain used to simulate the initiation stage of crevice corrosion. The small arrows represent metal ion dissolution. (taken from Heppner et al. 2004). .....	37
<b>Figure 3.1.</b> The solution domain representing the crack in the mill scale and the crevice between the surface of steel and mill scale. ....	54
<b>Figure 3.2.</b> The activities of the ionic species and the concentration of the gaseous species along the center of the mill scale crack (boundary 2) and along the steel surface (boundary 3) when steady-state conditions are reached. ....	65
<b>Figure 3.3.</b> Time plots at the tip of the crevice (point A) for: (a) hydroxide activity, chloride activity and (b) oxygen concentration of species. For clarity, only some of the data points are shown in the plots. ....	66

**Figure 3.4.** Variation of the pH and the  $\text{Cl}^-/\text{OH}^-$  ratio along the center of the mill scale crack (boundary 2) and along the steel surface (boundary 3) when steady-state conditions are reached. For clarity, only some of the data points are shown in the plots..... 67

**Figure 3.5.** pH and  $\text{Cl}^-/\text{OH}^-$  in CH solution along boundaries 2 and 3 (from point B to point A) after steady-state conditions are reached: (a) with chemical activity effects included; (b) with chemical activity effects ignored. For clarity, only some of the data points are shown in the plots..... 70

**Figure 4.1.** The pH profile along boundaries 2 and 3 (from point B to point A) for different passive current densities ( $i_p$ ) after steady-state conditions are reached at  $t = 10^9$  s. Diffusion coefficients linearly decrease from  $D_{max} = 10^{-9}$  to  $D_{min} = 10^{-13}$   $\text{A/m}^2$  as  $\text{Fe}(\text{OH})_{2(s)}$  builds up in the pore solution. For clarity, only some of the data points are shown in the plots..... 74

**Figure 4.2.** pH at point A over time with diffusion coefficients that linearly decrease from  $D_{max} = 10^{-9}$  to  $D_{min} = 10^{-13}$   $\text{A/m}^2$  as  $\text{Fe}(\text{OH})_{2(s)}$  builds up in the pore solution for various passive current densities ( $i_p$ ). For clarity, only some of the data points are shown in the plots. .... 77

**Figure 4.3.**  $\text{Fe}(\text{OH})_{2(s)}$  concentration for different diffusion coefficients that linearly decrease from  $D_{max}$  to  $D_{min}$  as solid build up in the pore solution: (a) at point A over time; (b) across the midpoint (C-C) of the crevice length at  $t = \sim 2.7 \times 10^4$  s; (c) across the midpoint (D-D) of the mill scale crack length at  $t = \sim 1.4 \times 10^3$  s. For clarity, only some of the data points are shown in the plots..... 79

**Figure 4.4.** pH at point A over time for different diffusion coefficients that linearly decrease from  $D_{max}$  to  $D_{min}$  as  $\text{Fe}(\text{OH})_{2(s)}$  builds up in the pore solution. For clarity, only some of the data points are shown in the plots. .... 80

**Figure 4.5.** pH profile along boundaries 2 and 3 (from point B to point A) after steady-state conditions are reached for different diffusion coefficients that linearly decrease from  $D_{max}$  to  $D_{min}$  as  $\text{Fe}(\text{OH})_{2(s)}$  builds up in the pore solution. For clarity, only some of the data points are shown in the plots. .... 81

**Figure 4.6.** pH at point A over time with diffusion coefficients that linearly decrease from  $D_{max} = 10^{-9}$  to  $D_{min} = 10^{-13}$   $\text{A}/\text{m}^2$  as  $\text{Fe}(\text{OH})_{2(s)}$  builds up in the pore solution for the CH solution with pH  $\sim 12.5$  and CP solution with pH  $\sim 13.5$ . For clarity, only some of the data points are shown in the plots. .... 82

**Figure 4.7.** Assumed depassivation criterion for the simulations carried out in Section 4.2. It was assumed that the passive current density remains constant until pH drops below 10; afterwards, the current density is assumed to sharply increase to the active corrosion rate that is observed after pit formation. In the figure the threshold of 3 was chosen arbitrarily. .... 84

**Figure 4.8.** pH and  $\text{Cl}^-/\text{OH}^-$  for a varying crack thickness along boundaries 2 and 3 (from point B to point A) after steady-state conditions are reached. For clarity, only some of the data points are shown in the plots. .... 89

**Figure 4.9.** pH and  $\text{Cl}^-/\text{OH}^-$  for crevice length ( $c/2$ ) of  $1.5 \times 10^{-3}$  m along boundaries 2 and 3 (from point B to point A) after steady-state conditions are reached. Other two crevice lengths (*i.e.*,  $5 \times 10^{-5}$  and  $5 \times 10^{-4}$  m) are not shown because of negligible changes in pH. .... 91

**Figure 4.10.** pH and  $\text{Cl}^-/\text{OH}^-$  at various passive current densities,  $i_p$ , in CH solutions with conductive mill scale surfaces along boundaries 2 and 3 (from point B to point A) after steady-state conditions are reached. For clarity, only some of the data points are shown in the plots. .... 93

**Figure 4.11.** pH and  $\text{Cl}^-/\text{OH}^-$  at various passive current densities,  $i_p$ , in CP solutions with conductive mill scale surfaces along boundaries 2 and 3 (from point B to point A) after steady-state conditions are reached. For clarity, only some of the data points are shown in the plots. .... 94

**Figure 4.12.** pH and  $\text{Cl}^-/\text{OH}^-$  for conductive and non-conductive mill scale surfaces along boundaries 2 and 3 (from point B to point A) after steady-state conditions are reached. For clarity, only some of the data points are shown in the plots. .... 96

**Figure 4.13.** pH and  $\text{Cl}^-/\text{OH}^-$  at different chloride activities in the bulk CH solution: (a) along boundaries 2 and 3 (from point B to point A) after steady-state conditions are reached (b) at point A over time. For clarity, only some of the data points are shown in the plots. .... 99

**Figure 4.14.** pH and  $\text{Cl}^-/\text{OH}^-$  at different chloride activities in the bulk CP solution: (a) along boundaries 2 and 3 (from point B to point A) after steady-state conditions are reached (b) at point A over time. For clarity, only some of the data points are shown in the plots. .... 103

**Figure 4.15.** pH and  $\text{Cl}^-/\text{OH}^-$  for different diffusion coefficients that linearly decrease from  $D_{max}$  to  $D_{min}$  as solid compounds expand in the pore solution: (a) along boundaries 2 and 3 (from point B to point A) after steady-state conditions are

reached (b) at point A over time. For clarity, only some of the data points are shown in the plots. .... 106

**Figure 4.16.** Assumed depassivation criterion for the simulations carried out in Section 4.3. It was assumed that the passive current density remains constant until a  $\text{Cl}^-/\text{OH}^-$  threshold of 3, after which the current density increases to a steady value until pH drops below 10; afterwards, the current density is assumed to sharply increase to active corrosion rate..... 110

**Figure 4.17.** pH and  $\text{Cl}^-/\text{OH}^-$  in CH solutions (soln. 1 in Table 3.2) along boundaries 2 and 3 (from point B to point A) for a passive current density that linearly increases from  $i_p = 1 \times 10^{-3}$  to  $i_t = 1.7 \times 10^{-2}$   $\text{A/m}^2$  on the steel surface at different assumed ranges of  $\text{Cl}^-/\text{OH}^-$ . For clarity, only some of the data points are shown in the plots. .... 111

**Figure 4.18.** pH and  $\text{Cl}^-/\text{OH}^-$  at various current densities after threshold,  $i_t$ , in CH solutions: (a) along boundaries 2 and 3 (from point B to point A) (b) at point A over time. For clarity, only some of the data points are shown in the plots. .... 116

**Figure 4.19.** pH and  $\text{Cl}^-/\text{OH}^-$  at various current densities after threshold,  $i_t$ , in CP solutions: (a) along boundaries 2 and 3 (from point B to point A) (b) at point A over time. For clarity, only some of the data points are shown in the plots. .... 117

**Figure 4.20.** pH and  $\text{Cl}^-/\text{OH}^-$  for varying crevice lengths in CH solutions along boundaries 2 and 3 (from point B to point A). For clarity, only some of the data points are shown in the plots..... 121

**Figure 4.21.** pH and  $\text{Cl}^-/\text{OH}^-$  for varying crevice lengths in CP solutions along boundaries 2 and 3 (from point B to point A). For clarity, only some of the data points are shown in the plots..... 122

**Figure 4.22.** pH and  $\text{Cl}^-/\text{OH}^-$  at different chloride activities in CH solution: (a) along boundaries 2 and 3 (from point B to point A) (b) at point A over time. For clarity, only some of the data points are shown in the plots. .... 125

**Figure 4.23.** pH and  $\text{Cl}^-/\text{OH}^-$  at different chloride activities in CP solution: (a) along boundaries 2 and 3 (from point B to point A) (b) at point A over time. For clarity, only some of the data points are shown in the plots. .... 127

**Figure 4.24.** pH and  $\text{Cl}^-/\text{OH}^-$  for different diffusion coefficients in CH solutions that linearly decrease from  $D_{max}$  to  $D_{min}$  as solid compounds expand in the pore solution along boundaries 2 and 3 (from point B to point A). For clarity, only some of the data points are shown in the plots. .... 130

**Figure 4.25.** pH and  $\text{Cl}^-/\text{OH}^-$  for different diffusion coefficients in CP solutions that linearly decrease from  $D_{max}$  to  $D_{min}$  as solid compounds expand in the pore solution along boundaries 2 and 3 (from point B to point A). For clarity, only some of the data points are shown in the plots. .... 131

**Figure C.1.** Mesh comparison of four different mesh types along the center of the mill scale crack (boundary 2) and along the steel surface (boundary 3) when steady-state conditions are reached for: (a)  $\text{OH}^-$  (b)  $\text{Fe}^{2+}$  (c)  $\text{Ca}^{2+}$ . Chemical activity effects were included. For clarity, only some of the data points are shown in the plots..... 173

**Figure C.2.** Mesh comparison of four different mesh types along the center of the mill scale crack (boundary 2) and along the steel surface (boundary 3) when steady-state conditions are reached for: (a)  $\text{Cl}^-$  (b)  $\text{Na}^+$  (c)  $\text{O}_2$ . Chemical activity effects were included. For clarity, only some of the data points are shown in the plots. 174

**Figure C.3.** Mesh comparison of five different mesh types along the center of the mill scale crack (boundary 2) and along the steel surface (boundary 3) when steady-state conditions are reached for: (a)  $\text{OH}^-$  (b)  $\text{Fe}^{2+}$  (c)  $\text{Ca}^{2+}$ . Activity effects were ignored. For clarity, only some of the data points are shown in the plots. .... 178

**Figure C.4.** Mesh comparison of five different mesh types along the center of the mill scale crack (boundary 2) and along the steel surface (boundary 3) when steady-state conditions are reached for: (a)  $\text{Cl}^-$  (b)  $\text{Na}^+$  (c)  $\text{O}_2$ . Activity effects were ignored. For clarity, only some of the data points are shown in the plots. .... 179

**Figure C.5.** Mesh comparison of two different mesh types along the center of the mill scale crack (boundary 2) and along the steel surface (boundary 3) when steady-state conditions are reached for  $\text{OH}^-$  species and activity effects were ignored. For clarity, only some of the data points are shown in the plots. .... 181

**Figure C.6.** Mesh used for all simulations in this thesis. Shaded colour scheme ranges from 1 (high quality) to 0 (low quality). .... 182

## List of Symbols

$A$	= temperature dependent parameter
$a_i$	= radii of species in the ionic state (m)
$B$	= temperature dependent parameter
$c$	= crevice length (m)
$c_i$	= concentration of species in the ionic or in the gaseous state ( $\text{mol/m}^3$ )
$c_{is}$	= concentration of species in the solid state ( $\text{mol/m}^3$ )
$\text{Cl}^-/\text{OH}^-$	= chloride-to-hydroxide concentration ratio
$D_i$	= diffusion coefficient for the species ( $\text{m}^2/\text{s}$ )
$D_{max}$	= maximum diffusion coefficient at $[\text{Fe}(\text{OH})_{2(s)}] = 0 \text{ mol/m}^3$ ( $\text{m}^2/\text{s}$ )
$D_{min}$	= minimum diffusion coefficient at $[\text{Fe}(\text{OH})_{2(s)}] = 37,840 \text{ mol/m}^3$ ( $\text{m}^2/\text{s}$ )
$e_0$	= charge of one electron ( $1.602 \times 10^{-19} \text{ C}$ )
$F$	= Faraday's constant (96,488 C/mol)
$I$	= ionic strength ( $\text{mol/m}^3$ )
$i$	= current density ( $\text{A/m}^2$ )
$i_p$	= passive current density ( $\text{A/m}^2$ )
$i_t$	= current density after threshold ( $\text{A/m}^2$ )
$K_{sp1}$	= solubility product constant of $\text{Ca}(\text{OH})_{2(s)}$ ( $5500 \text{ mol}^3/\text{m}^9$ )
$K_{sp2}$	= solubility product constant of $\text{Fe}(\text{OH})_{2(s)}$ ( $4.87 \times 10^{-8} \text{ mol}^3/\text{m}^9$ )
$l$	= mill scale crack length (m)
LPR	= linear polarisation resistance
$\mathbf{N}_i$	= total flux of species (vector)
$\mathbf{n}$	= directional normal vector to the boundary

$n_e$	= number of electrons exchanged in a reaction
$n_s$	= total number of ionic species
$R$	= ideal gas constant (8.3143 J/mol/K)
$r$	= radial direction
$T$	= temperature (K)
$t$	= time (s)
$t_c$	= crevice thickness (m)
$t_l$	= mill scale crack thickness (m)
$u_i$	= mobility of the species ( $\text{m}^2 \cdot \text{s}^{-1} \cdot \text{V}^{-1}$ )
$v_i$	= velocity of the net flow of species (m/s)
$z_i$	= valence of the ionic species
$\Gamma_i$	= boundary of the domain
$\gamma_i$	= chemical activity coefficient for various ionic species
$\varepsilon$	= permittivity of the medium ( $7.092 \times 10^{-10} \text{ C}^2/\text{N}/\text{m}^2$ )
$\varepsilon_0$	= permittivity of the vacuum ( $8.854 \times 10^{-12} \text{ C}^2/\text{N}/\text{m}^2$ )
$\varepsilon_r$	= dielectric constant of water (80.1)
$\bar{\mu}_i$	= electrochemical potential
$\mu_i^\circ$	= chemical potential in the standard state
$\phi$	= electric potential (V)

## 1) Introduction

The corrosion of carbon steel rebar in concrete is an electrochemical process, in which rebar provides a path for electrons to travel from anodic sites, where oxidation reactions take place, to cathodic sites, where reduction reactions occur (Perez 2004). The rate of corrosion can be determined from current per unit anodic area; *i.e.*, by the anodic current density. In the highly alkaline environment ( $\text{pH} > 13$ ) provided by concrete, the products of this electrochemical process form a protective oxide film (*i.e.*, passive film) on the rebar surface that keeps the corrosion rates low, typically below  $10^{-3}$  mm/yr (Poursaeed and Hansson 2007). As long as the chemical conditions that lead to the formation of the passive film remain relatively constant, the corrosion rate will also remain at these low levels and will maintain a stable and protective passive film on the rebar surface through a passive current density. The partial or complete loss of the passive film, known as depassivation, may lead to current densities that are orders of magnitude larger than the passive current density, hence, may result in excessive metal loss from the rebar.

Chlorides are well known to cause depassivation if they are present in concrete in sufficient concentrations above a threshold concentration (*i.e.*, chloride threshold). Chloride thresholds in concrete are generally represented as chloride-to-hydroxide concentration ratio,  $\text{Cl}^-/\text{OH}^-$ , since they have been documented to be related to the alkalinity of the pore solution (Gofni and Andrade 1990, Hansson and Sørensen 1990). Unfortunately, reported values of chloride thresholds for carbon steel rebar in concrete cover a wide range and have a large degree of uncertainty (Alonso et al. 2000, Ann and

Song 2007, Angst et al. 2009). Currently, there is no comprehensive explanation for the variability in measured chloride thresholds, but, as reported by Ghods et al. (2009d), they are believed to depend on a large number of factors including the chemical composition of the pore solution, the properties of the rebar-concrete interface, chloride binding in concrete, and oxygen availability around the reinforcement. In addition, even when similar testing procedures, materials and exposure conditions are used in the experiments, the chloride thresholds for carbon steel rebar in concrete still show variability: Ghods et al. (2009d) proposed that this variability might be partially due to the surface conditions of rebar, in particular, the presence of mill scale on the steel surface.

A number of researchers (Mammoliti et al. 1996, Alonso et al. 2000, Li and Sagüés 2001, Pillai and Trejo 2005, Mohammed and Hamada 2006, Manera et al. 2008) have investigated the effect of rebar surface conditions on chloride thresholds, and it has been widely reported that higher chloride thresholds were observed for rebars with modified surfaces (*i.e.*, with no mill scale after sandblasting, polishing or pickling, as shown in Figure 1.1a), than those in as-received conditions with mill scale. For example, Mammoliti (1995) reported that corrosion did not initiate in highly-polished rebar even after the specimens were exposed to chloride concentrations in excess of that is typically found in sea water. In addition, as reported by Ghods et al. (2009d), modifying the rebar surface also leads to reduced variability and reduced fluctuations in electrochemical measurements, which can be explained by the fact that modified surfaces are more uniformly the same everywhere, whereas as-received surfaces are locally much more diverse and complex due to the presence of mill scale. These results suggest that the

variability associated with the reported chloride thresholds may be attributed to the variability in mill scale properties resulting from the variability in manufacturing.

### **1.1 Background**

Mill scale is the iron oxide layer that forms on the rebar surface during the hot rolling process of steel production (Roberts 1983). Scanning electron microscopic (SEM) studies by Ghods et al. (2009c) have shown that this oxide layer is poorly and non-uniformly attached to the rebar surface, and it contains randomly distributed transverse cracks that link the free surface of the mill scale to the underlying crevices on the steel surface, as shown in Figures 1.1b and 1.1c. When as-received rebar surfaces are exposed to concrete pore solution contaminated with chlorides, these mill scale cracks serve as pathways for concrete pore solution to reach the surface of steel; hence allow ion exchange between the pore solution and the crevices through electrical migration and diffusion. Over time, the chemical composition of the pore solution within the crevices might begin to differ from that of the bulk solution through a process similar to the suggested mechanisms of typical crevice corrosion (Jones 1996, Fontana 1986). Figure 1.1d illustrates pit initiation along a crevice between mill scale and steel after an as-received rebar specimen was exposed to a simulated pore solution contaminated with chlorides. Ghods et al. (2009c) suggested that the concrete pore solution chemistry within mill scale cracks and crevices may change from that of the bulk pore solution contaminated with chlorides; thus, may provide more favourable conditions for depassivation and pit nucleation on the rebar surface. Here a brief description of one of the proposed mechanisms explaining this phenomenon, as provided by Ghods et al. (2009c), is provided.

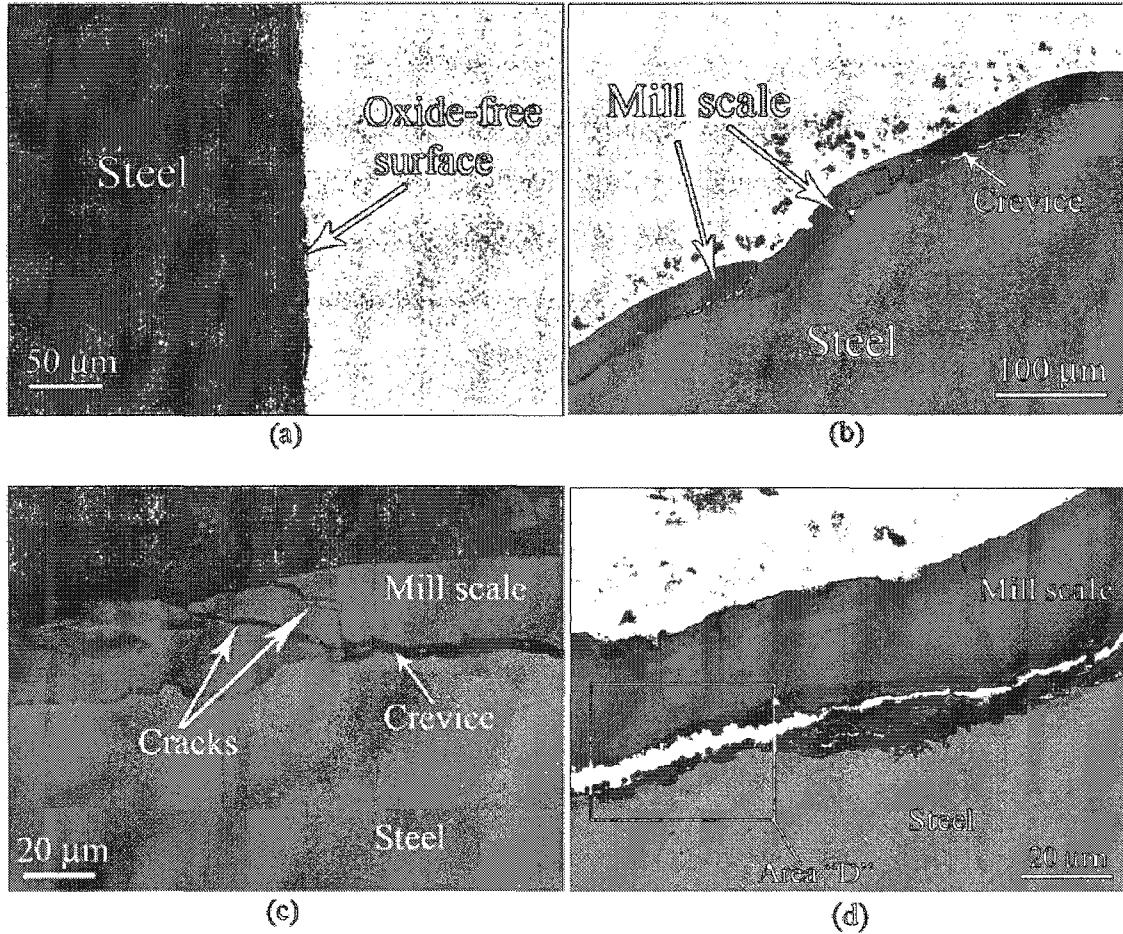


Figure 1.1. SEM cross-section images of turned-and-polished and as-received rebar samples: (a) oxide-free surface of a turned-and-polished rebar specimen; (b) low magnification image of as-received specimens before chloride exposure; (c) high magnification image of as-received sample before chloride exposure; (d) as-received rebar specimen after immersion in chloride-contaminated concrete pore solution showing corrosion initiation (area "D") under the mill scale (courtesy of Ghods et al. 2009c).

The effect of mill scale on the corrosion initiation mechanism of as-received rebar can be divided into two stages. In the first stage, due to the anodic reaction at the surface of steel, iron dissolves into the concrete pore solution. The rate of iron dissolution before depassivation is controlled by the passive current density. At the same time, in the presence of oxygen, the cathodic reaction in the form of oxygen reduction also takes place on the steel surface. Since the solubility of iron hydroxide in alkaline solutions is

very low (e.g. for  $\text{Fe}(\text{OH})_{2(s)}$ ,  $K_{sp} \sim 4.87 \times 10^{-8} \text{ mol}^3/\text{m}^9$ ) (Dean 1999), iron ions react with hydroxides and precipitate as iron hydroxide. During this stage, the concentrations of anions and cations in the crevice are the same as the concentrations in the bulk concrete pore solution. In particular,  $\text{Cl}^-/\text{OH}^-$  of the bulk solution and of the solution in the crevice are identical. As the anodic and cathodic reactions proceed, oxygen that is consumed in the cathodic reaction cannot be replenished by the transport of oxygen from the bulk solution since consumption rates are faster than the compensation rates; therefore, after a while, oxygen is depleted in the crevice.

Following the depletion of oxygen the second stage starts. In this stage, the cathodic reaction ceases in the crevice but continues to take place outside the crevice; hence, hydroxide is no longer produced inside the crevice. Meanwhile, due to the continuous formation of solid iron hydroxide, the concentration of hydroxide decreases inside the crevice, while an electrochemical gradient forms between the bulk and crevice pore solutions. The requirement of electro-neutrality dictates that negatively charged ions (e.g. chloride) migrate from the bulk solution into the crevice via cracks in the mill scale; therefore, the chloride concentration inside the crevice starts increasing as the hydroxide concentration decreases, causing  $\text{Cl}^-/\text{OH}^-$  to increase within the crevice.

## ***1.2 Objectives and scope***

The main objective of this thesis is to investigate numerically the chemistry of the concrete pore solution in the mill scale crevices of carbon steel rebar in order to test the hypothesis that the pore solution chemistry in these crevices may be different from that of

the bulk pore solution, and this difference may create the necessary conditions for the breakdown of the passive film on the steel surface when chlorides are present. These necessary conditions are generally defined in terms of chloride thresholds (*i.e.*,  $Cl^-/OH^-$ ). However, it was observed in many studies that rebars with modified (e.g. polished, sandblasted and/or or pickled) surfaces (with no mill scale) may depassivate at larger chloride thresholds than as-received rebars. As it will be further discussed in Chapter 2, in some cases rebars do not depassivate even after large  $Cl^-/OH^-$  values (e.g. larger than 3) are reached in the concrete pore solution. For these cases, it is possible that thermodynamic conditions that are necessary for active corrosion are not satisfied. These thermodynamic conditions are generally defined using Pourbaix diagrams, which are simply overlays of the redox and acid-base chemistry of elements, alloys and oxides onto the water stability diagram, establishing the potential-pH relationship of the system in equilibrium (Revie 2000). A typical Pourbaix diagram of iron in water is illustrated in Figure 1.2. In this diagram it can be observed that the high alkalinity of concrete pore solution (*i.e.*, pH ranging approximately from 12.5 to 13.5) positions rebar in the passivity region where it is protected by a stable passive oxide film. If the system were to be within the immunity region, corrosion would not occur as it said to be cathodically protected. For this oxide film to become thermodynamically unstable, the potential and pH of the system must be in one of the corrosion regions (Revie 2000).

For a freely corroding rebar (*i.e.*, no external potential is applied on the system), when the pH of the pore solution drops below 10 (see Figure 1.2), the oxide film on the steel rebar surface is no longer thermodynamically stable. Therefore, in this study, in addition to  $Cl^-$

$/\text{OH}^-$ , the pH of the pore solution within the mill scale cracks and crevices will also be monitored to determine if depassivation is thermodynamically possible. It was assumed in this study that when the pH of the pore solution within mill scale cracks and crevices drops below 10, rebar is depassivated regardless of the value of  $\text{Cl}^-/\text{OH}^-$ .

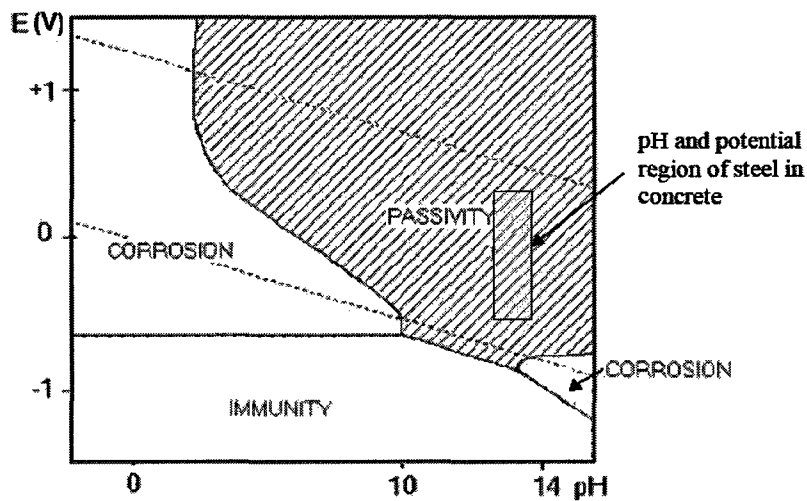


**Figure 1.2.** Pourbaix diagram for iron-water system at 25°C (reproduced from Esmaeilpoursaee 2007)

The numerical investigation focuses on the solution of coupled extended Nernst-Planck and Poisson's equations under constraints imposed by the chemical reactions and equilibrium requirements in domains that represent typical mill scale cracks and crevices. The parameters of the numerical investigation involve the geometry of the domain, pore solution chemistry, the passive current density of the steel and the transport properties of the modelled species. The pore solutions investigated in this study contain species that are present in typical concrete pore solutions; *i.e.*,  $\text{OH}^-$ ,  $\text{Fe}^{2+}$ ,  $\text{Ca}^{2+}$ ,  $\text{Cl}^-$ ,  $\text{Na}^+$ ,  $\text{K}^+$ , and  $\text{O}_{2(g)}$ . The simulations were carried out using a commercial software package called COMSOL Multiphysics™ under three scenarios: (1) simulations in chloride-free pore solutions; (2) simulations in pore solutions with chlorides when the passive current density is constant;

and (3) simulations in pore solutions with chlorides when the passive current density increases after an arbitrary chloride threshold is reached.

The numerical model developed in this thesis is based on the mechanism proposed by Ghods et al. (2009c). The following assumptions and simplifications have been made in this research:

- Focus is placed on the modelling of the transport of ionic, solid and gaseous species in the pore solution within mill scale cracks and crevices while all steel surfaces in the analysis domain are assumed to be passive and experiencing microcell corrosion with no macrocell anodes and cathodes. The modelling of the transport of ions in the pore solution after macrocell formation (e.g. after pitting) is not within the scope of this research.
- Since chloride-induced depassivation of rebar is the main interest of this research, other depassivation mechanisms (e.g. carbonation) are not considered.
- Only reactions in the pore solution involving  $\text{Ca(OH)}_{2(s)}$  and  $\text{Fe(OH)}_{2(s)}$  are considered in the current study. Many other reactions take place in typical concrete pore solutions (Ramachandran 1995, Glasser et al. 2008), mainly due to the presence of auxiliary ions (e.g.  $\text{SO}_4^{-2}$ ), but these are not considered in this study.
- Possible chloride binding by the concrete pore solution (Glass et al. 2000) is ignored.
- The pore solution is assumed to be stationary within mill scale cracks and crevices; therefore mass transport mechanisms due to advection (*i.e.*, mass

transport as a result of the movement of the pore solution) are not considered as part of the total flux of species during the modelling of transport phenomena.

### ***1.3 Organization of the thesis***

Chapter 1 of this thesis introduces the concept of mill scale crevices on rebar surfaces and their influence on the local depassivation mechanism of reinforcement in concrete pore solutions. Chapter 2 provides a literature review of other numerical models simulating localized corrosion, and presents a review of certain parameters that are used in the simulations (e.g. the passive current density and chloride thresholds). Chapter 3 provides the modelling theory and its implementation for the solution of the boundary value problem describing the pore solution chemistry within mill scale cracks and crevices. Chapter 4 provides the results and discussions of the numerical simulations. Chapter 5 lists the conclusions of the study and recommendations for future work.

The thesis also contains three appendices. In Appendix A, a detailed explanation of the solution process taken by COMSOL Multiphysics™ in solving the boundary value problem is presented. In Appendix B, the steps taken to implement a typical boundary value problem in COMSOL Multiphysics™ are presented. In Appendix C, the procedure taken to determine the finite element mesh that was used in the simulations carried out in this thesis is presented.

## **2) Literature Review**

This chapter presents a review of the literature that is relevant to the present work. The review starts with a general background on chloride thresholds to provide an understanding of the variability and uncertainty associated with the prediction of the onset of steel corrosion in concrete. Then, the existing experimental work on passive current density of carbon steel, which is one of the key parameters used in the simulations that are carried out in this study, is presented. Finally, prominent numerical models that simulate the localized corrosion of metals are examined to provide an understanding of the general application of the boundary-value problems describing the transport and interaction of species in a crevice or a pit.

### ***2.1 Chloride threshold of carbon steel rebar***

This section provides a review of literature to provide an understanding of the variability and uncertainty associated with the prediction of the onset of corrosion of carbon steel rebar in concrete. The chloride thresholds of other types of steel reinforcement (e.g. stainless and micro-composites steels) are not presented here. In this thesis,  $Cl^-/OH^-$  is used to identify the chloride threshold of carbon steel rebar in concrete; therefore, in this review, which is mainly based on a recent and comprehensive survey carried out by Angst et al. (2009), is presented using this representation of chloride threshold (as opposed to total chloride concentrations).

A large number of studies have reported chloride thresholds of rebar in concrete; Table 2.1 and Figure 2.1 (for abbreviations used in the table and the figure, see Table 2.2) show chloride thresholds in concrete are affected by a number of factors such as the exposure medium (*i.e.*, cement paste, mortar, concrete and synthetic pore solution), surface condition (e.g. as-received, sandblasted, polished, cleaned), corrosion detection method (e.g. half-cell potential, linear polarisation resistance, mass loss, potentiostatic control) and chloride source (*i.e.*, mixed-in with the concrete or introduced later via surface exposure). Other relevant parameters, which are not identified in Table 2.1 and Figure 2.1, but influence the chloride threshold include the binder type (Page et al. 1986, Reddy et al. 2002, Manera et al. 2008), moisture content of the concrete (Page 1975, Schiessl and Lay 2005), oxygen availability at the steel surface (Hausmann 1967, Isgor and Razaqpur 2006), electrical resistivity of the concrete (Morris et al. 2004, Ghods et al. 2009e), the degree of hydration of concrete (Hansson and Sørensen 1990, Poupard et al. 2004), temperature (Hussain et al. 1995, Pour-Ghaz et al. 2009), the type of cation accompanying chloride (Hansson et al. 1985, Andrade and Page 1986), and the presence of other species (e.g.  $\text{SO}_4$ ) in the concrete pore solution (Ramachandran 1995, Glasser et al. 2008). Discussions of these parameters are presented in detail by Angst et al. (2009).

Table 2.1 and Figure 2.1 demonstrate that there is no general agreement on the chloride threshold of carbon steel rebar in concrete. In fact, the reported threshold  $\text{Cl}^-/\text{OH}^-$  values are scattered in a wide range from 0.01 to 45. A widely accepted observation among these studies is that the chloride threshold is highly correlated with the alkalinity of the pore solution: the higher the alkalinity (*i.e.*, pH), the higher the chloride threshold, as can

be seen in Table 2.1. The variability in the experimental results is quite large, and can be attributed to, in part, the use of different experimental procedures and the number of parameters that influence chloride-induced corrosion of rebar. To eliminate the differences originating from the measurement techniques, Angst et al. (2009) expressed the strong need for a practical test method that uses standardized experimental parameters. Nevertheless, even when similar testing procedures are used, the chloride thresholds in carbon steel rebar still show variability; Ghods et al. (2009d) proposed that this variability might be partially due to the surface condition of rebar, in particular, the presence of mill scale on the steel surface.

Electrochemical measurements carried out by Ghods et al. (2009d) showed that modifying the rebar surface, by turning on a lathe and polishing rebar specimens to eliminate mill scale and deformities, leads to less variable and higher chloride thresholds than those measured for as-received rebars. For example, Ghods et al. (2009d) reported chloride thresholds for turned-and-polished rebar specimens in the range between 0.45 M to 1.25 M in simulated pore solutions with pH of 13.3. It was shown that, in a solution with identical properties, as-received rebar specimens had chloride thresholds that ranged from 0.05 M to 0.15 M. Ghods et al. (2009d) suggested how the local differences in the chemical composition of the pore solution in the vicinity of mill scale, as compared with the composition of the bulk pore solution, could explain why there could be such a large variability in the chloride thresholds for as-received rebar. In fact, an SEM study conducted by Ghods et al. (2009c) shows that mill scales on carbon steel rebar have variable characteristics: they form non-uniformly on the rebar surface during the

manufacturing process, and they contain transverse cracks, some of which are linked to crevices between the mill scale and rebar surface and provide pathways for concrete pore solution to penetrate into the crevices. Ghods et al. (2009c) suggested that the local chemistry of the pore solution within these crevices may vary from that of the bulk solution, making these crevices highly susceptible to pit initiation. The current investigation investigates these local changes using a numerical approach.

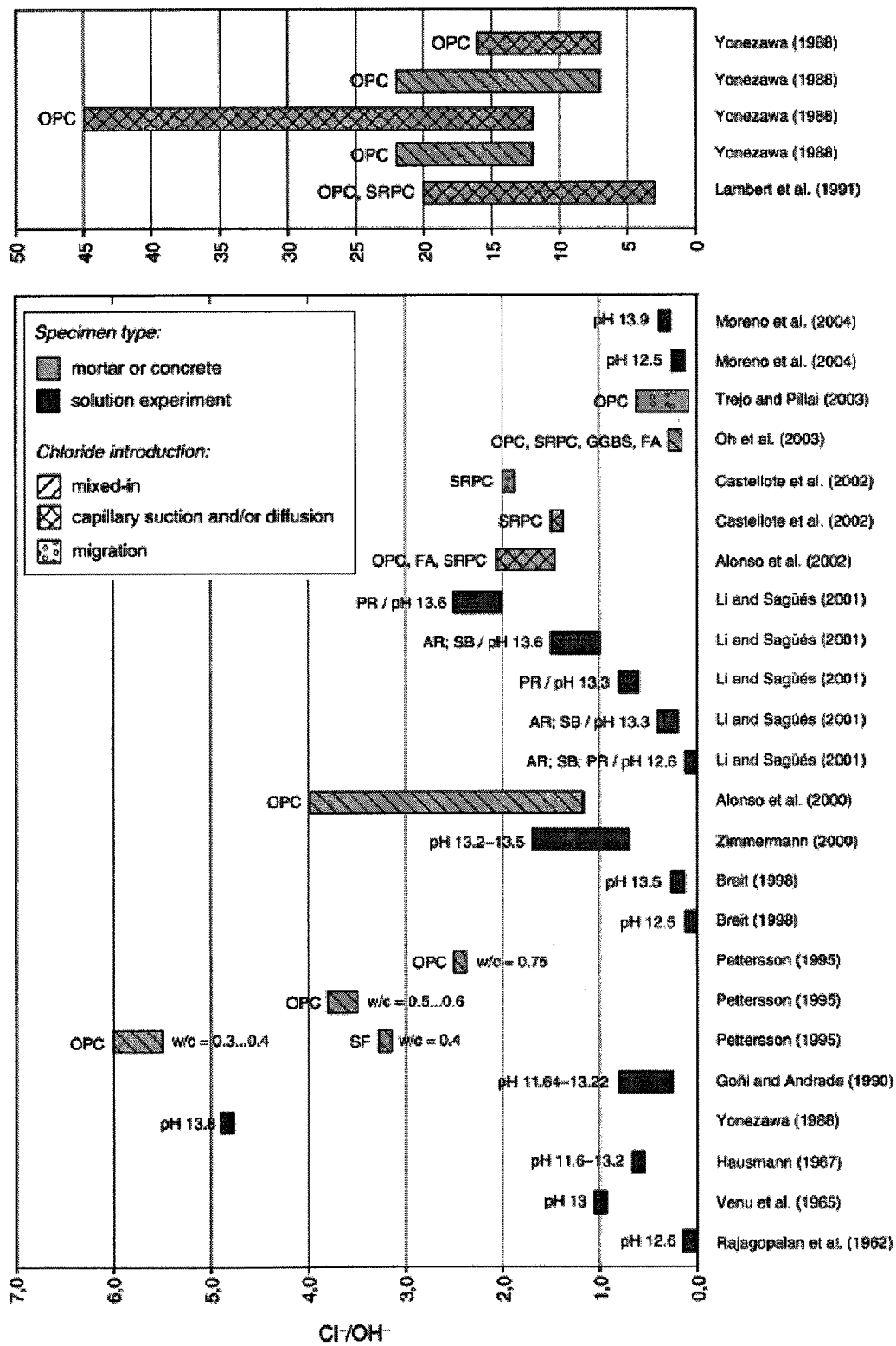


Figure 2.1. Summary of reported chloride threshold values (taken from Angst et al. 2009). Abbreviations are given in Table 2.2.

**Table 2.1:** Summary of reported chloride threshold values (taken from Angst et al. 2009).

Abbreviations are given in Table 2.2.

Reference	Steel condition	Corrosion detection	Exposure medium	Cl <sup>-</sup> /OH <sup>-</sup>
Rajagopalan et al. (1962)	ABR, CL	GP	pH 12.6	0.02–0.13
Venu et al. (1965)	ABR, CL	GP	pH 13	1.0
Hausmann (1967)	SM, P, CL	E, VI	pH 11.6–13.2	0.6
Yonezawa et al. (1988)	P	LPR, E	pH 13.8	4.9
			OPC	7–45
Goñi and Andrade (1990)	P, CL	LPR, E	pH 11.64–13.22	0.25–0.8
Lambert et al. (1991)	SM, SB, CL	LPR, E, WL	OPC, SRPC	3–20
Pettersson (1995)	RIB	LPR	OPC, SF	2.5–6
Breit (1998)	CL	PC	pH 13.5	0.26
Alonso et al. (2000)	RIB, SM	LPR, E	OPC	1.17–3.98
Zimmermann et al. (2000)	SB; CL	E, MC	pH 13.2–13.5	0.7–1.7
Li and Sagüés (2001)	AR, SB, PR	E, EIS	pH 12.6	0.01–0.04
			pH 13.3	0.2–0.8
			pH 13.6	1.0–2.5
Alonso et al. (2002)	RIB, MIL	PC	OPC, SRPC, FA	1.67±0.3
Castellote et al. (2002)	RIB	LPR, E	SRPC	1.5–2.0
Oh et al. (2003)	SM	E, VI	OPC, SRPC, GGBS, FA	0.16–0.27
Trejo and Pillai (2003)	CL	LPR	OPC	0.09–0.62
Moreno et al. (2004)	CL	PDP	pH 12.5	0.178
			pH 13.9	0.313

**Table 2.2:** Abbreviations in Table 2.1 and Figure 2.1 (taken from Angst et al. 2009).

Exposure medium	Steel condition	Corrosion detection
<i>FA</i> - Fly ash.	<i>ABR</i> – Abraded.	<i>E</i> – Potential.
<i>GGBS</i> - Ground granulated blast furnace slag.	<i>AR</i> - As-received.	<i>EIS</i> - Electrochemical impedance spectroscopy.
<i>OPC</i> - Ordinary Portland cement.	<i>CL</i> – Cleaned or degreased.	<i>GP</i> - Galvanostatic polarisation.
<i>SF</i> - Silica fume.	<i>MIL</i> - Mill-scaled.	<i>LRP</i> - Linear polarisation resistance.
<i>SRPC</i> - Sulphate resistant Portland cement.	<i>P</i> – Polished.	<i>MC</i> - Macro-cell current.
	<i>PR</i> - Pre-rusted.	<i>PC</i> - Potentiostatic control.
	<i>RIB</i> - Ribbed steel bars.	<i>PDP</i> - Potentiodynamic polarisation.
	<i>SB</i> – Sandblasted.	<i>VI</i> - Visual inspection.
	<i>SM</i> - Smooth steel bars.	<i>WL</i> - Weight loss.

## **2.2 Passive current density of carbon steel rebar**

The passive current density,  $i_p$ , of carbon steel is one of the parameters used in the simulations that are carried out in this study; This section presents a review of the existing experimental work on passive current density. Since this study is focused on the investigation of the pore solution chemistry in the mill scale crevices of carbon steel rebar, the literature pertaining to other types of steel is not presented. Furthermore, this literature review is limited to the passive current density measurements that were carried out in highly alkaline environments that are representative of concrete pore solution; therefore, studies are only reported in simulated pore solutions, mortar or concrete. Since, two concrete pore solutions (*i.e.*, one with pH ~12.5 and another with ~13.5) are modelled in this thesis, the review is mostly focused on studies that cover studies in solutions with pH ranging from 12 to 13.5.

As reported by Alonso et al. (2000), González et al. (2005), Poursaee and Hansson (2007), and Ghods et al. (2007, 2008a, 2009e) the measurements of passive current density of rebar are quite sensitive to the testing conditions and are affected by the test medium (*i.e.*, whether the measurement is carried in simulated pore solution, mortar or concrete), test setup (*i.e.*, the corrosion cell used to carry out the measurements), specimen type and size (*i.e.*, whether actual rebar or prepared specimens are used), and the surface conditions of the specimen (*i.e.*, whether the measurements are made on as-received or prepared steel surfaces). Ideally, the values of passive current density that are used in the simulations of this study would be representative of passive carbon steel with pristine (with no mill scale or deformities) surface conditions and are not affected by the

complications originating from testing conditions. Unfortunately, the number of studies that investigated the passive properties of carbon steel with pristine surface conditions is quite limited; therefore the review presented here is intended to provide a range from which realistic values of passive current density can be selected for modelling purposes.

When rebar is placed in a highly alkaline environment (e.g. simulated concrete pore solution, mortar, or concrete), a passive oxide film grows on the steel surface until a stable film is reached. If the current density on the steel surface is monitored during the film growth, it can be observed that it decreases as the thickness of the film increases, reaching a relatively constant value (*i.e.*, passive current density,  $i_p$ ) after the development of a stable passive film. Ghods et al. (2009e) carried out anodic polarization experiments on carbon steel rebar specimens in simulated pore solutions (with pH 12.5 and 13.5) and concluded that a minimum of 8 days were required for a stable passive film to form on the steel surface. A similar observation was also made by Poursaeed and Hansson (2007), who carried out potentiostatic linear polarization resistance (LPR) tests on (as-received and sand-blasted) carbon steel specimens and discovered that, for a stable passive film to form, approximately 7 days were required in mortar and approximately 3 days were required in synthetic pore solutions with a pH greater than 13. Moreno et al. (2004) also conducted LPR tests on as-received carbon steel samples in simulated pore solutions (pH = 12.5) and found that the passive film stabilized approximately after 4 days.

These three studies suggest that measurements that are made before stable passive film formation will yield higher passive current densities than those that would be observed after the stable passive film is formed. In fact, a number of anodic polarization studies on carbon steel rebar specimens shortly after exposure to the pore solution (Hurley and Scully 2006, Moreno et al. 2004, Li and Sagüés 2002) reported current densities around  $10^{-2}$  A/m<sup>2</sup>. For example, Hurley and Scully (2006) found a passive current density of 0.01 A/m<sup>2</sup> when potentiodynamic scans were carried out on polished carbon steel rebar in solutions consisting of saturated Ca(OH)<sub>2</sub> with various amounts of NaCl present, but the steel was exposed to a passivating solution for only 1 hour prior to polarization; thus, there was likely not enough time for a stable passive film growth. Moreno et al. (2004) also carried out potentiodynamic anodic polarization measurements on rebar samples in saturated Ca(OH)<sub>2</sub> solutions after only 1 hour exposure to the solution at an open circuit potential, and a passive current density of 0.007 A/m<sup>2</sup> was measured. Similarly, Li and Sagüés (2002) carried out cyclic polarization experiments on sandblasted rebar specimens in alkaline solutions (pH 11.6 - 13.6) containing chlorides shortly after the exposure of the specimens to the solution, and obtained a passive current density of 0.04 A/m<sup>2</sup>. These experiments yielded relatively large passive current densities. The studies that were carried out after the formation of stable passive films, on the other hand, report current densities in the order of  $10^{-3}$  A/m<sup>2</sup> (0.1  $\mu$ A/cm<sup>2</sup>) or less (Lambert et al. 1991, Moreno et al. 2004, Poursaee and Hansson 2007, Ghods et al. 2008a, 2009e), as presented later in this section.

Lambert et al. (1991) studied the relationship between the current density on rebar and  $\text{Cl}^-/\text{OH}^-$  in the pore solution and concluded that a  $\text{Cl}^-/\text{OH}^-$  in excess of 3 causes the current density to gradually increase from its passive state during which passive current density was approximately equal to  $1.5 \times 10^{-4} \text{ A/m}^2$ , as shown in Figure 2.2. This experimental study was conducted using linear polarization techniques on grit-blasted carbon steel rods that were embedded in Ordinary Portland Cement (OPC) and sulphate resistant Portland cement mortars (SRPC). Four steel rods were tested in each cement paste at various cover depths (10, 20, 30 and 40 mm) and exposure conditions (constantly maintained solution, weekly wet/dry cycle, or monthly wet/dry cycle); however, Lambert et al. (1991) observed no significant difference between the different cement types, cover depths, and exposure conditions when relating the corrosion rate to  $\text{Cl}^-/\text{OH}^-$ .

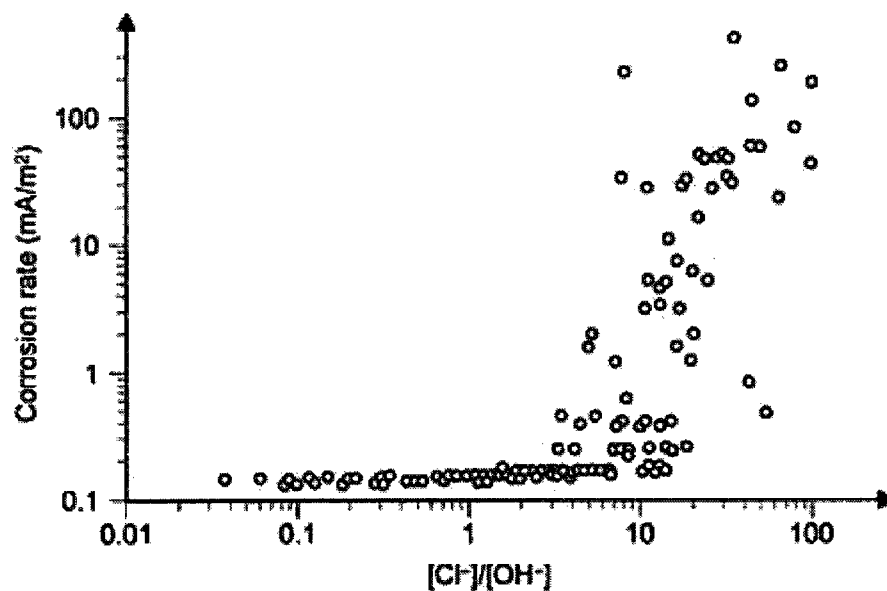


**Figure 2.2.** Variation of the current density of grit blasted steel rods at different  $\text{Cl}^-/\text{OH}^-$  in cement paste (taken from Lambert et al. 1991).

Moreno et al. (2004) measured the corrosion current density on as-received reinforcing steel bars immersed in simulated pore solutions, saturated with  $\text{Ca}(\text{OH})_2$  and varying

chloride concentrations, for 160 hours using the LPR technique to determine the time required for rebar to be passivated. The tested carbon steel specimens were 3.5 cm in length and 4.5 mm in diameter; all measurements were performed at room temperature. The results of these experiments, which are presented in Figure 2.3, indicate that a passive current density of slightly less than  $10^{-3} \text{ A/m}^2$  (corresponding to  $10^{-7} \text{ A/cm}^2$  in the figure) was measured when no chloride was present. In the simulated pore solutions that contained chlorides, a breakdown of the passive film was observed, and the current densities increased by one order of magnitude compared to those measured in the passive state.

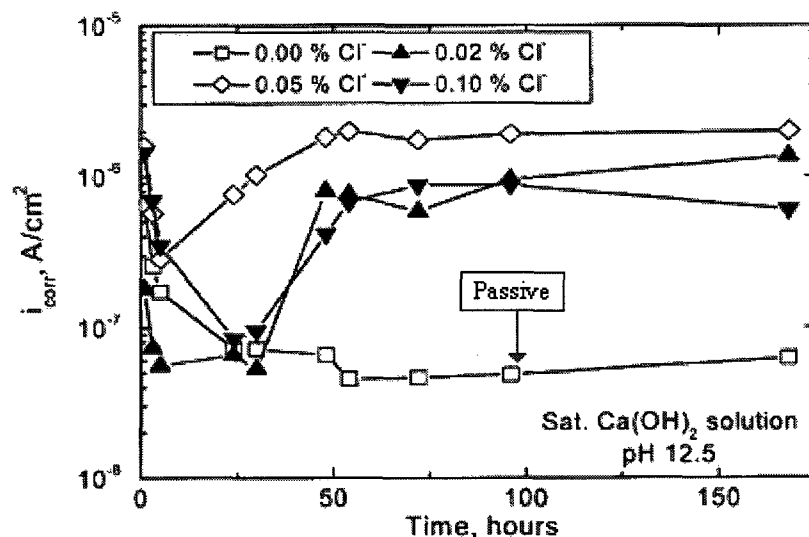


**Figure 2.3.** Corrosion current density of as-received carbon steel rods in saturated  $\text{Ca}(\text{OH})_2$  solutions with different concentrations of chloride ion (taken from Moreno et al. 2004).

In general, the passive current density of rebar is affected by a number of factors that include the composition of the steel (Hurley and Scully 2006), the surface conditions of the rebar (Poursae and Hansson 2007, Alonso et al. 2000, Ghods et al. 2008a) and the properties of the pore solution (Poursae and Hansson 2007, Ghods et al. 2009e).

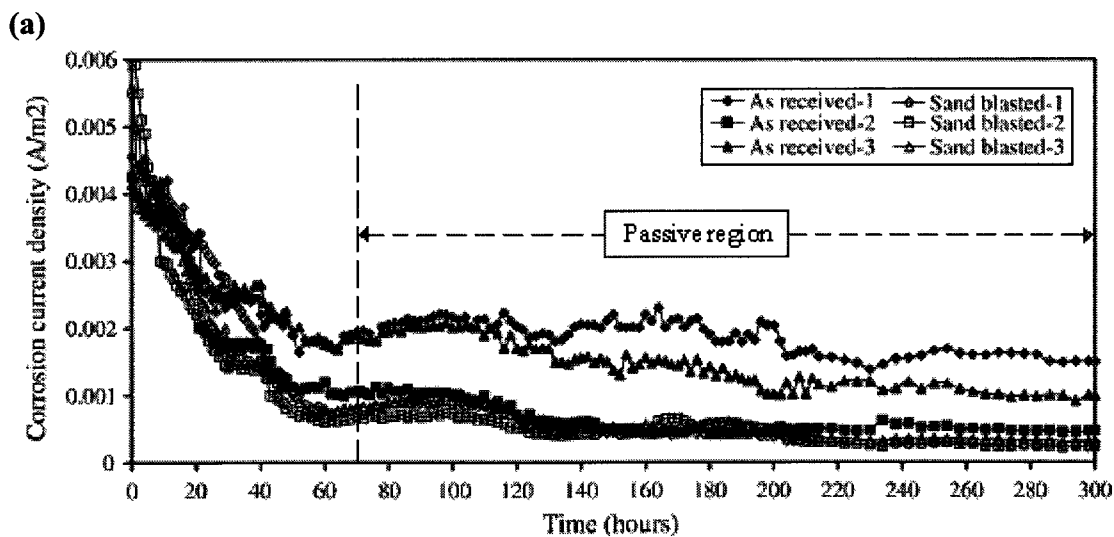
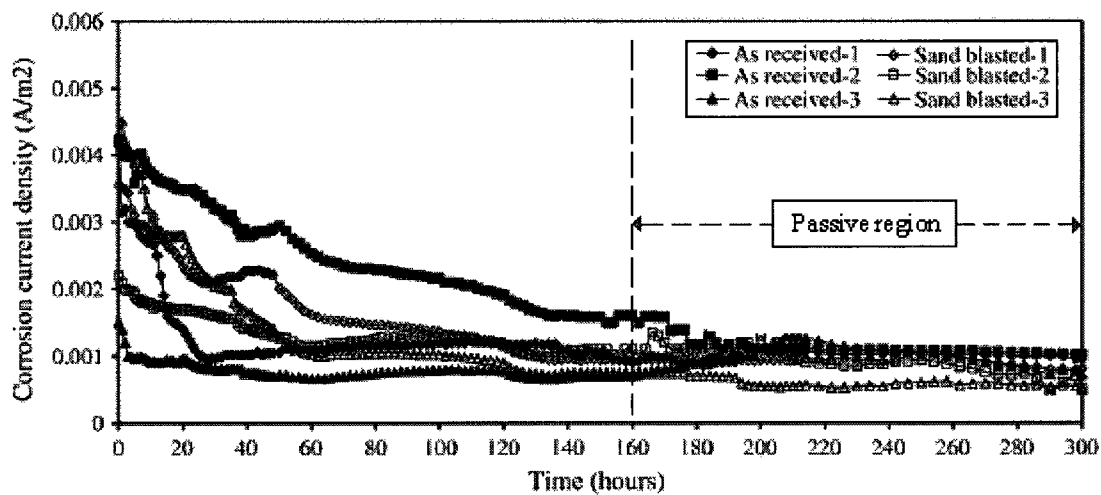
Poursaeed and Hansson (2007) conducted experiments on as-received and sand-blasted carbon steel rebar in mortar (type 10 Portland mortar, w/c ratio = 0.45) and synthetic pore solution with pH > 13 (composition: 2.4 g/l Ca(OH)<sub>2</sub> + 5.24 g/l NaOH + 17.94 g/l KOH + 0.55 g/l CaSO<sub>4</sub>·2H<sub>2</sub>O) to determine the time required for rebar to be passivated. Three as-received and three sand-blasted specimens, that were approximately 9 cm in length and 10 mm in diameter, were embedded in each exposure medium and were monitored using the potentiostatic LPR technique for 300 hours. In Figure 2.4a, a passive current density of 10<sup>-3</sup> A/m<sup>2</sup> is shown for as-received samples in mortar, which is slightly higher than the samples with sand-blasted surfaces for which the passive current density ranged from 5x10<sup>-4</sup> to 10<sup>-3</sup> A/m<sup>2</sup>. This variation between as-received and sand-blasted samples was more evident when measuring samples in synthetic pore solutions; Figure 2.4b shows that the passive current density for the as-received samples that ranged from 5x10<sup>-4</sup> to 2x10<sup>-3</sup> A/m<sup>2</sup> are greater than that of the sand-blasted samples (10<sup>-4</sup> A/m<sup>2</sup>). For a given steel composition with pristine surface finish, Poursaeed and Hansson (2007) showed that passive current density increases with increasing alkalinity and with reducing resistivity of the pore solution; however since the increasing alkalinity is typically associated with the reduced resistivity of the pore solution, they commented that these two parameters are not independent.

Ghods et al. (2009e) also concluded that the quality of the passive film is influenced by the composition of the pore solution in which it was grown: higher quality is characterized by lower passive current density, and vice versa. They also reported that an increase of pH from 12.5 to 13.5 causes the passive current density to increase up to one

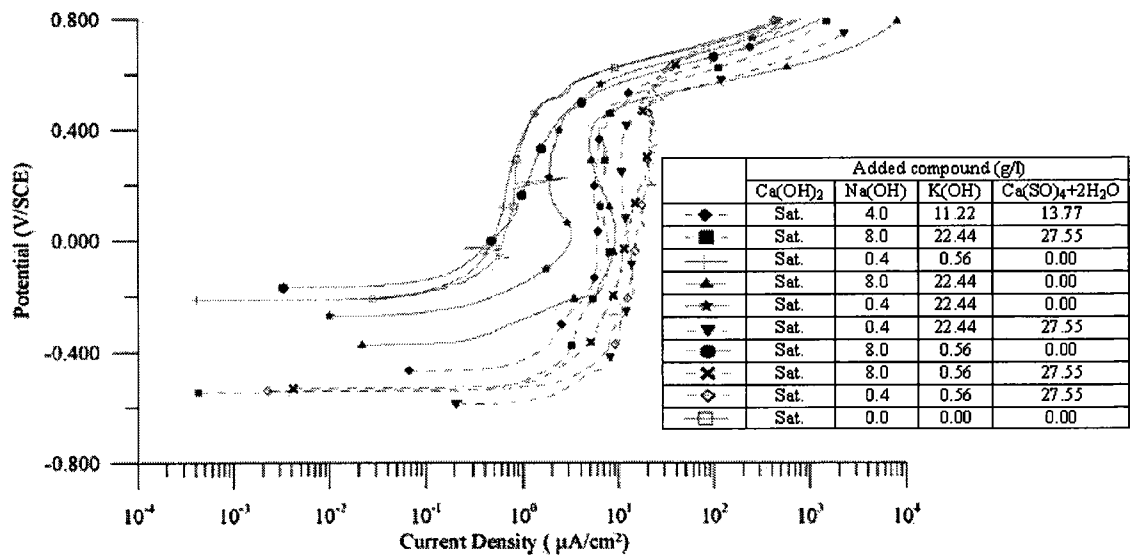
order of magnitude, as is shown in Figure 2.5a; however, they concluded that the passive current densities were not significantly correlated with pH or conductivity of the pore solutions; they suggested the existence of more complicated functional dependencies. Ghods et al. (2009e) also stated the importance of surface conditions on passive current density. Anodic polarization experiments on as-received (with mill scale and deformity ribbing) and turned-and-polished (mill scale and deformity ribbing removed) rebar specimens in a simulated concrete pore solution (composition provided in Figure 2.5a) showed that passive current density of the turned-and-polished specimens with pristine steel surface is one order of magnitude smaller than that of the as-received specimens. The effect of surface conditions on the passive current density of carbon steel rebar in simulated concrete pore solution (composition: 0.1 M  $\text{Ca}(\text{OH})_2$  + 0.1 M  $\text{Na}(\text{OH})$  + 0.2 M  $\text{K}(\text{OH})$  + 0.003 M  $\text{Ca}(\text{SO})_4 \cdot 2\text{H}_2\text{O}$ ) was also considered by Ghods et al. (2008a), and as was the case for the previous study, the as-received specimens had lower current densities than the specimens with polished surfaces, as illustrated in Figure 2.5b.

Through anodic polarization measurements on steel in saturated  $\text{Ca}(\text{OH})_2$  solutions at various chloride concentrations, Saremi and Mahallati (2002), Moreno et al. (2004), Hurley and Scully (2006) and Ghods et al. (2008a) showed that the addition of small concentrations of chloride (smaller than threshold concentrations) had no effect on the passive current density. This can be seen in Figure 2.5b, which shows similar anodic polarization curves and passive current densities for polished carbon steel rebar specimens in a simulated pore solution with  $\text{pH} = 13.3$ . Alonso et al. (2000), González et al. (2005) and Abd El Aal et al. (2009) reported that when the chloride concentration

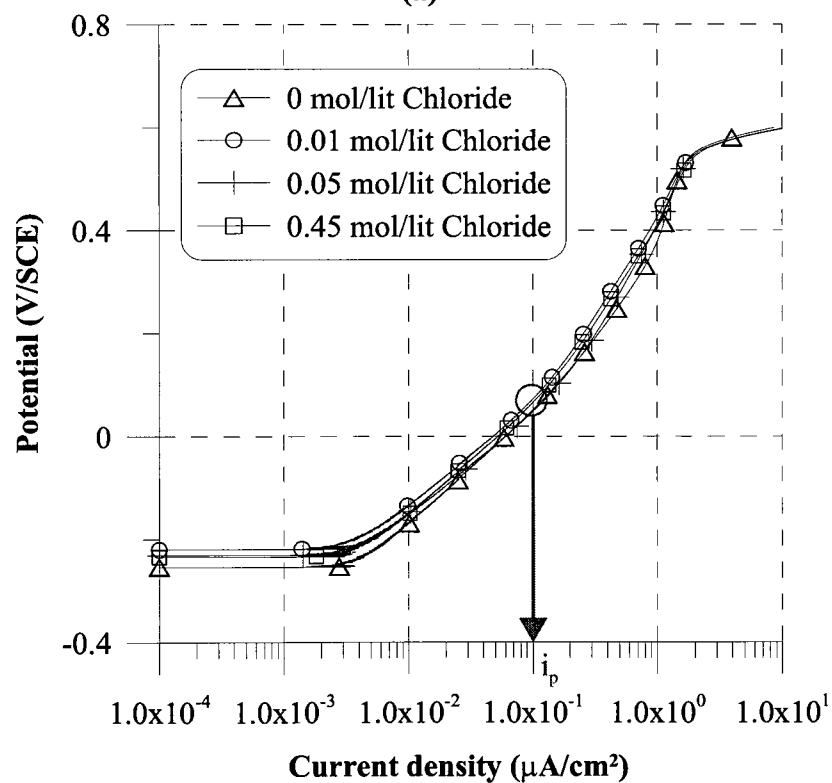
reaches a threshold, the passive current density increases; and further increase of the chloride concentration in the pore solution may lead to the breakdown of passive film and pitting. The literature on the pattern of increase in the passive current density beyond the threshold (*i.e.*, whether it is sudden or gradual) is not conclusive.



(b)  
**Figure 2.4.** Corrosion current density of carbon steel in (a) mortar (b) synthetic pore solution with a pH > 13 (taken from Poursaee and Hansson 2007).



(a)



(b)

**Figure 2.5.** Anodic polarization curve of (a) as-received carbon steel in different synthetic pore solutions (taken from Ghods et al. 2009e) (b) polished carbon steel in simulated pore solution with pH = 13.3 (reproduced from Ghods et al. 2008a).

A summary of experimental studies on the passive current density (in the absence of chlorides) is presented in Table 2.3. In general, as-received (with mill scale and deformity ribbing) rebar specimens tend to have larger passive current densities than specimens with mill scale removed (*i.e.*, turned-and-polished, sand-blasted or grit-blasted). Furthermore, passive current densities were found to increase with increasing alkalinity, but this increase in passive current density can also be attributed to other functional dependencies (Poursaee and Hansson 2007, Ghods et al. 2009e).

**Table 2.3:** Summary of experimental studies on the passive current density <sup>(1)</sup>.

Reference	Specimen type and size	Electrochemical technique	Exposure medium	Surface condition <sup>(2)</sup>	Passive current density (A/m <sup>2</sup> )
Lambert et al. (1991)	Steel rods: 3 mm diameter	Potentiodynamic polarization resistance	OPC & SRPC	Grit-blasted	$1.5 \times 10^{-4}$
Moreno et al. (2004)	Reinforcing steel bars: 3.5 cm length & 4.5 mm diameter	Potentiodynamic polarization resistance	Simulated pore solution: Ca(OH) <sub>2</sub>	As-received	$10^{-3}$
Poursae and Hansson (2007)	Carbon steel bars: ~ 9 cm length & 10 mm diameter	Potentiostatic polarization resistance	Type 10 Portland mortar (w/c=0.45)	As-received	$10^{-3}$
				Sand-blasted	$10^{-3}$ to $5 \times 10^{-4}$
			Synthetic pore solution: Ca(OH) <sub>2</sub> + NaOH + KOH + CaSO <sub>4</sub> ·2H <sub>2</sub> O	As-received	$2 \times 10^{-3}$ to $5 \times 10^{-4}$
				Sand-blasted	$10^{-4}$
Ghods et al. (2008a)	Carbon steel rebar: 3 cm length & 10 mm diameter	Potentiodynamic polarization	Synthetic pore solution: Ca(OH) <sub>2</sub> + NaOH + KOH + CaSO <sub>4</sub> ·2H <sub>2</sub> O	Polished	$10^{-3}$
Ghods et al. (2009e)	Carbon steel rebar: 3 cm length & 10 mm diameter	Potentiodynamic polarization	Synthetic pore solution: Ca(OH) <sub>2</sub> + NaOH + KOH + CaSO <sub>4</sub> ·2H <sub>2</sub> O	As-received	$7 \times 10^{-3}$ to $5 \times 10^{-2}$

<sup>(1)</sup> These passive current densities were measured in the absence of chlorides.

<sup>(2)</sup> Sand-blasted and grit-blasted samples remove mill scale from rebar surface, while polished samples remove mill scale and deformity ribbing.

### **2.3. Numerical models of localized corrosion**

Many numerical models that simulate chemistry of the electrolytes within localized zones of metals and alloys exist in the literature; however, the effect of mill scale crevices (that exist on rebar surfaces) on the breakdown of passive films has not been modelled previously. The model developed in this thesis use many of the attributes developed for previous models; therefore, a review of the existing models that simulate localized corrosion of metals and alloys is presented here.

#### **2.3.1 Sharland et al. (1989)**

Sharland et al. (1989) modelled corrosion in a crevice on carbon steel that was filled with a dilute solution of NaCl. The mechanisms controlling the movement of the species within the crevice over time were governed by mass-balance equations describing diffusion under concentration gradients, electrical migration under potential gradients and a chemical reaction term. A separate electro-neutrality equation was also added to eliminate any charge gradients in the system. Six species (*i.e.*,  $\text{Fe}^{2+}$ ,  $\text{FeOH}^+$ ,  $\text{Na}^+$ ,  $\text{Cl}^-$ ,  $\text{H}^+$  and  $\text{OH}^-$ ) were used in this model. These species were included to simulate the dissolution of a metal ( $\text{Fe}^{2+}$ ), the separation of water molecules ( $\text{H}^+$  and  $\text{OH}^-$ ), hydrolysis of a metal oxide ( $\text{FeOH}^+$ ) and the presence of a chloride bearing salt ( $\text{Na}^+$  and  $\text{Cl}^-$ ). The chemical reactions in the solution (*i.e.*, reactions involving the products  $\text{FeOH}^+$ ,  $\text{Fe}(\text{OH})_2$  and  $\text{H}_2\text{O}$ ) were assumed to be at equilibrium at all times and were represented by the chemical reaction term in the mass-balance equation. Two domains were investigated by Sharland et al. (1989): Figure 2.6 represents the two-dimensional domain which contained an active tip and crevice surfaces and was discretized using rectangular

elements. A one-dimensional case which contained passive walls with an active tip was also considered. Both models had fixed concentrations for all species at the crevice mouth to represent the bulk solution outside the crevice. The active surfaces for both models included only the metal dissolution reaction; thus, iron dissolution was represented by a flux term that corresponded to the current density at the active surfaces, while all other species had a flux of zero. The model produced by Sharland et al. (1989) gave reasonable qualitative and quantitative agreements with the experimental data of Alavi and Cottis (1983), in which measurements of pH and potential were carried out in a simulated crevice on carbon steel.

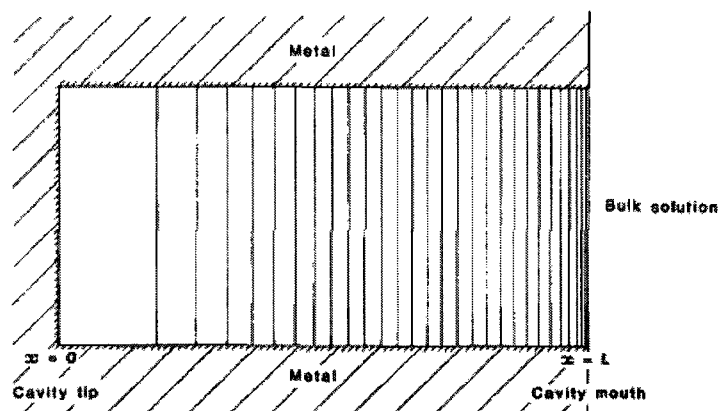


**Figure 2.6.** Finite element domain used to simulate crevice corrosion (taken from Sharland et al.1989).

### 2.3.2 Harb and Alkire (1991)

The numerical model produced by Harb and Alkire (1991) was used to simulate an active corrosion pit with passive walls on a nickel surface, which was exposed to a 0.5 M NaCl solution. Figure 2.7 shows the two-dimensional axi-symmetric domain used for the simulations. Within this domain, the modelled species (*i.e.*,  $\text{NiCl}^+$ ,  $\text{NiCl}_2$ ,  $\text{Ni}^{2+}$ ,  $\text{Cl}^-$  and  $\text{Na}^+$ ) were subjected to diffusion and electrical migration through concentration and

electric potential gradients, respectively. The concentration of the species was constrained by two equilibrium relations that were based on the chemical reactions involving aqueous species  $\text{NaCl}^+$  and  $\text{NaCl}_2$ . The reactions involving hydrolysis products were excluded from the model because it was numerically found not to affect significantly the concentration of species in the solution or the potential field. To couple the concentration and potential fields in the domain, an electro-neutrality equation was also added. The surface kinetics of this model were defined based on the boundaries represented in Figure 2.7. On the active surface (*i.e.*, pit surface), the dissolution of nickel was represented by a flux term that was related to the current density on the nickel surface. All other species had a flux of zero on this surface. On the inert surface (*i.e.*, cathodic area around the pit), no surface reactions were defined because of its passive state. The boundary conditions at the bulk solution position had fixed concentrations and fixed electric potential. This boundary was placed at a sufficient distance away from the pit so that the concentration profiles in the pit region were not disturbed.

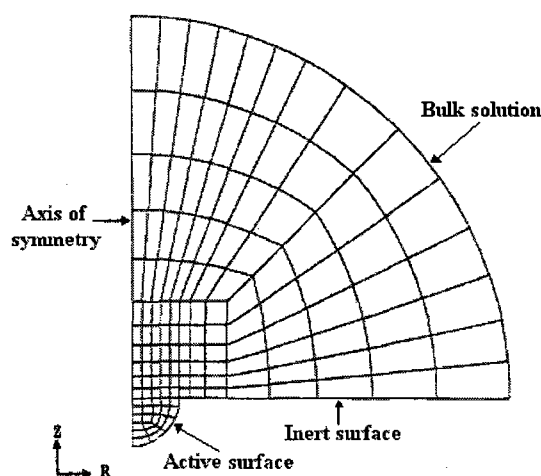


**Figure 2.7.** Finite element domain used to simulate the dissolution of a hemispherical corrosion pit (taken from Harb and Alkire 1991).

In this numerical model, physical parameters (*i.e.*, diffusion coefficient, solubility product constants and the pit radius) were assumed to be constant. This assumption might not be accurate as these parameters may change due to the change in chemistry within the solution (Harb and Alkire 1991); however, it was mentioned that no physical data were available for these types of systems and that this assumption needed to be made. It was also assumed in this model that the surface around the anodic pit was inert. According to Sikora and Macdonald (2002), a passive current density is present on the passive surfaces of nickel; hence, this omission could explain why the chemical reactions involving hydrolysis products were considered insignificant in this model. The concentration profiles produced by the numerical model showed an enrichment of ions inside the pit to a level with a high ionic strength of approximately  $4500 \text{ mol/m}^3$ . Around these ionic strengths, the ionic species within the solution would experience an increased amount of interactions causing considerable changes to the concentration of each species in the solution (Samson et al. 1999b). Considering these interactions in the simulations, by means of adding a chemical activity term in the governing differential equation, could have improved the realistic nature of the numerical model.

### **2.3.3 Chang et al. (2000)**

Chang et al. (2000) developed a numerical model to study the initiation stage of crevice corrosion in NaCl solution where the metal surface inside the modelled crevice, which is illustrated in Figure 2.8, was assumed to be covered with a passive film that protected the metal until pH dropped below 1.7 and crevice corrosion initiated. The model considered a complex solution chemistry consisting of sixteen chemical reactions. Accordingly, a large

number of species (*i.e.*,  $H^+$ ,  $OH^-$ ,  $Na^+$ ,  $Cl^-$ ,  $Fe^{2+}$ ,  $FeOH^+$ ,  $Fe(OH)_{2(aq)}$ ,  $Ni^+$ ,  $NiOH^+$ ,  $Ni(OH)_{2(aq)}$ ,  $Cr^+$ ,  $CrOH^{2+}$ ,  $Cr(OH)_2^+$ ,  $Cr(OH)_3(aq)$ ,  $Mo^{6+}$ ,  $MoO_4^{2-}$ ,  $HMoO_4^-$ ,  $H_2MoO_4$ ,  $O_2$ ) were included when evaluating the transport processes. The governing equations used in this model included terms to simulate diffusion, migration, metal ion dissolution from the crevice wall, chemical reactions, and electric potential in the solution. The diffusion term was described using concentration gradients; two migration terms were added to describe the current induced due to the potential gradient and the concentration; the dissolution of metal ions was described using a flux term in the governing equation that was based on the current at the metal-solution interface; and the electric potential in the solution was described using Poisson's equation. The boundary conditions for the governing equations consisted of a zero concentration flux along the crevice walls and a fixed concentration at the crevice mouth based on the bulk solution conditions. It should be noted that no potential terms were defined at the boundaries because the potential term in the governing equation was replaced by an electro-neutrality relation in order to decrease the computation time.

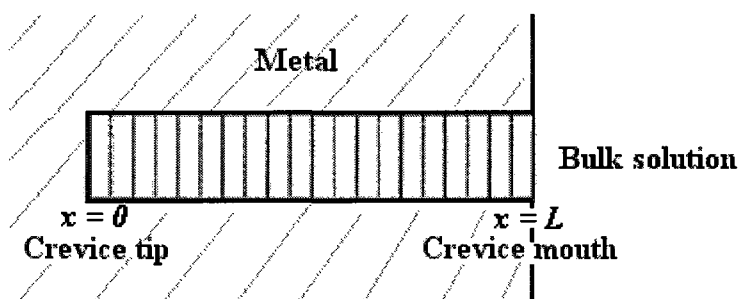


**Figure 2.8.** Finite element domain used to simulate the initiation stage of crevice corrosion (reproduced from Chang et al. 2000).

Similar to other models investigated in this section, the solution was assumed to be dilute; thus, ionic species were not presented in terms of activity in this model (Samson et al. 1999b).

The governing equations included in this model were essentially describing a one-dimensional system because only one layer of rectangular elements was used to discretize the domain. As a result, the transport in the transverse direction was ignored, causing the concentrations of the species to be uniform across the crevice thickness; it was assumed by the researchers that this simplification would result in negligible errors because the crevice width was rather small (Chang et al. 2000). The advection term (describing the movement of species with the fluid) was also ignored in this model because it was believed that this effect was not a significant factor within crevices with these small volumes (Chang et al. 2000).

#### **2.3.4 Chin and Sabde (2000)**

The crevice corrosion model developed by Chin and Sabde (2000) considered the crevice formed for a metal pipeline when coating disbands from the surface, as illustrated in Figure 2.9. The two-dimensional axi-symmetric model presented in this figure was assumed to be initially filled with a dilute NaCl solution containing  $\text{Na}^+$ ,  $\text{Cl}^-$ ,  $\text{OH}^-$ , and  $\text{O}_2$  species. The movement of these species was based on a steady-state transport equation that describes diffusion under concentration gradients and electrical migration under potential gradients. In addition, an electro-neutrality equation was added to maintain electrical balance in the solution. The boundary conditions for these equations were based



surface cathodic reactions would unlikely take place. Lastly, Chin and Sabde (2000) noted that larger ionic strengths caused larger margin of errors with experimental data. This can be explained by the fact that a dilute solution was assumed in the model; thus, numerical results were less accurate as the ionic strength increased because chemical activity effects were ignored (Samson et al. 1999b).

### **2.3.5 Vankeerberghen (2004)**

A numerical model that predicted the onset of crevice corrosion in a NaCl solution was investigated by Vankeerberghen (2004). A schematic representation of the modelled crevice is shown in Figure 2.10. The movement of the modelled species (*i.e.*,  $\text{Al}^{3+}$ ,  $\text{Al}(\text{OH})^{2+}$ ,  $\text{H}^+$ ,  $\text{OH}^-$ ,  $\text{Na}^+$ ,  $\text{Cl}^-$ ,  $\text{H}_2\text{O}$ ) within the crevice was represented by Nernst-Planck equations that included diffusion under concentration gradients, electrical migration under potential gradients, advection under fluid movement, and a chemical reaction term that described the homogeneous hydrolysis reaction involving  $\text{Al}(\text{OH})^{2+}$ . To take the electric potential gradients of the solution into account, Poisson's equation was also included in the model. Before solving these equations, the concentration and electric potential variables were defined on the boundaries. On the aluminium surface, the electrochemical reaction involving the production of  $\text{Al}^{3+}$  was considered by defining a concentration flux that was related to the current density on the aluminium surface through Faraday's law. All other species had a zero concentration flux and the electric potential had a zero potential gradient at this boundary. On the non-conductive insulator surface, all species had a zero concentration flux and the electric potential gradient was

also defined as zero. At the crevice mouth, the concentration of all species was fixed based on their bulk conditions and a zero electric potential was defined.

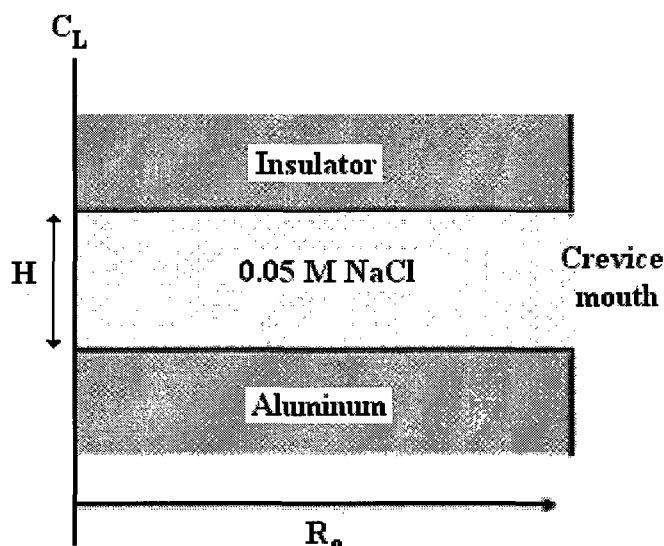


**Figure 2.10.** Schematic representation of the modelled crevice formed between a quartz disk at the top and an aluminium disk at the bottom.  $H$  is the height of the crevice,  $R_o$  is the radius and  $C_L$  is the centreline representing the axis of cylindrical symmetry (taken from Vankeerberghen 2004).

Unlike other numerical models investigated in this chapter, which assume a static (*i.e.*, immobile) electrolyte, the numerical model shown in this section introduces the advection term (*i.e.*, transport due to fluid movement) in the mass-transport equations; however, a chemical activity term was still not included. Having written this, neglecting this term was believed to be a reasonable assumption for this model because of the low ionic strength (*i.e.*,  $\sim 50 \text{ mol/m}^3$ ) of the studied solutions. It was also mentioned in this model that de-aeration occurred within the crevice, hence including only the aluminium dissolution reaction (*i.e.*, anodic reaction) on the steel surface was thought to be valid, as the cathodic reactions could be assumed to occur on the outer aluminium surface where oxygen was still present (Vankeerberghen 2004).

### **2.3.6 Heppner et al. (2004)**

The numerical model developed by Heppner et al. (2004) focused on the initiation of crevice corrosion of two different types of metals, stainless steel and pure titanium, which were separately immersed in NaCl solutions. The governing equation used in this model included Poisson's equation, which represented the charge distribution in the solution, migration under potential gradients, diffusion under concentration gradients, and a sink/source chemical reaction term that was obtained through a set of chemical equilibrium relations. Thirteen chemical equilibrium relationships were assumed to occur in the stainless steel crevice solution, while four relations were assumed for the case with titanium. In addition, all of these equilibrium relations included chemical activities that were calculated using the Pitzer model (Pitzer 1991); the Pitzer model is further discussed in Chapter 3.1 of this thesis. As presented in Figure 2.11, metal was dissolved into the solution from the interior crevice surfaces and this anodic reaction rate was governed by Faraday's law (Perez 2004). Furthermore, the hydrogen evolution reaction occurring on the metal surface was equal to the anodic reaction rate as per the mixed potential theory (Perez 2004). These electrochemical reactions involving metal dissolution and hydrogen evolution were included in the migration term of the governing equations. A zero concentration flux was applied for all species at the crevice surfaces, and bulk concentrations were defined at the crevice mouth.

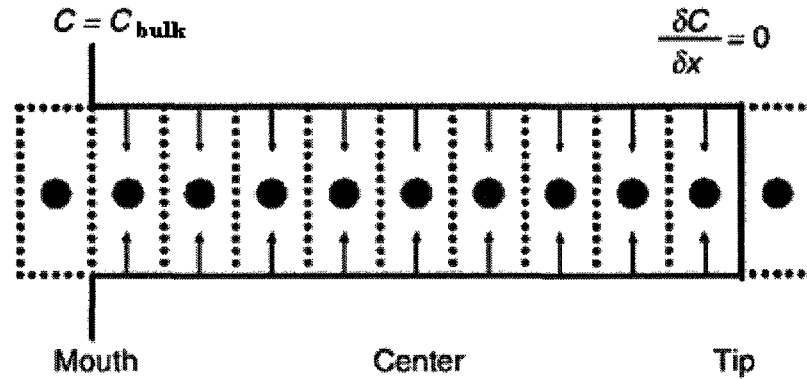


**Figure 2.11.** Finite element domain used to simulate the initiation stage of crevice corrosion. The small arrows represent metal ion dissolution. (taken from Heppner et al. 2004).

### 2.3.7 Summary

All the numerical models presented in this chapter follow the same general structure: (1) The electrochemical reaction rates on the metal surface are based on Faraday's law, which is a function of current density. (2) The governing equation that describes the transport processes of the modelled species in the solution consist of a various groupings of diffusion, migration, advection and chemical activity. (3) The charge distribution in the solution is defined using either Poisson's equation, or an electro-neutrality condition. (4) The treatment of the chemical reactions in the solution depends on the rate of the reaction: if the rates are large in comparison with other transport processes a chemical equilibrium assumption is made, otherwise the reaction is added as a sink/source term in the governing transport equations. (5) Boundary conditions for bulk solutions are defined as fixed concentrations and electric potential, while the crevice/pit surfaces are defined as flux terms that depend on the current on the metal surface.

## **2.4. Key observations obtained from the literature review**

The key observations obtained from the literature review can be summarized as follows:

- The variability in the chloride threshold of carbon steel rebar can be partially attributed to the surface conditions of the rebar, in particular, the presence of mill scale. It was demonstrated that mill scales on carbon steel rebar are not uniform and show significant variability.
- It was suggested that the pore solution chemistry in the crevices between the mill scale and the steel surface may be different from that of the bulk pore solution, and this difference may create the necessary conditions for the breakdown of the passive film on the steel surface within a mill scale crevice.
- The passive current density on the pristine (with no mill scale or deformities) carbon steel surface is typically in the order of  $10^{-3}$  A/m<sup>2</sup>; however it has been shown that it is affected by the alkalinity of the pore solution (higher alkalinity implies higher passive current density) and the presence of chlorides in the pore solution. It was observed that, up to a certain chloride concentration in the pore solution, the passive current density remains relatively constant; however, beyond this level, it increases. Literature on the pattern of increase (*i.e.*, sudden vs. gradual) is not conclusive.
- Literature on the models that simulate the chemistry of the electrolytes in local zones on the metal or alloy surfaces showed that it is necessary to incorporate multiple mechanisms of transport (e.g. diffusion, electrical migration and advection) to achieve realistic simulations; however, the types of transport mechanism to be used in each model is specific to the case that is being studied. For example, it is not

necessary to include transport by advection if the electrolyte within the domain is not moving.

- Activity of the species in the electrolyte may become important when the ionic strength of the solution is relatively large; therefore, the need for the inclusion of chemical activity effect in the present work needs to be studied.

### 3) Modelling Theory and Its Implementation

This chapter presents the governing differential equations that describe the transport of species in concrete pore solution within mill scale cracks and crevices, the chemical reaction constraints that are enforced in the domain to describe accurately interactions within the pore solution, and the initial and boundary conditions of the modelled domain.

#### 3.1 Governing equations

The transport of ionic, solid and gaseous species within the concrete pore solution can be modelled using the mass conservation equation (Samson et al. 1999c):

$$\frac{\partial c_i}{\partial t} + \nabla \cdot (\mathbf{N}_i) = 0 \quad (3.1)$$

where subscript  $i$  is the index representing each ionic (*i.e.*, OH<sup>-</sup>, Fe<sup>2+</sup>, Ca<sup>2+</sup>, Cl<sup>-</sup>, Na<sup>+</sup>, K<sup>+</sup>), and gaseous (*i.e.*, O<sub>2(g)</sub>) species modelled;  $c_i$  (mol/m<sup>3</sup>) is the concentration of species in the ionic or in the gaseous state;  $t$  (s) is time; and  $\mathbf{N}_i$  is the total flux of species. The total flux term,  $\mathbf{N}_i$ , in equation (3.1) can be expressed as

$$\mathbf{N}_i = c_i \mathbf{v}_i \quad (3.2)$$

where  $\mathbf{v}_i$  (m/s) is the velocity of the net flow of species (Li and Page 1998):

$$\mathbf{v}_i = -\frac{D_i}{RT} \nabla \bar{\mu}_i \quad (3.3)$$

In equation (3.3),  $D_i$  (m<sup>2</sup>/s) is the diffusion coefficient for the species in water,  $R$  is the ideal gas constant (8.3143 J/mol/K),  $T$  (K) is the temperature and  $\bar{\mu}_i$  is the electrochemical potential (Li and Page 1998):

$$\bar{\mu}_i = \mu_i^\circ + RT \ln(\gamma_i c_i) + z_i F \phi \quad (3.4)$$

where  $\mu_i^\circ$  is the chemical potential in the standard state (*i.e.*, temperature of 298.15 K, or 25°C, and an absolute pressure of 101.325 kPa, 1 atm.),  $z_i$  is the valence of the ionic species (see Table 3.1),  $F$  is Faraday's constant (96,488 C/mol),  $\phi$  (V) is the electric potential, and  $\gamma_i$  is the chemical activity coefficient for the various ionic species in water, which depends on the ionic strength,  $I$  (mol/m<sup>3</sup>), of the solution:

$$I = 0.5 \sum_{i=1}^{n_s} z_i^2 c_i \quad (3.5)$$

**Table 3.1:** Valence and radii of the ionic species modelled in the study (Dean 1999).

Species	Valence, $z_i$	Radii, $a_i$ (10 <sup>-10</sup> m)
OH <sup>-</sup>	-1	3.5
Fe <sup>2+</sup>	2	6
Ca <sup>2+</sup>	2	6
Cl <sup>-</sup>	-1	3
Na <sup>+</sup>	1	4
K <sup>+</sup>	1	3

When dealing with solutions with low ionic strength, the chemical activity coefficient,  $\gamma_i$ , can be approximated as one; however, as the overall ionic concentration increases in the solution, more ionic interactions are likely to occur; this, in turn, causes the chemical activity coefficient to gradually deviate from unity (Samson et al. 1999b). For the solutions studied in this study, it was found that an ionic strength up to 1.5 mol/m<sup>3</sup> would

result in less than 10 % difference in the chemical activity coefficients (*i.e.*,  $\gamma_i \geq 0.9$ ). There are models, such as the Debye-Hückel model (Debye and Hückel 1923) and Davies equation (Davies 1967), that can be used to calculate the chemical activity coefficient; however, these models are only valid for ionic strengths up to 10 mol/m<sup>3</sup> and 500 mol/m<sup>3</sup>, respectively, and concrete pore solutions typically have ionic strengths over 500 mol/m<sup>3</sup> (Samson et al. 1999b). Samson and Marchand (2007) proposed a modified version of Davies equation (Davies 1967) to calculate the chemical activity coefficients of a given ionic species in concrete pore solution such that:

$$\ln \gamma_i = -\frac{Az_i^2 \sqrt{I}}{1 + a_i B \sqrt{I}} + \frac{(0.2 - 4.17 \times 10^{-5} I) Az_i^2 I}{\sqrt{1000}} \quad (3.6)$$

In equation (3.6),  $a_i$  (m) is the radii of the ions given in Table 3.1,  $A$  and  $B$  are temperature dependent parameters defined as:

$$A = \frac{\sqrt{2} F^2 e_0}{8\pi(\epsilon RT)^{3/2}} \quad (3.7)$$

$$B = \sqrt{\frac{2F^2}{\epsilon RT}} \quad (3.8)$$

where  $e_0$  is the charge of one electron ( $1.602 \times 10^{-19}$  C) and  $\epsilon$  is the permittivity of the medium, which was assumed in this study to be the same as water ( $7.092 \times 10^{-10}$  C<sup>2</sup>/N/m<sup>2</sup>).

The modified Davies equation (3.6) can accurately predict single ion activity coefficient of concrete pore solutions made of monovalent and divalent ions up to an ionic strength of 1200 mol/m<sup>3</sup> (Samson et al. 1999b). In this model, 11 different solutions were analyzed (see Tables 3.2 and 3.3), and their ionic strengths varied from 47 to 1551 mol/m<sup>3</sup>. Two of these solutions (*i.e.*, solutions 1 and 2 in Table 3.3) had ionic strengths

that were greater than the limit proposed by Samson et al. (1999b), but for consistency, the activity coefficients of species in these cases were also calculated using the same approach. The Pitzer Ion Interaction model (Pitzer 1991) can accurately predict single ion activity coefficient for ionic strengths up to 6000 mol/m<sup>3</sup>, but not all ion interaction parameters that are used in this model can be found in the literature; therefore it was not used in the present study.

Using equations (3.3) and (3.4) in equation (3.2),  $N_i$  can be re-written as (Li and Page 1998):

$$N_i = -D_i \nabla c_i - \frac{D_i z_i F}{RT} c_i \nabla \phi - D_i c_i \frac{\nabla \gamma_i}{\gamma_i} \quad (3.9)$$

By substituting equation (3.9) into equation (3.1), the extended Nernst-Planck equation, which is the governing differential equation used in this study to model the transport of species in the concrete pore solution, can be established (Samson et al. 1999a):

$$\frac{\partial c_{is}}{\partial t} + \frac{\partial c_i}{\partial t} + \nabla \cdot \left( \underbrace{-D_i \nabla c_i}_{\text{Diffusion}} - \underbrace{\frac{D_i z_i F}{RT} c_i \nabla \phi}_{\text{Electrical Migration}} - \underbrace{D_i c_i \nabla (\ln \gamma_i)}_{\text{Chemical Activity}} \right) = 0 \quad (3.10)$$

where  $c_{is}$  (mol/m<sup>3</sup>) is the concentration of the stationary species in solid state (*i.e.*, the components Fe<sub>(s)</sub> and OH<sub>(s)</sub> as they exist in Fe(OH)<sub>2(s)</sub>) and  $\partial c_{is} / \partial t$  is the sink/source term that accounts for the exchange between the solid and ionic species in the concrete pore solution; *i.e.*, the exchange between Fe<sub>(s)</sub> and Fe<sup>+2</sup>, and the exchange between OH<sub>(s)</sub> and OH<sup>-</sup>. For all other species,  $\partial c_{is} / \partial t$  was set to zero. The interactions within the concrete pore solution are discussed in further detail in Section 3.2.

In equation (3.10), there are three mechanisms that are used to describe the flux of species in concrete pore solution: diffusion, electrical migration and chemical activity. Advection flux was not considered as part of the total flux of species because the analysis domain was assumed to be fully saturated with the concrete pore solution that is stationary. The diffusion term in the total flux expression represents the movement of species based on a concentration gradient. Although there was no external current applied to the system, the diffusion of ions within the pore solution creates electric potential gradients since different ions move at different velocities, and this, in turn, leads to an imbalance in the electro-neutrality of the system. These potential gradients,  $\nabla\phi$ , through the electrical migration term in equation (3.10), slows down the faster ions while accelerating the slower ions so that electro-neutrality of the system is maintained (Samson et al. 1999c). The potential gradients change over time, and they need to be calculated for each time step during the numerical solution of equation (3.10); therefore, in this study, equation (3.10) was coupled with the Poisson's equation that directly relates the electric potential distribution with the electric charge distribution in the concrete pore solution (Samson and Marchand 1999):

$$\nabla^2\phi + \frac{F}{\varepsilon} \sum_{i=1}^{n_s} z_i c_i = 0 \quad (3.11)$$

where  $n_s$  refers to the total number of ionic species. Finally, the chemical activity term in equation (3.10) represents the ion-ion and ion-solvent interactions that take place in an ionic solution. Ion-ion interactions may reduce the mobility of certain ions in solutions due to the fact that opposite charges attract, hence an ion of a given charge moving in the solution will have oppositely charged ions attaching themselves around it (Samson et al.

1999b). Ion-solvent interactions may also reduce the mobility of ions in a solution, but this interaction is caused by ions dragging solvent (e.g. water) molecules with them as they move in the solution (Samson et al. 1999b). The effect of chemical activity on the overall transport of species is investigated further in Section 3.8.

### **3.2 Chemical reaction constraints**

In this study, the simulations were carried out in two pore solutions named CH and CP. The label “CH” refers to a saturated calcium hydroxide,  $\text{Ca}(\text{OH})_2$ , solution with pH of 12.5, where “C” stands for calcium and “H” stands for hydroxide. The solution referred as “CP”, where “C” stands for concrete and “P” stands for pore, was composed of calcium hydroxide (at saturation), sodium hydroxide (NaOH) and potassium hydroxide (KOH). The CP solution, which contained typical concentrations of different anions and cations that can be found in ordinary portland cement concrete pore solution, had a pH of 13.5. Initial chemical compositions of the CH and CP solutions are provided in Section 3.3.

For the CH solution, the numerical analysis of equations (3.6), (3.10) and (3.11) within the domain (see Section 3.4), with the imposed constraints (see Section 3.2), initial (see Section 3.3) and boundary conditions (see Section 3.4), provide the solutions for 8 concentrations ( $c_{\text{OH}^-}$ ,  $c_{\text{OH}(s)}$ ,  $c_{\text{Fe}^{2+}}$ ,  $c_{\text{Fe}(s)}$ ,  $c_{\text{Ca}^{2+}}$ ,  $c_{\text{Cl}^-}$ ,  $c_{\text{Na}^+}$ ,  $c_{\text{O}_2}$ ), 5 chemical activity values ( $\gamma_{\text{OH}^-}$ ,  $\gamma_{\text{Fe}^{2+}}$ ,  $\gamma_{\text{Ca}^{2+}}$ ,  $\gamma_{\text{Cl}^-}$ ,  $\gamma_{\text{Na}^+}$ ) and electric potential ( $\phi$ ) over time. For the CP solution, which contained an additional extended Nernst-Planck and modified Davies equation for the  $\text{K}^+$  ions, the following additional variables were also solved: ( $c_{\text{K}^+}$ ,  $\gamma_{\text{K}^+}$ ).

In the following sections, these chemical reaction constraints, the domain of analysis, and initial and boundary conditions are presented.

It was also assumed in this study that the anodic and cathodic micro-cell reactions on the passive steel surface were, respectively, iron dissolution from the steel surface to the concrete pore solution and the reduction of dissolved oxygen in the pore solution:



In the finite element simulations, equations (3.12) and (3.13) were assumed to take place simultaneously at every point on the steel surface (Bertolini et al. 2004).

For these simulations, calcium ( $Ca^{2+}$ ) and iron ( $Fe^{+2}$ ) ions in the pore solution were assumed to only react with hydroxides ( $OH^{-}$ ) to form solid calcium hydroxide and solid iron hydroxide as per equations (3.14) and (3.15), respectively. This simplification was done because of the concern that auxiliary ions would complicate the chemistry within mill scale crevices such that it would be difficult to carry out a parametric study to investigate the effects of the variations in basic parameters such as passive current density and domain size.



where  $K_{sp1}$  and  $K_{sp2}$  are the solubility product constants, which were taken in this study as  $5500 \text{ mol}^3/\text{m}^9$  and  $4.87 \times 10^{-8} \text{ mol}^3/\text{m}^9$ , respectively (Dean 1999). The stoichiometric

balance among the solid species of equation (3.14) and (3.15) require that in the bulk concrete pore solution the following constraint exists:

$$c_{Fe(s)} + c_{Ca(s)} = 0.5 \times c_{OH(s)} \quad (3.16)$$

This constraint is satisfied at all times within the bulk concrete pore solution; the initial conditions (see Section 3.3) and the bulk boundary conditions (see Section 3.4) were calculated using equations (3.14), (3.15) and (3.16). However, experimental studies (Glasser et al. 2008, Marinoni et al. 2008, Jain and Neithalath 2009, and Ghods 2009) have shown that  $Ca(OH)_{2(s)}$  was not detectable near the steel surface when concrete was exposed to a corrosive environment. This is understandable since the solubility product constant for  $Ca(OH)_{2(s)}$  is almost 11 orders of magnitude larger than that of  $Fe(OH)_{2(s)}$ , the concentrations of  $Ca_{(s)}$  and  $OH_{(s)}$  from  $Ca(OH)_{2(s)}$  were significantly smaller than the concentrations of  $Fe_{(s)}$  and  $OH_{(s)}$  from  $Fe(OH)_{2(s)}$ . Furthermore, due to the fact that the solid species were treated as sink/source terms in the extended Nernst-Planck equation (3.10), imposing equation (3.16) as a constraint resulted in negative  $Ca_{(s)}$  concentrations within the analysis domain (*i.e.*, mill scale crack and crevice), which was not realistic. To overcome this numerical problem, and to model more realistically the pore solution chemistry within the domain of analysis, it was assumed that  $Ca(OH)_{2(s)}$  was consumed within the mill scale crack and crevice such that the following constraint can be used instead of equation (3.16):

$$c_{Fe(s)} = 0.5 \times c_{OH(s)} \quad (3.17)$$

It should also be noted that the reaction rates of the reversible reactions (3.14) and (3.15) were assumed to be large in comparison to the rate of transport of species involved (Rubin 1983). Accordingly, reactions (3.14) and (3.15) required the following two

solubility relations be satisfied simultaneously at every node in the domain (Barbarulo 2000):

$$\gamma_{Ca^{2+}} c_{Ca^{2+}} (\gamma_{OH^-} c_{OH^-})^2 = K_{sp1} \quad (3.18)$$

$$\gamma_{Fe^{2+}} c_{Fe^{2+}} (\gamma_{OH^-} c_{OH^-})^2 = K_{sp2} \quad (3.19)$$

These two solubility relations must be satisfied at every node in the pore solution when their respective solid compound (*i.e.*,  $Ca(OH)_{2(s)}$  for equation (3.18) and  $Fe(OH)_{2(s)}$  for equation (3.19)) is present in the concrete pore solution.

### 3.3 Initial conditions

At the beginning of the simulations it was assumed that the pore solution composition within the mill scale crack and crevice was equal to the composition of the bulk concrete pore solution. Dissolved oxygen concentration in both CH and CP pore solutions was assumed to be equal to  $0.15 \text{ mol/m}^3$  (Isgor and Razaqpur 2006), and the concentrations of  $Fe_{(s)}$  and  $OH_{(s)}$  from  $Fe(OH)_{2(s)}$  were assumed to be  $0 \text{ mol/m}^3$ .

For the CH solution, the simulations required the solution of governing equations described in Section 3.1 when the bulk pore solution contained externally added NaCl salt at different concentrations. When NaCl is present in the bulk pore solution, the electro-neutrality condition requires that the following condition must be satisfied at all times:

$$z_{OH^-} c_{OH^-} + z_{Fe^{2+}} c_{Fe^{2+}} + z_{Ca^{2+}} c_{Ca^{2+}} + z_{Cl^-} c_{Cl^-} + z_{Na^+} c_{Na^+} = 0 \quad (3.20)$$

In equation (3.20), since  $Cl^-$  and  $Na^+$  ions come only from NaCl salt, the electro-neutrality of these two ions are satisfied such that:

$$z_{Cl^-}c_{Cl^-} + z_{Na^+}c_{Na^+} = 0 \quad (3.21)$$

Note that  $|z_{Cl^-}| = |z_{Na^+}| = 1$ . The initial concentrations of  $Cl^-$  and  $Na^+$  in this study were explicitly defined based on the amount of NaCl salt that was present in each simulation. Due to the condition given in equation (3.21), equation (3.20) can be re-written as:

$$z_{OH^-}c_{OH^-} + z_{Fe^{2+}}c_{Fe^{2+}} + z_{Ca^{2+}}c_{Ca^{2+}} = 0 \quad (3.22)$$

If the hydroxide concentrations,  $c_{OH^-}$ , in equations (3.18) and (3.19) are substituted in equation (3.22), the following expression can be obtained after the valence values (*i.e.*,  $z_{OH^-} = -1$ ;  $z_{Fe^{2+}} = 2$ ;  $z_{Ca^{2+}} = 2$ ) are used:

$$c_{OH^-} = \left( \frac{2K_{sp1}}{\gamma_{Ca^{2+}}\gamma_{OH^-}^2} + \frac{2K_{sp2}}{\gamma_{Fe^{2+}}\gamma_{OH^-}^2} \right)^{1/3} \quad (3.23)$$

Since the activity coefficients and concentrations of species are related to each other (through the modified Davies equation), the solution of  $c_{OH^-}$ ,  $c_{Fe^{2+}}$  and  $c_{Ca^{2+}}$  required an iterative approach. In the first iteration, the activity terms ( $\gamma_{OH^-}$ ,  $\gamma_{Fe^{2+}}$  and  $\gamma_{Ca^{2+}}$ ) were assumed to be unity. Once the hydroxide concentration was determined from equation (3.23), the concentration of the calcium and iron ions could be calculated from equations (3.18) and (3.19), respectively. In the subsequent iterations, the chemical activity coefficients of all ionic species were calculated using the modified Davies equation (3.6); and these revised chemical activity coefficients were used in equations (3.23), (3.18) and (3.19) to solve for the concentrations  $c_{OH^-}$ ,  $c_{Fe^{2+}}$  and  $c_{Ca^{2+}}$ . At the end of each iteration, the concentration of these three ions were compared with the concentrations from the previous iteration, and iterations were continued until the concentrations from the last iteration were equal, up to four significant figures, to the previous concentrations.

A similar iterative procedure was used for the CP solution. The main difference in the iteration schemes for the two solutions originates from the electro-neutrality condition:

$$z_{OH^-}c_{OH^-} + z_{Fe^{2+}}c_{Fe^{2+}} + z_{Ca^{2+}}c_{Ca^{2+}} + z_{Cl^-}c_{Cl^-} + z_{Na^+}c_{Na^+} + z_{K^+}c_{K^+} = 0 \quad (3.24)$$

As discussed previously, the CP solution contained calcium hydroxide ( $Ca(OH)_2$ ), potassium hydroxide (KOH) and sodium hydroxide (NaOH). The simulations required the solution of governing equations described in Section 3.1 when the bulk pore solution contained externally added NaCl salt at different concentrations, but, unlike the case for the CH solution,  $Na^+$  ions in the CP solution came from both NaCl and NaOH compounds; therefore the electro-neutrality condition given in equation (3.21) cannot be used. Substituting equations (3.18) and (3.19) into equation (3.24) and using the valence values (*i.e.*,  $z_{OH^-} = -1$ ;  $z_{Fe^{2+}} = 2$ ;  $z_{Ca^{2+}} = 2$ ;  $z_{Cl^-} = -1$ ;  $z_{Na^+} = 1$ ;  $z_{K^+} = 1$ ) gave the following expression:

$$-c_{OH^-}^3 + c_{OH^-}^2(-c_{Cl^-} + c_{Na^+} + c_{K^+}) + \frac{2K_{sp1}}{\gamma_{Ca^{2+}}\gamma_{OH^-}^2} + \frac{2K_{sp2}}{\gamma_{Fe^{2+}}\gamma_{OH^-}^2} = 0 \quad (3.25)$$

Since the activity coefficients and concentrations of species are related to each other (through the modified Davies equation), the solution of  $c_{OH^-}$ ,  $c_{Fe^{2+}}$  and  $c_{Ca^{2+}}$  required an iterative approach. The initial concentrations of  $Cl^-$ ,  $Na^+$  and  $K^+$  ions were explicitly defined based on the amount of NaCl, NaOH and KOH present in the CP solution, and these quantities were substituted in equation (3.25). In the first iteration, the activity terms ( $\gamma_{OH^-}$ ,  $\gamma_{Fe^{2+}}$  and  $\gamma_{Ca^{2+}}$ ) were assumed to be unity. Once the hydroxide concentration was determined from equation (3.25), the concentration of the calcium and iron ions could be calculated from equations (3.18) and (3.19), respectively. In the

subsequent iterations, the chemical activity coefficients of all ionic species were calculated using the modified Davies equation (3.6); and these revised chemical activity coefficients were used in equations (3.25), (3.18) and (3.19) to solve for the concentrations  $c_{OH^-}$ ,  $c_{Fe^{2+}}$  and  $c_{Ca^{2+}}$ . At the end of each iteration, the concentration of these three ions were compared with the concentrations from the previous iteration, and iterations were continued until the concentrations from the last iteration were equal, up to four significant figures, to the previous concentrations.

Since the simulations in this study have been carried out for various chloride concentrations, the initial concentrations, chemical activity coefficients and activities of the species at different chloride concentrations in the CH and CP bulk solutions are provided in Tables 3.2 and 3.3, respectively. In Table 3.2, the ionic concentrations of  $OH^-$ ,  $Fe^{2+}$  and  $Ca^{2+}$  are shown to increase and the corresponding chemical activity coefficients decrease as the ionic strength increase from 47 to 557 mol/m<sup>3</sup> (*i.e.*, solution no. 5 to 1). In Table 3.3, an increase in the ionic strength from 301 to 426 mol/m<sup>3</sup> (*i.e.*, solution no. 6 to 5) follows the same trend as before; however, as the ionic strength increase from 801 to 1551 mol/m<sup>3</sup> (*i.e.*, solution no. 4 to 1) the ionic concentrations of the species decrease, while their activity coefficients increase. This change in the trend can be explained by the fact that there are reduced amounts of free water molecules present to solvate the ions in the solution at the high ionic strengths (*i.e.*, greater than approximately 600 mol/m<sup>3</sup> for this study) (Samson et al. 1999b).

**Table 3.2:** Concentrations, activity coefficients and activities of species in the bulk CH solution (\*).

Concentration, $c_i$ (mol/m <sup>3</sup> )						Ionic Strength (mol/m <sup>3</sup> )
Solution n <sup>o</sup>	Cl <sup>-</sup>	OH <sup>-</sup>	Fe <sup>2+</sup>	Ca <sup>2+</sup>	Na <sup>+</sup>	
1	500	38.291	1.70x10 <sup>-10</sup>	19.145	500	557
2	125	36.320	1.61x10 <sup>-10</sup>	18.160	125	179
3	100	35.773	1.58x10 <sup>-10</sup>	17.887	100	154
4	50	34.202	1.51x10 <sup>-10</sup>	17.101	50	101
5	0	31.311	1.39x10 <sup>-10</sup>	15.656	0	47
Activity coefficient, $\gamma_i$						
Solution n <sup>o</sup>	Cl <sup>-</sup>	OH <sup>-</sup>	Fe <sup>2+</sup>	Ca <sup>2+</sup>	Na <sup>+</sup>	
1	0.6841	0.7065	0.3925	0.3925	0.7268	
2	0.7393	0.7511	0.4069	0.4069	0.7621	
3	0.7489	0.7597	0.4163	0.4163	0.7697	
4	0.7756	0.7838	0.4475	0.4475	0.7915	
5	0.8243	0.8291	0.5212	0.5212	0.8336	
Activity, $c_i\gamma_i/\gamma_0^{(**)}$						
Solution n <sup>o</sup>	Cl <sup>-</sup>	OH <sup>-</sup>	Fe <sup>2+</sup>	Ca <sup>2+</sup>	Na <sup>+</sup>	
1	342.05	27.05	6.67x10 <sup>-11</sup>	7.51	363.40	
2	92.41	27.28	6.55x10 <sup>-11</sup>	7.39	95.26	
3	74.89	27.18	6.58x10 <sup>-11</sup>	7.45	76.97	
4	38.78	26.81	6.76x10 <sup>-11</sup>	7.65	39.58	
5	0	25.96	7.24x10 <sup>-11</sup>	8.16	0	

(\*) The amount of NaCl added in each case corresponds to the concentration of Cl<sup>-</sup> (or Na<sup>+</sup>).

(\*\*)  $\gamma_0 = 1 \text{ mol/m}^3$

**Table 3.3:** Concentrations, activity coefficients and activities of species in the bulk CP solution (\*).

Concentration, $c_i$ (mol/m <sup>3</sup> )							Ionic Strength (mol/m <sup>3</sup> )
Solution n <sup>o</sup>	Cl <sup>-</sup>	OH <sup>-</sup>	Fe <sup>2+</sup>	Ca <sup>2+</sup>	Na <sup>+</sup>	K <sup>+</sup>	
1	1250	300.490	2.17x10 <sup>-12</sup>	0.245	1350	200	1551
2	1000	300.516	2.29x10 <sup>-12</sup>	0.258	1100	200	1301
3	750	300.552	2.44x10 <sup>-12</sup>	0.276	850	200	1051
4	500	300.592	2.62x10 <sup>-12</sup>	0.296	600	200	801
5	125	300.621	2.75x10 <sup>-12</sup>	0.311	225	200	426
6	0	300.597	2.64x10 <sup>-12</sup>	0.299	100	200	301
Activity coefficient, $\gamma_i$							
Solution n <sup>o</sup>	Cl <sup>-</sup>	OH <sup>-</sup>	Fe <sup>2+</sup>	Ca <sup>2+</sup>	Na <sup>+</sup>	K <sup>+</sup>	
1	0.6696	0.7065	0.4980	0.4980	0.7392	0.6696	
2	0.6712	0.7053	0.4741	0.4741	0.7357	0.6712	
3	0.6726	0.7035	0.4457	0.4457	0.7311	0.6726	
4	0.6756	0.7027	0.4164	0.4164	0.7270	0.6756	
5	0.6937	0.7132	0.3853	0.3853	0.7308	0.6937	
6	0.7098	0.7259	0.3868	0.3868	0.7406	0.7098	
Activity, $c_i\gamma_i / \gamma_0^{(**)}$							
Solution n <sup>o</sup>	Cl <sup>-</sup>	OH <sup>-</sup>	Fe <sup>2+</sup>	Ca <sup>2+</sup>	Na <sup>+</sup>	K <sup>+</sup>	
1	837.00	212.30	1.08x10 <sup>-12</sup>	0.12	997.92	133.92	
2	671.20	211.95	1.09x10 <sup>-12</sup>	0.12	809.27	134.24	
3	504.45	211.44	1.09x10 <sup>-12</sup>	0.12	621.44	134.52	
4	337.80	211.23	1.09x10 <sup>-12</sup>	0.12	436.20	135.12	
5	86.71	214.40	1.06x10 <sup>-12</sup>	0.12	164.43	138.74	
6	0	218.20	1.02x10 <sup>-12</sup>	0.12	74.06	141.96	

(\*) CP solution contains 100 mol/m<sup>3</sup> NaOH and 200 mol/m<sup>3</sup> KOH. The amount of NaCl added in each case corresponds to the concentration of Cl<sup>-</sup>.

(\*\*)  $\gamma_0 = 1 \text{ mol/m}^3$

### 3.4 Domain and boundary conditions

Figure 3.1 illustrates the axi-symmetrical domain and boundary conditions of a typical simulation, representing the crack in the mill scale and crevice between the mill scale and

the steel surface. In the figure, boundary 1 is the opening of the mill scale crack to the concrete pore solution; boundary 2 is the axis of symmetry; boundary 3 is the steel surface; and boundaries 4, 5 and 6 represent the mill scale surfaces.

The dimensions of the domain in the simulations presented in this study have been established based on microscopic observations by Ghods (2009), who reported different ranges for the thickness and length of mill scale cracks and crevices. In these microscopic studies, the mill scale crack thickness and crevice length were shown to vary significantly, while the mill scale crack length and crevice thickness were not varying much; thus, in the present study (Chapter 4) the mill scale crack length ( $l$ ) and crevice thickness ( $t_c$ ) were fixed at  $5 \times 10^{-5}$  and  $1 \times 10^{-6}$  m, respectively, for all cases investigated, while the mill scale crack thickness ( $t$ ) was set at values ranging between  $1 \times 10^{-5}$  to  $1 \times 10^{-7}$  m, and the crevice length ( $c$ ) was set at values ranging between  $3 \times 10^{-3}$  to  $1 \times 10^{-4}$  m.

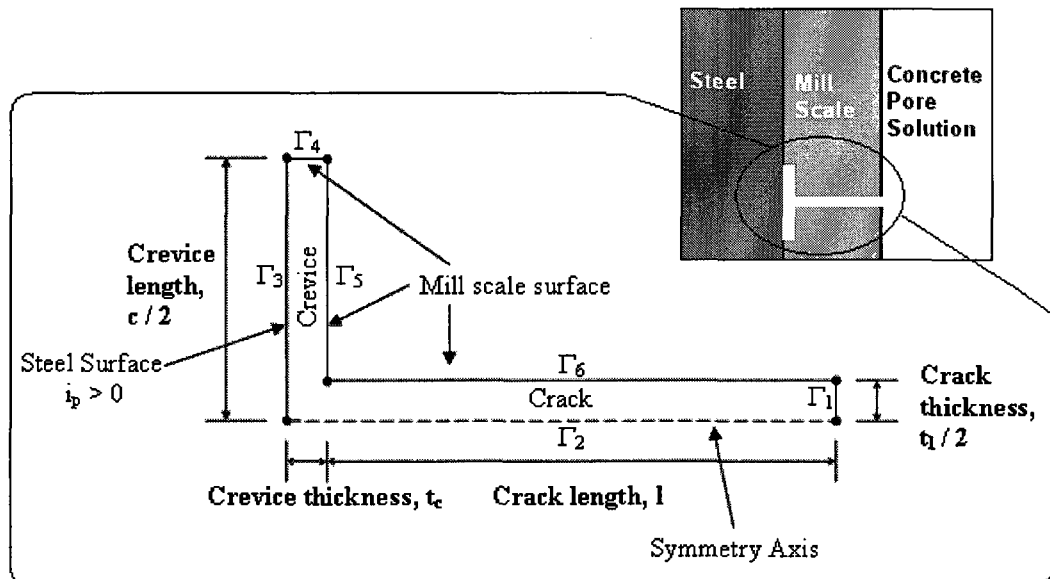


**Figure 3.1.** The solution domain representing the crack in the mill scale and the crevice between the surface of steel and mill scale.

### 3.4.1 Boundary conditions for the extended Nernst-Planck equations

Boundary 1 represents the opening of the crack to the bulk concrete pore solution, in which concentrations of species were assumed to remain constant; therefore, for boundary 1, Dirichlet boundary conditions were defined based on the assumed concentration levels in the bulk concrete pore solution. During the implementation of the Dirichlet boundary conditions, there were some issues regarding the convergence of the solution for the extended Nernst-Planck equation. This originated from the fact that, in the beginning of the analysis (*i.e.*, at  $t = 0$  s), the bulk concrete pore solution had  $\text{Cl}^-$  ions (see Tables 3.2 and 3.3) while the mill scale crack and the crevice (*i.e.*, the actual analysis domain in Figure 3.1) was free from chloride. When large chloride concentrations were applied as Dirichlet conditions on boundary 1, the boundary-value problem became significantly nonlinear because of the large gradients at boundary 1, causing convergence issues. To overcome this problem, the chloride concentration at boundary 1 was not set to its actual value at  $t = 0$  s, but it was linearly increased from 0 to its desired value over 3600 s, during which all other Dirichlet conditions for other species on boundary 1 were calculated using the same iterative procedure described in Section 3.3.

The boundary conditions for the steel and mill scale surfaces (*i.e.*, boundaries 2-6) during the solution of the extended Nernst-Planck equations (3.10) were defined as Neumann conditions (see Section 2.3.7):

$$\mathbf{n} \cdot \mathbf{N}_i = \frac{i}{n_e F} \quad (3.26)$$

where  $\mathbf{n}$  is a unit vector with the direction normal to the boundary,  $n_e$  refers to the number of electrons exchanged in the reaction and  $i$  is refers to the current density, representing the rate of electrochemical reactions taking place on the steel surface (Hansson and Sørensen 1990).

The following set of equations was defined on boundary 2 to represent the axis of symmetry:

$$\mathbf{n} \cdot \mathbf{N}_{\text{OH}^-} = 0 \quad \text{on } \Gamma_2 \quad (3.27)$$

$$\mathbf{n} \cdot \mathbf{N}_{\text{Fe}^{2+}} = 0 \quad \text{on } \Gamma_2 \quad (3.28)$$

$$\mathbf{n} \cdot \mathbf{N}_{\text{Ca}^{2+}} = 0 \quad \text{on } \Gamma_2 \quad (3.29)$$

$$\mathbf{n} \cdot \mathbf{N}_{\text{Cl}^-} = 0 \quad \text{on } \Gamma_2 \quad (3.30)$$

$$\mathbf{n} \cdot \mathbf{N}_{\text{Na}^+} = 0 \quad \text{on } \Gamma_2 \quad (3.31)$$

$$\mathbf{n} \cdot \mathbf{N}_{\text{K}^+} = 0 \quad \text{on } \Gamma_2 \quad (3.32)$$

$$\mathbf{n} \cdot \mathbf{N}_{\text{O}_2} = 0 \quad \text{on } \Gamma_2 \quad (3.33)$$

The steel surface (boundary 3) was assumed to be covered with a passive oxide film; therefore, steel was in a passive corrosion state with a corrosion rate equal to the passive current density,  $i_p$ . Chapter 2.1 (Literature Review) provides a background on the range of  $i_p$  for passive steel, and in this study (see Chapter 4), the effect of  $i_p$  on the pore solution chemistry within the mill scale cracks and crevices is investigated. Following equations (3.12) and (3.13), the boundary conditions along the steel surface should represent  $\text{OH}^-$  production,  $\text{Fe}^{2+}$  dissolution and  $\text{O}_2$  depletion in the passive state; therefore, the following Neumann conditions were defined along boundary 3:

$$\mathbf{n} \cdot \mathbf{N}_{\text{OH}^-} = (i_p / F) \text{ on } \Gamma_3 \quad (3.34)$$

$$\mathbf{n} \cdot \mathbf{N}_{\text{Fe}^{2+}} = (i_p / 2F) \text{ on } \Gamma_3 \quad (3.35)$$

$$\mathbf{n} \cdot \mathbf{N}_{\text{Ca}^{2+}} = 0 \text{ on } \Gamma_3 \quad (3.36)$$

$$\mathbf{n} \cdot \mathbf{N}_{\text{Cl}^-} = 0 \text{ on } \Gamma_3 \quad (3.37)$$

$$\mathbf{n} \cdot \mathbf{N}_{\text{Na}^+} = 0 \text{ on } \Gamma_3 \quad (3.38)$$

$$\mathbf{n} \cdot \mathbf{N}_{\text{K}^+} = 0 \text{ on } \Gamma_3 \quad (3.39)$$

$$\mathbf{n} \cdot \mathbf{N}_{\text{O}_2} = -(i_p / 4F) \text{ on } \Gamma_3 \quad (3.40)$$

There is strong evidence that mill scale is conductive (Fujii et al. 1999, Marcotte 2001), hence there could be passive current density associated with the mill scale surfaces, the literature on this subject is still not conclusive. Therefore, a conservative approach was taken in this study such that both cases (*i.e.*, with and without passive current density defined on mill scale surfaces) were analyzed. The following set of equations represents the Neumann conditions of boundaries 4, 5 and 6, for the simulations in which passive current density was defined on mill scale surfaces:

$$\mathbf{n} \cdot \mathbf{N}_{\text{OH}^-} = (i_p / F) \text{ on } \Gamma_4, \Gamma_5 \text{ and } \Gamma_6 \quad (3.41)$$

$$\mathbf{n} \cdot \mathbf{N}_{\text{Fe}^{2+}} = (i_p / 2F) \text{ on } \Gamma_4, \Gamma_5 \text{ and } \Gamma_6 \quad (3.42)$$

$$\mathbf{n} \cdot \mathbf{N}_{\text{Ca}^{2+}} = 0 \text{ on } \Gamma_4, \Gamma_5 \text{ and } \Gamma_6 \quad (3.43)$$

$$\mathbf{n} \cdot \mathbf{N}_{\text{Cl}^-} = 0 \text{ on } \Gamma_4, \Gamma_5 \text{ and } \Gamma_6 \quad (3.44)$$

$$\mathbf{n} \cdot \mathbf{N}_{\text{Na}^+} = 0 \text{ on } \Gamma_4, \Gamma_5 \text{ and } \Gamma_6 \quad (3.45)$$

$$\mathbf{n} \cdot \mathbf{N}_{\text{K}^+} = 0 \text{ on } \Gamma_4, \Gamma_5 \text{ and } \Gamma_6 \quad (3.46)$$

$$\mathbf{n} \cdot \mathbf{N}_{\text{O}_2} = -(i_p / 4F) \quad \text{on } \Gamma_4, \Gamma_5 \text{ and } \Gamma_6 \quad (3.47)$$

When the mill scale was assumed to be non-conductive (hence no electrochemical reactions could take place on mill scale surfaces), Neumann conditions for equations (3.41), (3.42) and (3.47) were set to zero.

### 3.4.2 Boundary conditions for the Poisson equation

The solution of the Poisson's equation (3.11) provides a potential gradient ( $\nabla\phi$ ) in the electrical migration term of the extended Nernst-Planck equation (3.10). Since it was assumed that no external current was applied, for the solution of the Poisson's equation (3.11), all boundaries, except for boundary 1, were represented by the Neumann condition:

$$\mathbf{n} \cdot \nabla\phi = 0 \quad \text{on } \Gamma_2, \Gamma_3, \Gamma_4, \Gamma_5 \text{ and } \Gamma_6 \quad (3.48)$$

Boundary 1 was defined as a Dirichlet condition. Since the ultimate goal of the solution of the Poisson's equation is to solve for the potential gradient ( $\nabla\phi$ ), the value of the Dirichlet condition defined on boundary 1 is not important as long as all other boundaries are defined as "no flux" Neumann conditions; the gradients of the potentials will be the same regardless of the value of the potential used as the Dirichlet condition on boundary 1. For convenience, the Dirichlet condition on boundary 1 was defined as:

$$\phi = 0 \text{ V} \quad \text{on } \Gamma_1 \quad (3.49)$$

### 3.5 Transport properties

The diffusion coefficients of ionic species in the concrete pore solution, which is a water-based solvent, were calculated using Einstein's relation (Dean 1999):

$$D_i = \frac{RTu_i}{z_i F} \quad (3.50)$$

As  $\text{Fe}(\text{OH})_{2(s)}$  precipitates, it progressively occupies more space within the mill scale crack and the crevice; this build-up could cause a decrease in the rate of transport of species. To account for this effect, the diffusion coefficients were assumed to decrease relative to the  $\text{Fe}(\text{OH})_{2(s)}$  concentration at any given point in the analysis domain at a given time. In this model,  $\text{Fe}(\text{OH})_{2(s)}$  was assumed to build up in the space within the mill scale crack and crevice until there was no more space left. Assuming the density of  $\text{Fe}(\text{OH})_{2(s)}$  (molar mass 89.86 g/mol) as 3400 g/l (Dean 1999), the maximum amount of  $\text{Fe}(\text{OH})_{2(s)}$  that can be found in a given volume was calculated as 37,840 mol/m<sup>3</sup>. When the  $\text{Fe}(\text{OH})_{2(s)}$  reaches 37,840 mol/m<sup>3</sup> within a given finite element, the diffusion coefficients of all species in that element were assumed to be very small, typically in a range between 10<sup>-10</sup> and 10<sup>-13</sup> m<sup>2</sup>/s (Bamforth et al. 1997). The diffusion coefficients for all other concentrations of  $\text{Fe}(\text{OH})_{2(s)}$  were linearly interpolated between the maximum and minimum diffusion coefficients (*i.e.*,  $D_{max}$  and  $D_{min}$ ) at  $[\text{Fe}(\text{OH})_{2(s)}] = 0$  and  $[\text{Fe}(\text{OH})_{2(s)}] = 37,840 \text{ mol/m}^3$ , respectively.

Table 3.4 provides diffusion coefficients for different species when  $[\text{Fe}(\text{OH})_{2(s)}] = 0$  and  $[\text{Fe}(\text{OH})_{2(s)}] = 37,840 \text{ mol/m}^3$ , assuming that after the  $\text{Fe}(\text{OH})_{2(s)}$  occupied the entire space of a given finite element, the diffusion coefficients (of all species) would reduce to levels in the order of 10<sup>-13</sup> m<sup>2</sup>/s. In the present study, different assumed values ranging

from  $10^{-11}$  to  $10^{-13}$   $\text{m}^2/\text{s}$  were used to study the effect of  $\text{Fe}(\text{OH})_{2(s)}$  on the pore solution composition.

**Table 3.4:** Transport properties of all species in the concrete pore solutions.

Species	Mobility, $u_i$ ( $10^{-8} \text{ m}^2 \cdot \text{s}^{-1} \cdot \text{V}^{-1}$ ) <sup>(a)</sup>	Diffusion coefficient, $D_{\max_i}$ ( $\text{m}^2/\text{s}$ ) @ $c_{\text{Fe}(s)} = 0$ <sup>(b)</sup>	Diffusion coefficient, $D_{\min_i}$ ( $\text{m}^2/\text{s}$ ) @ $c_{\text{Fe}(s)} 37,840 \text{ mol} / \text{m}^3$ <sup>(c)</sup>
$\text{OH}^-$	20.56	$5.28 \times 10^{-9}$	$5.28 \times 10^{-13}$
$\text{Fe}^{2+}$	5.60	$0.72 \times 10^{-9}$	$0.72 \times 10^{-13}$
$\text{Ca}^{2+}$	6.17	$0.79 \times 10^{-9}$	$0.79 \times 10^{-13}$
$\text{Cl}^-$	7.92	$2.03 \times 10^{-9}$	$2.03 \times 10^{-13}$
$\text{Na}^+$	5.19	$1.33 \times 10^{-9}$	$1.33 \times 10^{-13}$
$\text{K}^+$	7.62	$1.96 \times 10^{-9}$	$1.96 \times 10^{-13}$
$\text{O}_2$	-	$2.20 \times 10^{-9(d)}$	$2.20 \times 10^{-13}$

<sup>(a)</sup> Roberge (2000)

<sup>(b)</sup> Calculated using equation (3.50) assuming  $T = 298 \text{ K}$

<sup>(c)</sup> Assumed values. In the present study, different assumed values ranging from  $10^{-11}$  to  $10^{-13}$   $\text{m}^2/\text{s}$  were used to study the effect of  $\text{Fe}(\text{OH})_{2(s)}$  on the pore solution composition.

<sup>(d)</sup> (Ferrell and Himmelblau 1967, Chuan 2005)

### 3.6 Solution procedure

The boundary-value problem defined in Sections 3.1 to 3.5 was implemented and solved using a commercial finite element analysis software called COMSOL Multiphysics™.

The software has its own mesh generation routines and offers several alternatives for nonlinear and transient solution algorithms, as described in Appendix A.

For the CH solution, the modelling of the problem in COMSOL™ software required the implementation of 6 Nernst-Planck equations (3.10), the Poisson's equation (3.11), 5 modified version of Davies equations (3.6) and 2 chemical reaction constraints: equations (3.17) and (3.19). For the CP solution, the implementation required an additional

extended Nernst-Planck and modified Davies equation for the  $K^+$  ions. All equations were solved using coupled transient and nonlinear solution algorithms. All simulations were carried out at room temperature. Table 3.5 provides a tabulated view of the constants and materials properties that were used in the simulations.

**Table 3.5:** Constants and analysis parameters used in the numerical model.

Parameter	Value	Description
$T$	298 K	Temperature
$R$	8.3143 J/mol/K	Ideal gas constant <sup>a</sup>
$F$	96488 C/mol	Faraday's constant <sup>a</sup>
$K_{sp1}$	$5500 \text{ mol}^3/\text{m}^9$	Solubility product constant of $\text{Ca}(\text{OH})_{2(s)}$ <sup>b</sup>
$K_{sp2}$	$4.87 \times 10^{-8} \text{ mol}^3/\text{m}^9$	Solubility product constant of $\text{Fe}(\text{OH})_{2(s)}$ <sup>b</sup>
$\epsilon_0$	$8.854 \times 10^{-12} \text{ C}^2/\text{N}/\text{m}^2$	Permittivity of the vacuum <sup>c</sup>
$\epsilon_r$	80.1	Dielectric constant of water <sup>c</sup>
$\epsilon$	$7.092 \times 10^{-10} \text{ C}^2/\text{N}/\text{m}^2$	Permittivity of the medium <sup>c</sup>

<sup>(a)</sup> Perez (2004)

<sup>(b)</sup> Dean (1999)

<sup>(c)</sup> Samson and Marchand (2007)

Further details of the implementation of the boundary-value problem described in Sections 3.1 to 3.5 into COMSOL<sup>TM</sup> software are provided in Appendix B and the specific details for individual simulations are provided in Chapter 4. The accuracy of the simulation results provided in Chapter 4 was checked by performing a mesh analysis, as was shown in Appendix C, and the presentation and logic behind these simulations are described in the following section.

### **3.7 Results from a typical simulation**

Due to the number of species analyzed, and since the main results of interest in this study are those of  $\text{OH}^-$  and  $\text{Cl}^-$  ions (*i.e.*, pH and  $\text{Cl}^-/\text{OH}^-$ ), the results for all species analyzed

will not be presented in Chapter 4. In this section, the results of the finite element analysis for a typical simulation will be presented for all species, and the transport patterns will be discussed.

The analysis presented in this section was carried out on a domain with the following dimensions: mill scale crack length ( $l$ ) =  $5 \times 10^{-5}$  m; mill scale crack thickness ( $t_l/2$ ) =  $5 \times 10^{-8}$  m; crevice length ( $c/2$ ) =  $1.5 \times 10^{-3}$  m; crevice thickness ( $t_c$ ) =  $1 \times 10^{-6}$  m. The simulations were carried out in the CP solution; the chloride concentration in the bulk CP solution was  $1250 \text{ mol/m}^3$ . Initial activities in the CP solution (solution no. 1) are given in Table 3.3. A constant passive current density,  $i_p$ , of  $10^{-3} \text{ A/m}^2$  was applied on steel and mill scale surfaces. Diffusion coefficients of species were assumed to linearly decrease from  $D_{max}$  to  $D_{min}$ , as per Table 3.4.

When presenting the movement of ionic species within solutions with high ionic strength, it is more informative to report the results in terms of activities, rather than concentrations; therefore, this approach is used in this thesis. Activity, which is also referred to as effective concentration (Roberge 2000), is calculated by multiplying the ionic concentration,  $c_i$ , of each species by the respective activity coefficient,  $\gamma_i$ . The activities of the ionic species and the concentration of the gaseous species (*i.e.*,  $\text{O}_2$ ) are presented along the mill scale crack (boundary 2) and along the steel surface (boundary 3) after steady-state conditions are reached ( $t = 10^9 \text{ s}$ ) in Figure 3.2. In Figure 3.2a, the activity of hydroxide is shown to be decreasing towards the tip of the crevice (point A). In Figure 3.2b, the activity of chloride is shown to be increasing towards the tip of the

crevice (point A). The steady-state profiles of other ions (i.e.,  $\text{Ca}^{+2}$ ,  $\text{Fe}^{+2}$ ,  $\text{Na}^+$  and  $\text{K}^+$ ) and oxygen concentration are also presented in Figure 3.2.

In order to explain these trends, changes in the activities of hydroxide and chloride, and the change in oxygen concentration, are plotted at the tip of the crevice (i.e., point A, which is the farthest point from the bulk pore solution in Figures 3.2a and 3.2b) over time in Figure 3.3a and 3.3b respectively. It should also be noted that anodic reactions (see equation (3.12)) produce  $\text{Fe}^{+2}$  ions on the steel surface (hence the increase in the activity of  $\text{Fe}^{+2}$  observed in Figure 3.2a), and cathodic reactions (see equation (3.13)) consumes oxygen from the pore solution and produces hydroxide near the steel surface. When anodic and cathodic reactions are in balance, the expected outcome is an increase in the activity of hydroxide; however, as shown in Figure 3.2a, an opposite pattern is observed. It can be seen in Figure 3.3b that, after a short period (around 100 s) during which anodic and cathodic reactions at point A are in balance, the oxygen concentration at point A starts decreasing sharply from its initial condition of  $0.15 \text{ mol/m}^3$  to zero in 20 s. The decrease is mainly due to the oxygen consumption by the cathodic reactions on the steel surface, but accelerated due to the slow diffusion of oxygen from the bulk solution towards the tip of the crevice (point A): the consumed oxygen is not replenished by the oxygen diffusing from the bulk solution. When the oxygen is completely consumed at point A, the cathodic reaction cannot continue there, but the anodic reaction still takes place since electrons produced in the anodic reaction can still be consumed in cathodic reactions on other parts of the steel where the pore solution still contains oxygen. The termination of the cathodic reaction at point A results in the termination of hydroxide

production there; therefore, the hydroxide activity starts to decrease at point A because the  $\text{Fe}^{+2}$  ions produced in the anodic reaction reacts with hydroxides to produce  $\text{Fe}(\text{OH})_{2(s)}$ . Eventually, continued production of  $\text{Fe}^{+2}$  ions and decreased amounts of hydroxide causes an imbalance in the electro-neutrality in the pore solution near point A such that total positive charge becomes larger than total negative charge. This imbalance in electro-neutrality creates a strong electrochemical gradient between the pore solution near point A and the bulk pore solution, which contains large amounts of negatively charged ions such as hydroxides and chlorides; therefore hydroxides and chlorides start moving towards the tip of the crevice (point A) where they are needed to establish electro-neutrality. As it can be seen in Table 3.4, the mobility of chlorides are smaller than that of hydroxides by a factor of  $\sim 3$ ; however, the chloride activity near point A starts increasing sharply, while hydroxide activity decreases, as shown in Figure 3.3a, because hydroxides are continuously being consumed to produce  $\text{Fe}(\text{OH})_{2(s)}$  in the pore solution. The tip of the crevice was selected for the description above since it is the farthest point within the crevice from the bulk pore solution. However, the same mechanism occurs at other parts of the crevice; therefore when steady-state conditions are reached, the profiles given in Figure 3.2 can be plotted along the mill scale crack and crevice boundaries. The result is an increase in the chlorides and a decrease in the hydroxides within the mill scale crack and crevice.

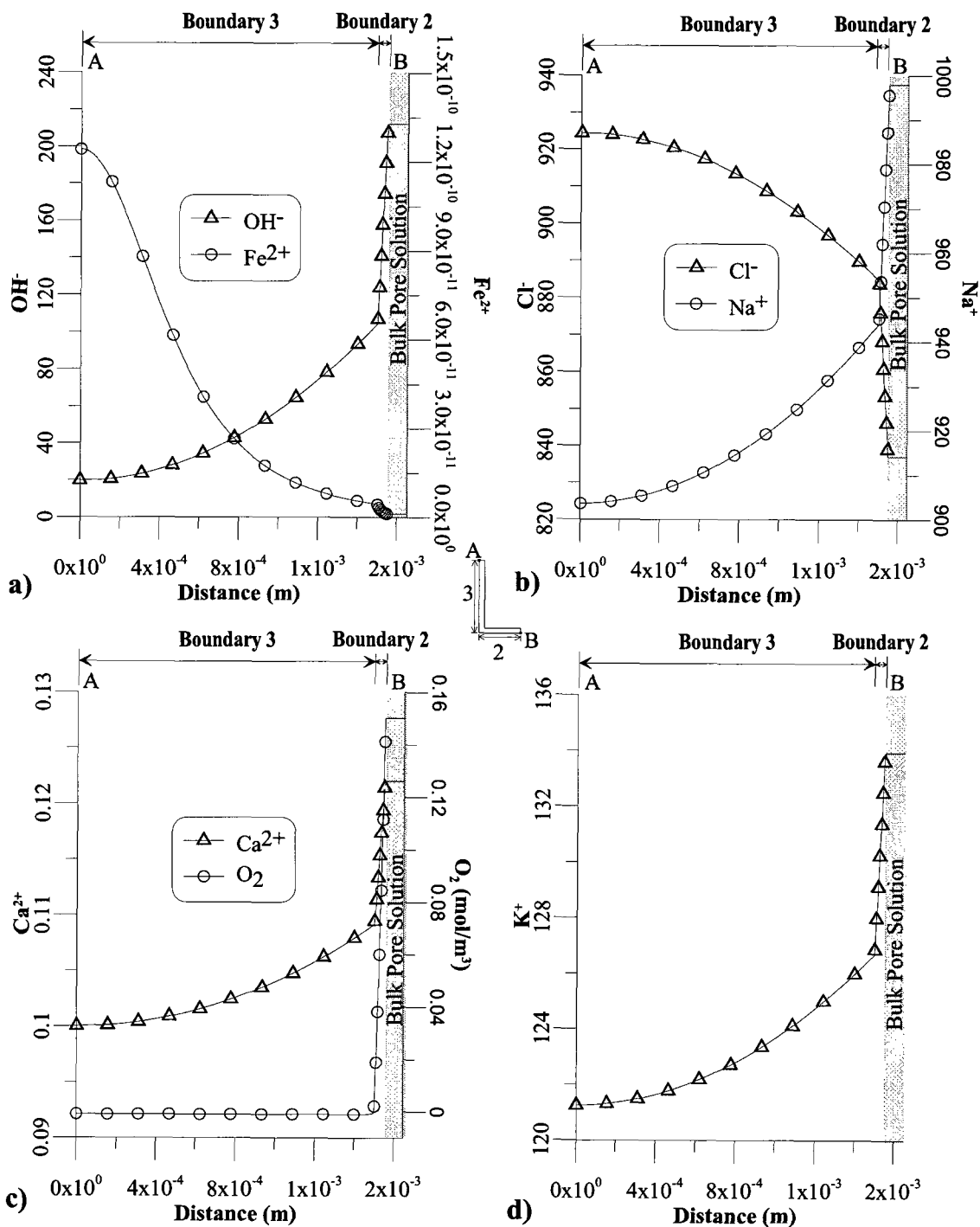


**Figure 3.2.** The activities of the ionic species and the concentration of the gaseous species along the center of the mill scale crack (boundary 2) and along the steel surface (boundary 3) when steady-state conditions are reached.

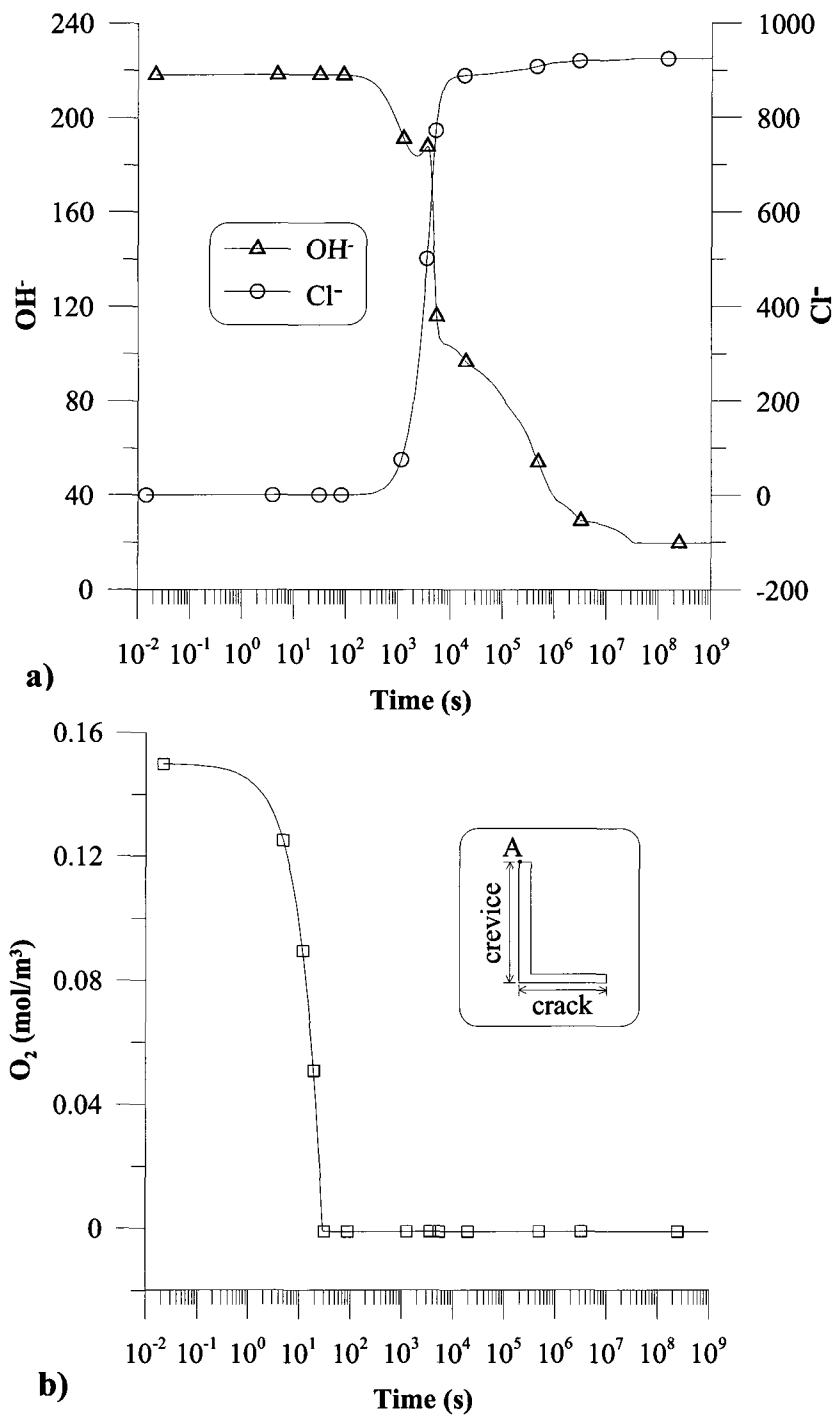


**Figure 3.3.** Time plots at the tip of the crevice (point A) for: (a) hydroxide activity, chloride activity and (b) oxygen concentration of species. For clarity, only some of the data points are shown in the plots.

As previously stated, due to the number of species analyzed, and since the main results of interest are those of  $\text{OH}^-$  and  $\text{Cl}^-$  ions, only the variation of pH and  $\text{Cl}^-/\text{OH}^-$  in the mill scale crack and crevice, as shown in Figure 3.4, will be reported in Chapter 4. The pH is calculated using the activity of the  $\text{OH}^-$  ions such that (Perez 2004):

$$pH = 14 + \log_{10} (c_{\text{OH}^-} \gamma_{\text{OH}^-} / \gamma_0) \quad (3.51)$$

where  $\gamma_0$  has a magnitude of 1 and the unit of the concentration,  $c_{\text{OH}^-}$ .

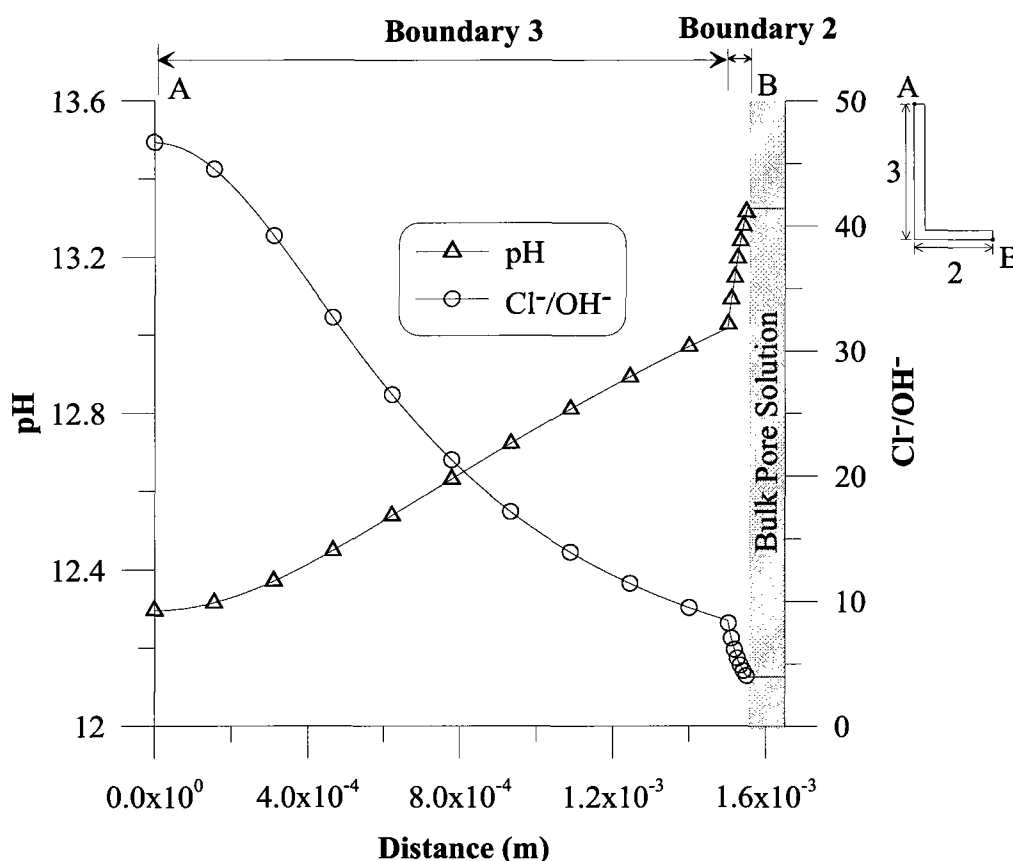


**Figure 3.4.** Variation of the pH and the  $\text{Cl}^-/\text{OH}^-$  ratio along the center of the mill scale crack (boundary 2) and along the steel surface (boundary 3) when steady-state conditions are reached. For clarity, only some of the data points are shown in the plots.

### 3.8 Effect of chemical activity on the simulations

A numerical study was carried out to determine the effect chemical activity has on the simulations, specifically on the pH and  $\text{Cl}^-/\text{OH}^-$  in the crevice. The inclusion of chemical

activity effects in equation (3.10) increases the complexity and nonlinearity of the simulations; thus, it is important to know how equation (3.10) influences the results in order to determine whether or not chemical activity can be ignored in the present study (Chapter 4).

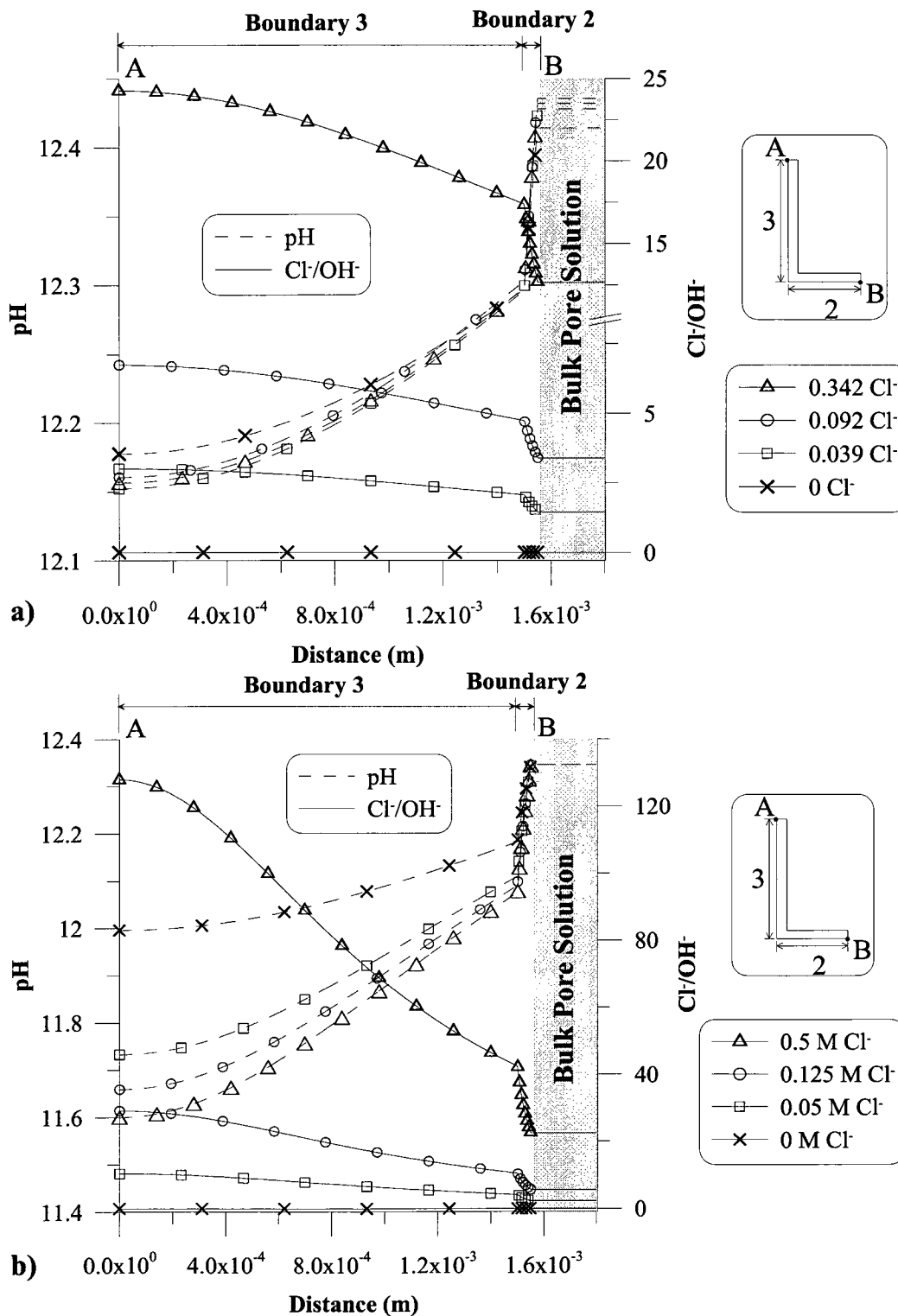
The analysis presented in this section was carried out in a domain with the following dimensions: mill scale crack length ( $l$ ) =  $5 \times 10^{-5}$  m; mill scale crack thickness ( $t_l/2$ ) =  $5 \times 10^{-8}$  m; crevice length ( $c/2$ ) =  $1.5 \times 10^{-3}$ ; crevice thickness ( $t_c$ ) =  $1 \times 10^{-6}$  m. A constant passive current density,  $i_p$ , of  $10^{-3}$  A/m<sup>2</sup> was applied on steel and mill scale surfaces. Diffusion coefficients of species were assumed to linearly decrease from  $D_{max}$  to  $D_{min}$ , as per Table 3.4. The simulations were carried out in CH solution; the chloride concentrations in the CH solution ranged from 0 to 500 mol/m<sup>3</sup>. Initial activities for the cases with chemical activity included in the CH solution (solutions no. 1, 2, 4 and 5) are given in Table 3.2, while the initial concentrations for the cases with chemical activity ignored (*i.e.*, chemical activity removed from equation (3.10)) in the CH solution (solutions no. 1, 2, 3 and 4) are given in Table 3.6.

**Table 3.6:** Bulk CH solution when chemical activity effects were ignored (mol/m<sup>3</sup>).

Solution n <sup>o</sup>	Cl <sup>-</sup>	OH <sup>-</sup> (*)	Fe <sup>2+</sup> (*)	Ca <sup>2+</sup> (*)	Na <sup>+</sup>
1	500	22.24	$9.85 \times 10^{-11}$	11.12	500
2	125	22.24	$9.85 \times 10^{-11}$	11.12	125
3	50	22.24	$9.85 \times 10^{-11}$	11.12	50
4	0	22.24	$9.85 \times 10^{-11}$	11.12	0

(\*) Concentrations calculated assuming  $\gamma_i$  is equal to 1 in equations (3.18), (3.19), (3.23)

In Figure 3.5, the pH and  $\text{Cl}^-/\text{OH}^-$  are plotted along boundaries 2 and 3 (from point B to point A as shown in the figure) after steady-state conditions were reached ( $t = 10^9$  s). Figure 3.5a presents the simulation results for cases with chemical activity included; Figure 3.5b presents the simulation results for the same cases when the chemical activity effects were ignored; *i.e.*, chemical activity removed from equation (3.10). When Figures 3.5a and 3.5b are compared, it can be observed that the inclusion of calculated chemical activity coefficients in the transport equations (*i.e.*, equation (3.10)) results in smaller drops in pH and smaller increases in  $\text{Cl}^-/\text{OH}^-$  within the crevice. This is mainly due to the decreased movement of the ionic species when ionic interactions were considered. For example, when ionic interactions are not considered, chlorides in the solution would not be held back by slower cations (e.g.  $D_{\text{Na}^+} = 1.33 \times 10^{-9}$  and  $D_{\text{Cl}^-} = 2.03 \times 10^{-9}$   $\text{m}^2/\text{s}$ ) and interactions with the water molecules (Samson et al. 1999b). For this reason, when the ionic interactions are not considered, the chlorides increase at greater magnitudes towards the tip of the crevice (point A), and this, in turn, also causes the hydroxides to decrease at larger amounts. Due to the significant effects activity has on the pH and  $\text{Cl}^-/\text{OH}^-$ , all simulations from here on will be carried out with chemical activity included.



## 4) Numerical Analysis and Discussion

Numerical simulations were carried out to investigate the chemistry of the concrete pore solution in the mill scale crevices of carbon steel rebar. Three scenarios were studied: (1) simulations in chloride-free pore solutions; (2) simulations in pore solutions with chlorides when the passive current density,  $i_p$ , is constant until depassivation; and (3) simulations in pore solutions with chlorides when the passive current density,  $i_p$ , increases after a predetermined chloride threshold is reached. In each scenario, a parametric study was carried out to investigate if the chemistry of the pore solution within mill scale crevices reaches conditions that may lead to pitting.

### 4.1 Simulations in chloride-free pore solution

The protective passive oxide film that forms on the rebar surface is considered to be stable within the alkaline environment provided by concrete, as long as chlorides are not present in the pore solution (Glass and Buenfeld 2000a). This implies that the pore solution chemistry in mill scale crevices would not reach critical pitting conditions because the stable passive film would protect the steel against corrosion. The numerical investigation presented in this section is intended to test this implication.

The simulations were carried out in the domain shown in Figure 3.1. The dimensions of the domain, which were selected to simulate a realistic case that would lead to large drops in pH (Ghods et al. 2009c), are provided in Table 4.1. Most simulations in this section

were carried out in the CH solution since its pH is lower than that of the CP solution; it was assumed that if the pH of the CH solution does not drop to critical levels, the pH of the CP solution would also remain above critical conditions. To support this assumption, one simulation in the CP solutions was also carried out (see Section 4.1.1.3); for this simulation, a large crevice length of  $1.5 \times 10^{-3}$  m was selected to obtain larger drops in pH.

**Table 4.1:** Dimensions of the domain for the simulations carried out in Section 4.1.

Relevant Sections	Crevice length, $c/2$ (m)	Mill scale crack length, $l$ (m)	Mill scale crack thickness, $t/2$ (m)	Crevice thickness, $t_c$ (m)
4.1.1.1 - 4.1.1.2	$3 \times 10^{-4}$	$5 \times 10^{-5}$	$5 \times 10^{-8}$	$1 \times 10^{-6}$
4.1.1.3	$1.5 \times 10^{-3}$			

The literature review in Section 2.2 showed that a passive current density of approximately  $10^{-3}$  A/m<sup>2</sup> is a reasonable estimate for carbon steel; however, it was also shown that there were experimental studies that reported current densities in a range between  $10^{-4}$  A/m<sup>2</sup> and  $10^{-2}$  A/m<sup>2</sup>. Therefore, the intensity of the passive current density was selected as one of the parameters of this parametric investigation. As discussed in Section 3.4.1, two cases were analyzed in this study: (1) passive current density defined on steel surfaces only; and (2) passive current density defined on steel and mill scale surfaces. Finally, the effect of decreasing diffusion coefficients of species with increasing Fe(OH)<sub>2(s)</sub> concentration was studied as part of the parametric investigation (see Section 3.5). All simulation cases are summarized in Table 4.2.

**Table 4.2:** Input parameters for all simulation cases in Section 4.1.

Relevant Section	Passive current density, $i_p$ (A/m <sup>2</sup> )	Treatment of passive current density	Diffusion coefficient, $D_{max}$ to $D_{min}$ (m <sup>2</sup> /s) (*)	Activity in bulk pore solution
4.1.1.1	10 <sup>-4</sup>	$i_p$ on steel & mill scale	10 <sup>-9</sup> to 10 <sup>-13</sup>	CH soln. 5 in Table 3.2
		$i_p$ on steel		
	10 <sup>-3</sup>	$i_p$ on steel & mill scale		
		$i_p$ on steel		
	10 <sup>-2</sup>	$i_p$ on steel & mill scale		
		$i_p$ on steel		
4.1.1.2	10 <sup>-2</sup>	$i_p$ on steel & mill scale	10 <sup>-9</sup> to 10 <sup>-13</sup>	CH soln. 5 in Table 3.2
			10 <sup>-9</sup> to 10 <sup>-11</sup>	
			10 <sup>-9</sup>	
4.1.1.3	10 <sup>-3</sup>	$i_p$ on steel & mill scale	10 <sup>-9</sup> to 10 <sup>-13</sup>	CH soln. 5 in Table 3.2
				CP soln. 6 in Table 3.3

(\*) Diffusion coefficient of each species change by orders of magnitude from  $D_{max}$  to  $D_{min}$  (see Table 3.4 for specific quantities of each species)

## 4.1.1 Results and discussion

### 4.1.1.1 Effect of passive current density

The effect of passive current density on the alkalinity of the CH solution within the mill scale crack and crevice is shown in Figure 4.1, in which the pH along the mill scale crack (boundary 2) and along the crevice (boundary 3) is plotted after steady-state conditions are reached ( $t = 10^9$  s).

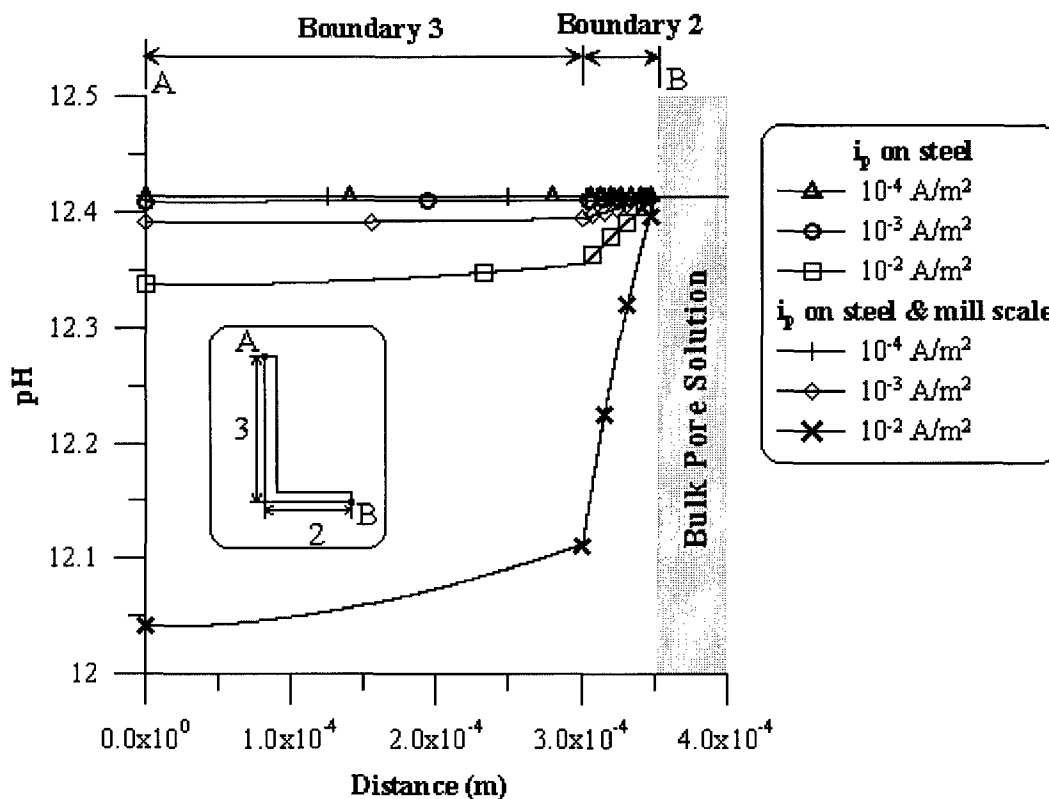


**Figure 4.1.** The pH profile along boundaries 2 and 3 (from point B to point A) for different passive current densities ( $i_p$ ) after steady-state conditions are reached at  $t = 10^9$  s. Diffusion coefficients linearly decrease from  $D_{max} = 10^{-9}$  to  $D_{min} = 10^{-13}$  A/m<sup>2</sup> as  $\text{Fe}(\text{OH})_{2(s)}$  builds up in the pore solution. For clarity, only some of the data points are shown in the plots.

In all cases shown in Figure 4.1, the pH decreases from the bulk solution (point B) to the tip of the crevice (point A). As discussed in Section 3.7, the consumption of oxygen by the cathodic reaction on the steel (and in some cases on the mill scale) surfaces reduces the amount of oxygen available in mill scale crevices, which in turn, decreases the amount of hydroxide production at these locations. It can also be seen that the largest drop in pH occurs within the mill scale crack length (*i.e.*, along boundary 2). This is mainly due to the small area of inflow caused by the narrow mill scale crack; a small amount of oxygen would diffuse into the system causing a sharp drop from that of the bulk pore solution levels (see oxygen profile in Figure 3.2c). The hydroxide production

due to the cathodic reactions has a similar trend because hydroxide production is correlated to the amount of oxygen available in the pore solution.

Figure 4.1 also shows that larger pH drops are caused by larger passive current densities because of the increased rates of iron oxidation and oxygen reduction reactions that are associated with the larger passive current densities. The largest pH drop (from 12.41 to 12.04 at point A) occurred when a passive current density of  $10^{-2} \text{ A/m}^2$  was applied on both steel and mill scale surfaces. However, even for this case, the alkalinity in the crevice is high enough (*i.e.*,  $\text{pH} > 10$ ) to resist a potential breakdown of the passive oxide film on the steel surface. This result indicates that without the presence of chlorides, carbon steel rebar will remain passive within the mill scale crevices. It is interesting to note that when a passive current density was only applied on the steel surface, the pH drop was not significant. For instance, the largest pH drop was from 12.41 to 12.34 at point A when a passive current density of  $10^{-2} \text{ A/m}^2$  was used.

Figure 4.2 shows the variation of pH at point A (*i.e.*, the tip of the crevice where the pH drop is the largest) over time in the CH solution. The cases presented in this figure are exactly the same ones in Figure 4.1; therefore the discussion on the effect of passive current density on the pH will not be repeated here. The examination of the pH over time in Figure 4.2 indicates that all cases have similar trends; however, only the cases with passive current densities of  $10^{-2} \text{ A/m}^2$  show large drops in pH. It can be seen in the pH profile that up until  $\sim 10^1 \text{ s}$ , there is no observable changes in pH since the hydroxide production (*i.e.*, cathodic reactions on steel surface) and consumption (*i.e.*, precipitation

of  $\text{Fe}(\text{OH})_{2(s)}$  are balanced. From  $\sim 10^1$  s to  $\sim 10^3$  s, the decrease in pH can be primarily attributed to the decrease in the hydroxide concentration due to the oxygen depletion within the crevice. During this period, the solid  $\text{Fe}(\text{OH})_{2(s)}$  concentration in the crack and crevice is relatively low; therefore the hydroxide within the crevice (or at point A in Figure 4.2) can be replenished from the bulk concrete pore solution relatively quickly because the diffusion coefficient is still large. As more iron from the steel surface dissolves into crevice, the solid  $\text{Fe}(\text{OH})_{2(s)}$  concentration increases, causing the diffusion of species, in particular of the hydroxide, from the bulk concrete pore solution towards the tip of the crevice to slow down. Therefore, a relatively large decrease in the pH is observed between  $\sim 10^3$  and  $\sim 10^7$  s. After  $\sim 10^7$  s, steady state conditions are reached; hence the pH remains relatively constant.

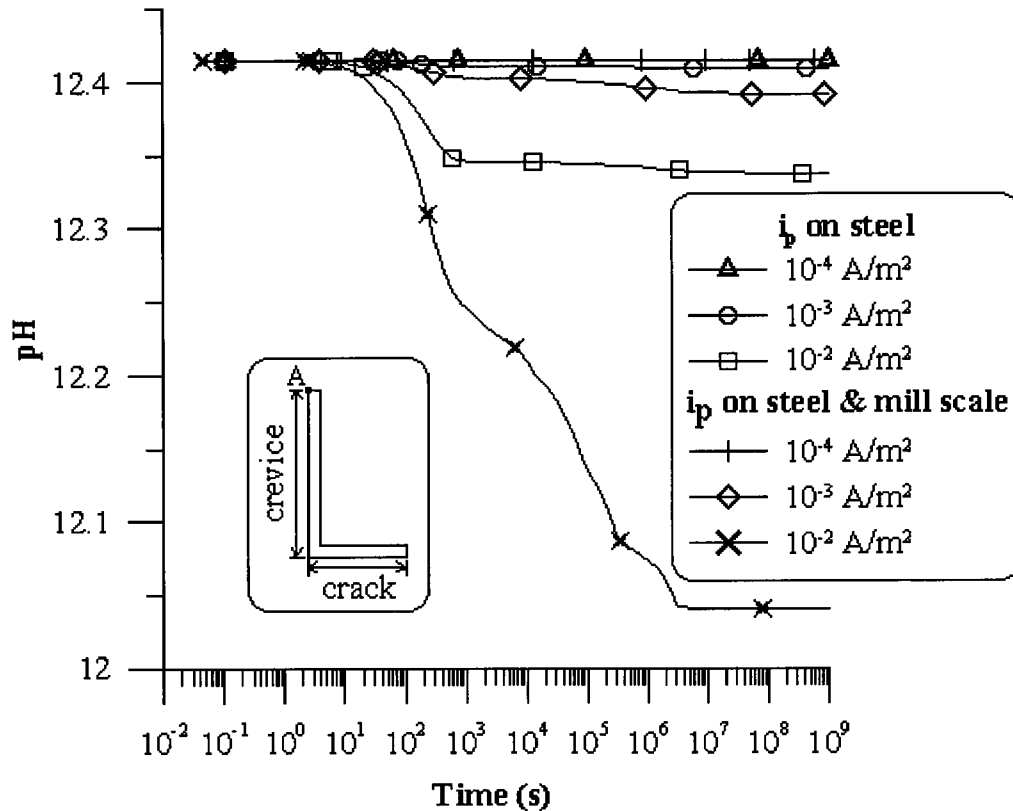


**Figure 4.2.** pH at point A over time with diffusion coefficients that linearly decrease from  $D_{max} = 10^{-9}$  to  $D_{min} = 10^{-13}$  A/m<sup>2</sup> as  $\text{Fe}(\text{OH})_{2(s)}$  builds up in the pore solution for various passive current densities ( $i_p$ ). For clarity, only some of the data points are shown in the plots.

#### 4.1.1.2 Effect of diffusion coefficient

To clearly observe the effect of decreasing diffusion coefficients on the pH of the pore solution within the crevice, a comparison of three different cases were examined when a passive current density of  $10^{-2}$  A/m<sup>2</sup> was applied on the steel and mill scale surfaces. In the first case, the diffusion coefficients of species were assumed to decrease linearly from  $10^{-9}$  m<sup>2</sup>/s to  $10^{-13}$  m<sup>2</sup>/s as the  $\text{Fe}(\text{OH})_{2(s)}$  concentration increases from 0 to 37,840 mol/m<sup>3</sup>. In the second case, for the same  $\text{Fe}(\text{OH})_{2(s)}$  buildup, the diffusion coefficients were assumed to decrease linearly from  $10^{-9}$  m<sup>2</sup>/s to  $10^{-11}$  m<sup>2</sup>/s. For the final case, the diffusion

coefficients were assumed to remain constant at  $10^{-9}$  m<sup>2</sup>/s, regardless of the Fe(OH)<sub>2(s)</sub> buildup. The results of the simulations are presented in Figures 4.3 – 4.5.

In Figure 4.3, the Fe(OH)<sub>2(s)</sub> concentrations at the tip of the crevice (point A) over time (Figure 4.3a), across the midpoint (C-C) of the crevice length at  $t = \sim 2.7 \times 10^4$  s (Figure 4.3b), and across the midpoint (D-D) of the mill scale crack length at  $t = \sim 1.4 \times 10^3$  s (Figure 4.3c) are presented (*i.e.*,  $\sim 2.7 \times 10^4$  and  $\sim 1.4 \times 10^3$  s represent the times at which a Fe(OH)<sub>2(s)</sub> concentration of 37,840 mol/m<sup>3</sup> is reached on each respective surface). It can be seen from these figures that changing diffusion coefficients of species in the pore solution does not have any remarkable influence on the Fe(OH)<sub>2(s)</sub> concentration within the mill scale crack and crevice. In addition, the profiles shown in Figures 4.3b and 4.3c indicates that the concentration of Fe(OH)<sub>2(s)</sub> is increasing quickly along the mill scale and steel surfaces, and slowly building up at the centre of the mill scale crack and crevice.

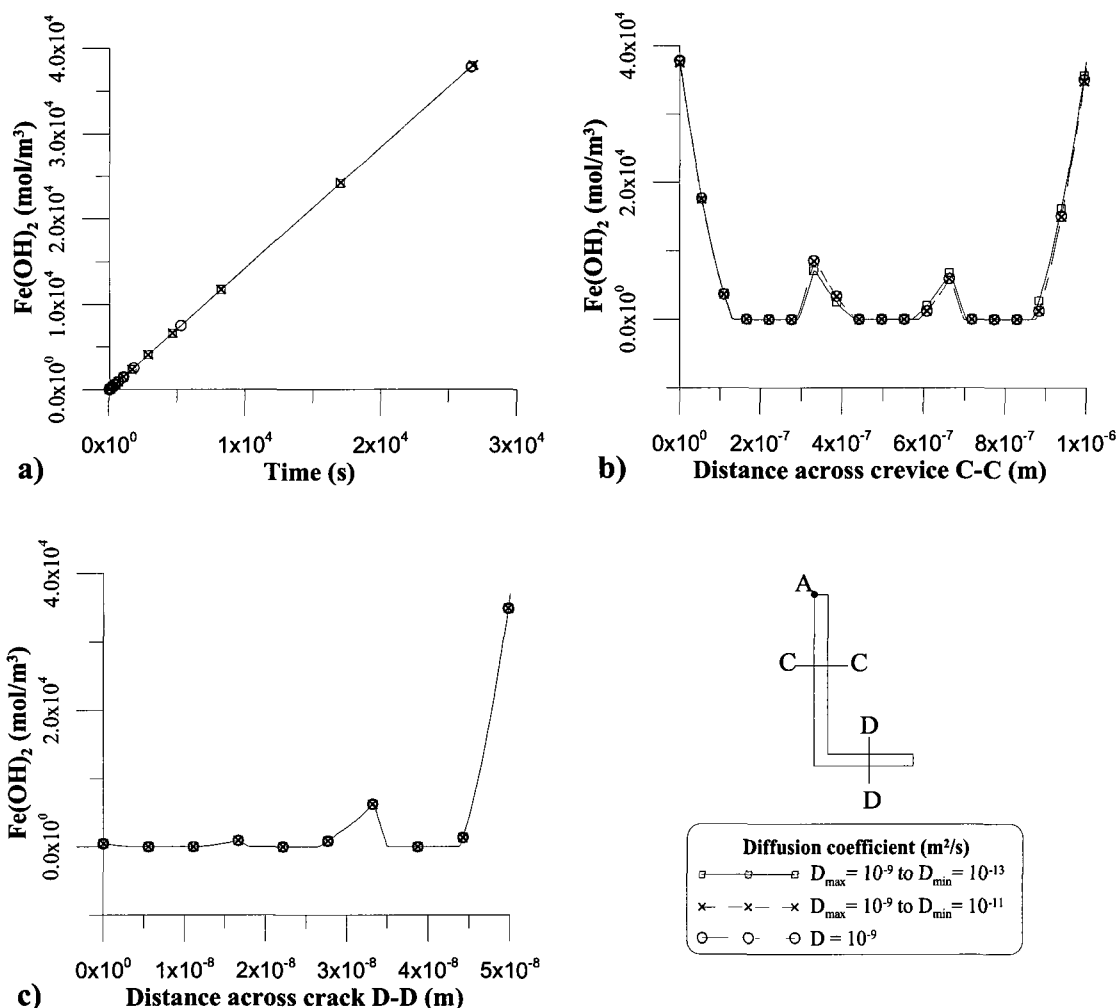
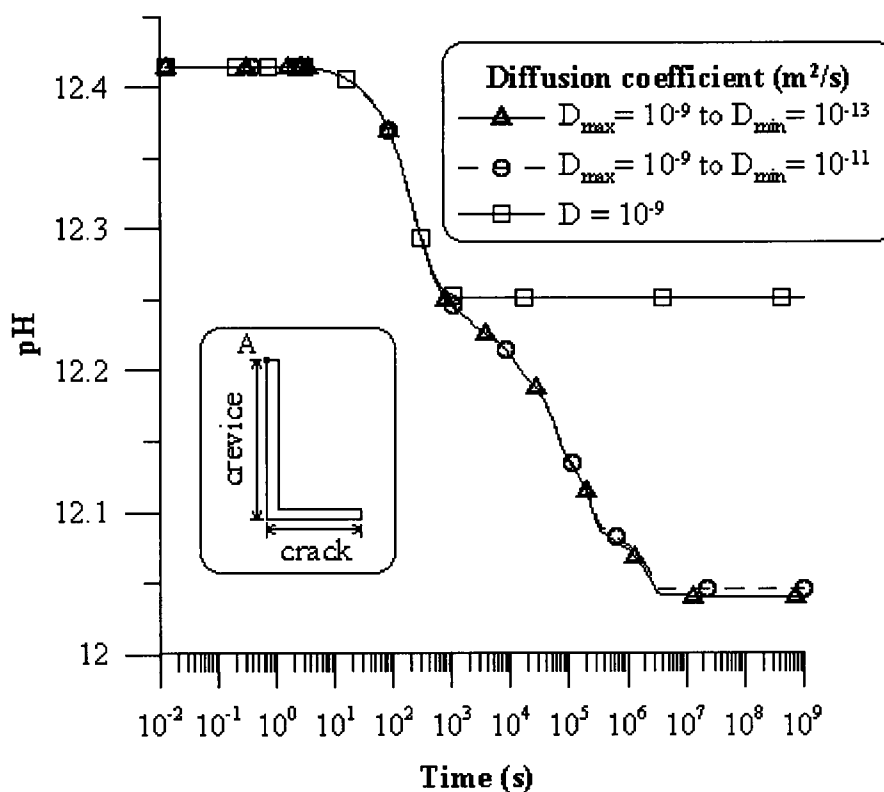


**Figure 4.3.**  $\text{Fe(OH)}_{2(s)}$  concentration for different diffusion coefficients that linearly decrease from  $D_{\max}$  to  $D_{\min}$  as solid build up in the pore solution: (a) at point A over time; (b) across the midpoint (C-C) of the crevice length at  $t = \sim 2.7 \times 10^4$  s; (c) across the midpoint (D-D) of the mill scale crack length at  $t = \sim 1.4 \times 10^3$  s. For clarity, only some of the data points are shown in the plots.

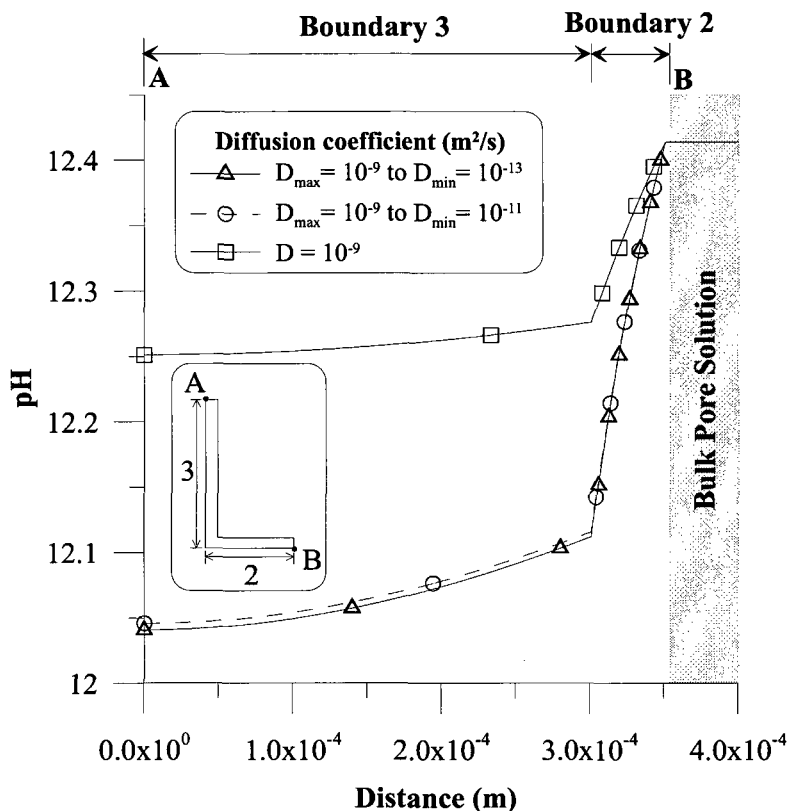
Figure 4.4 shows the pH over time at a point at the tip of the crevice (*i.e.*, point A).

Figure 4.5 shows the pH profile along the mill scale crack (boundary 2) and steel surface (boundary 3) after steady-state conditions are reached at  $t = 10^9$  s. Examination of Figures 4.4 and 4.5 indicates a significant difference in pH between the case, in which the diffusion coefficient remains constant at  $10^{-9} \text{ m}^2/\text{s}$ , and the other two cases, in which the

diffusion coefficient decreases to  $10^{-11}$  and  $10^{-13}$   $\text{m}^2/\text{s}$ . In fact, Figure 4.4 illustrates the time ( $t = \sim 10^3$  s) at which the diffusion coefficient becomes the dominant parameter causing the pH to decrease. It can also be observed in Figures 4.4 and 4.5 that there is negligible difference between the two cases in which the diffusion coefficients were decreased to  $10^{-11}$  and  $10^{-13}$   $\text{m}^2/\text{s}$ .



**Figure 4.4.** pH at point A over time for different diffusion coefficients that linearly decrease from  $D_{\text{max}}$  to  $D_{\text{min}}$  as  $\text{Fe}(\text{OH})_{2(\text{s})}$  builds up in the pore solution. For clarity, only some of the data points are shown in the plots.



**Figure 4.5.** pH profile along boundaries 2 and 3 (from point B to point A) after steady-state conditions are reached for different diffusion coefficients that linearly decrease from  $D_{max}$  to  $D_{min}$  as  $\text{Fe}(\text{OH})_{2(s)}$  builds up in the pore solution. For clarity, only some of the data points are shown in the plots.

#### 4.1.1.3 Analysis in the CP solution

Up to this point, the simulations that were carried out in the chloride-free CH solution have been presented. It was assumed that if the pH within the crevice did not drop to critical values (*i.e.*,  $\text{pH} < 10$ ), the pH of the CP solution would also remain above 10. To confirm this, an additional simulation was carried out in the CP solution, as shown in Figure 4.6 (see Tables 4.1 and 4.2 for the parameters of the simulation). As was the case for all other simulations for the CH solution, the pH of the CP solution also remained above 10; therefore the steel in the mill scale crevice was not susceptible to pitting. It was also confirmed that CP solution was more resistant to the pH drop due to its high

alkalinity that originates from the excess amounts of hydroxide ions provided by the highly soluble KOH and NaOH in the CP solution.

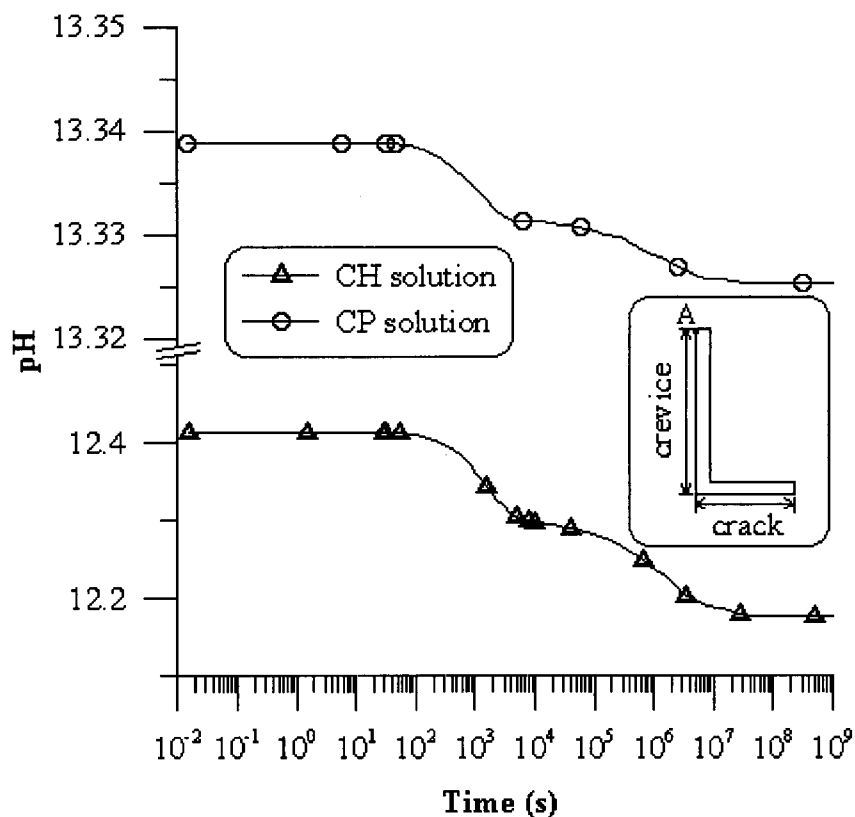


**Figure 4.6.** pH at point A over time with diffusion coefficients that linearly decrease from  $D_{max} = 10^{-9}$  to  $D_{min} = 10^{-13}$  A/m<sup>2</sup> as  $\text{Fe}(\text{OH})_{2(s)}$  builds up in the pore solution for the CH solution with pH  $\sim 12.5$  and CP solution with pH  $\sim 13.5$ . For clarity, only some of the data points are shown in the plots.

#### 4.1.1.4 Summary

The simulations presented in this section show that the chemistry of the pore solution within mill scale crevices investigated in this study does not change significantly enough to cause the loss of conditions that lead to formation and maintenance of a stable passive film on the steel surface; therefore, the carbon steel facing a mill scale crevice can be assumed to be protected by a stable passive film when chlorides are not present in the pore solution.

## **4.2 Simulations in pore solutions with chlorides – constant $i_p$**

It is known that chlorides in quantities larger than a threshold concentration have the potential to breakdown the protective passive oxide film on the rebar surface (Glass and Buenfeld 2000a). Although a number of studies have observed that the passive current density increases after a threshold  $Cl^-/OH^-$  is reached (these cases are studied in Section 4.3), as also presented in the literature review (Section 2.2), for some cases the current density on the steel surface have been reported to increase from passive rates to active corrosion rates relatively quickly once the breakdown occurs. Literature review also showed that chloride concentrations below the threshold levels have little or no effect on the passive current density. In the simulations presented in this section, following some of the observations in the literature, the passive current density was assumed to remain constant until the critical conditions that are necessary for the passive film breakdown are reached, and afterwards, it was assumed to quickly increase to active corrosion rates, as illustrated in Figure 4.7. In this study, these critical conditions were assumed to occur when pH drops below 10 (based on the Pourbaix diagram of iron), regardless of  $Cl^-/OH^-$ .

The main objective of the simulations in this section is to investigate the pore solution chemistry within mill scale cracks and crevices when the passive current density is assumed to remain constant until depassivation. Specifically, the following questions will be answered:

- (1) Does  $Cl^-/OH^-$  within the crevice increase beyond the typically-observed thresholds (e.g.  $Cl^-/OH^- = 3$  can be taken as a reasonable reference for a typical chloride threshold) under a constant passive current density?

- (2) If the  $\text{Cl}^-/\text{OH}^-$  within the crevice exceed the typically-observed thresholds, does the pH of the pore solution in the crevice drop below 10, creating the necessary conditions for the depassivation and subsequent pitting of the steel?

The effects of a number of parameters on the outcome of these two questions were investigated; these parameters include the dimensions of the mill scale crack and crevice, the passive current density, the activities of chloride in the bulk concrete pore solution, and the diffusion coefficients of the species. Table 4.3 summarizes the parameters of all simulation cases analyzed in this section and the order in which they are presented.

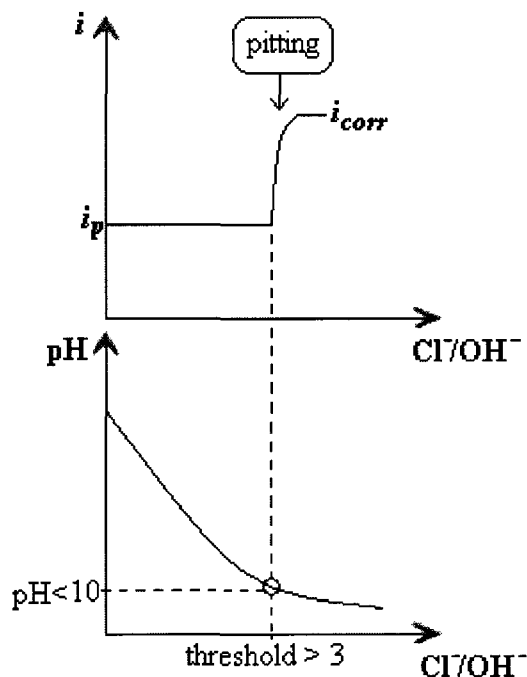


**Figure 4.7.** Assumed depassivation criterion for the simulations carried out in Section 4.2. It was assumed that the passive current density remains constant until pH drops below 10; afterwards, the current density is assumed to sharply increase to the active corrosion rate that is observed after pit formation. In the figure the threshold of 3 was chosen arbitrarily.

First, the effect of the mill scale crack thickness and crevice length on the chemistry of the pore solution in crevices is studied (see Section 4.2.1.1) based on the microscopic

observations of Ghods (2009) with the hope of identifying critical dimensions that may lead to breakdown of the passive film. Most simulations in this section were carried out using a passive current density of  $10^{-3}$  A/m<sup>2</sup>, which reasonably represents the passive current densities reported in the literature for carbon steel (see Section 2.2). However, as reported in the literature review, some studies have shown that an increase in the solution alkalinity also increases the passive current density on the steel surface. To include this observation in the analysis, while studying the effect of passive current density on the chemical composition of the CP solution in the mill scale cracks and crevices (see Section 4.2.1.2), a relatively large passive current density of  $10^{-2}$  A/m<sup>2</sup> was also used for one simulation.

In the investigation of the effect of chloride activities (see Section 4.2.1.3), different chloride activities in the bulk solution were chosen according to the alkalinity of the solution. Since CH solutions have hydroxide concentrations that are approximately ten times smaller than those in CP solutions (see Tables 3.2 and 3.3), larger chloride concentrations are required in the CP solution to reach the same Cl<sup>-</sup>/OH<sup>-</sup>. This implementation also supports the observations of Ghods et al. (2009d) (see Section 2.1 of the literature review), who reported that chloride thresholds in the CP solution were approximately ten times larger than those measured in the CH solution.

The effect of diffusion coefficient of the species on the chemical composition of the pore solution in the mill scale cracks and crevices as the concentration of Fe(OH)<sub>2(s)</sub> increases is reported in Section 4.2.1.4.

**Table 4.3:** Input parameters for all simulation cases carried out in Section 4.2.

Relevant Section	Passive current density, $i_p$ (A/m <sup>2</sup> )	Treatment of passive current density	Diffusion coefficient, $D_{max}$ to $D_{min}$ (m <sup>2</sup> /s) <sup>(a)</sup>	Activity in bulk pore solution <sup>(b)</sup>	Crevice length, $c/2$ (m)	Mill scale crack thickness, $t/2$ (m)
4.2.1.1	$1 \times 10^{-3}$	$i_p$ on steel & mill scale	$10^{-9}$ to $10^{-13}$	CH soln. 1 in Table 3.2	$1.5 \times 10^{-3}$	$5 \times 10^{-8}$
						$5 \times 10^{-7}$
						$5 \times 10^{-6}$
					$5 \times 10^{-8}$	$5.0 \times 10^{-5}$
						$5.0 \times 10^{-4}$
$1.5 \times 10^{-3}$						
4.2.1.2	$1 \times 10^{-4}$	$i_p$ on steel & mill scale	$10^{-9}$ to $10^{-13}$	CH soln. 1 in Table 3.2	$1.5 \times 10^{-3}$	$5 \times 10^{-8}$
	$5 \times 10^{-4}$					
	$1 \times 10^{-3}$	$i_p$ on steel		CP soln. 1 in Table 3.3		
	$1 \times 10^{-2}$	$i_p$ on steel & mill scale				
	$5 \times 10^{-3}$					
	$1 \times 10^{-3}$					
4.2.1.3	$1 \times 10^{-3}$	$i_p$ on steel & mill scale	$10^{-9}$ to $10^{-13}$	CH soln. 5 in Table 3.2	$1.5 \times 10^{-3}$	$5 \times 10^{-8}$
				CH soln. 4 in Table 3.2		
				CH soln. 2 in Table 3.2		
				CH soln. 1 in Table 3.2		
				CP soln. 6 in Table 3.3		
				CP soln. 5 in Table 3.3		
				CP soln. 4 in Table 3.3		
				CP soln. 1 in Table 3.3		
4.2.1.4	$1 \times 10^{-3}$	$i_p$ on steel & mill scale	$10^{-9}$ to $10^{-13}$	CH soln. 1 in Table 3.2	$1.5 \times 10^{-3}$	$5 \times 10^{-8}$
			$10^{-9}$ to $10^{-11}$			
			$10^{-9}$			

<sup>(a)</sup> Diffusion coefficient of each species change by orders of magnitude from  $D_{max}$  to  $D_{min}$  (see Table 3.4 for specific quantities of each species)

<sup>(b)</sup> Activities linearly change from CH soln. 5 in Table 3.2 and from CP soln. 6 in Table 3.3 ( $[Cl^-] = 0$ ) to its desired solution indicated in the Table 4.3 over a 3600 s period, as discussed in Section 3.4.1

## 4.2.1 Results and discussion

### 4.2.1.1 Effect of the mill scale crack thickness and crevice length

In the microscopic studies conducted by Ghods et al. (2009c), the dimensions of the mill scale cracks and crevices on carbon rebar surface show a large degree of variability. They show that rebars from different producers may have completely different mill scale structure and that even for the same rebar, the dimensions of mill scale cracks and crevices may be quite different from one location to the other. Ghods et al. (2009c) reported that the crack thickness ( $t_l/2$ ) and the crevice length ( $c/2$ ) show more variability than the crack length ( $l$ ) and crevice thickness ( $t_c$ ) (refer to Figure 3.1 for definitions); therefore, in this study, the effect of the former two parameters on the pore solution chemistry in the mill scale cracks and crevices were investigated. Based on the observations of Ghods et al. (2009c), the mill scale crack length ( $l$ ) and crevice thickness ( $t_c$ ) were assumed to be constant as  $5 \times 10^{-5}$  m and  $1 \times 10^{-6}$  m, respectively. The crack thickness ( $t_l/2$ ) and the crevice length ( $c/2$ ) for each simulation are presented in Table 4.3. The analyses were carried out for the CH solution.

To study the effects of crack thickness ( $t_l/2$ ), the pH and  $Cl^-/OH^-$  were analyzed along boundaries 2 and 3 (from point B to point A) after steady-state conditions are reached ( $t = \sim 10^9$  s), as shown in Figure 4.8. Examination of Figure 4.8 shows that a smaller crack thickness results in a larger decrease in pH and a larger increase in  $Cl^-/OH^-$  towards the tip of the crevice (point A). Although a decrease in pH is observed with decreasing crack thickness, the changes from the bulk pore solution are not significant, as the largest pH drop is shown to be from 12.43 in the bulk pore solution to 12.16 at point A for a crack

thickness of  $5 \times 10^{-8}$  m.  $\text{Cl}^-/\text{OH}^-$  show an increase towards the tip of the crevice as the crack thickness becomes smaller; for example,  $\text{Cl}^-/\text{OH}^-$  increases (almost doubles) from 12.64 in the bulk pore solution to 24.26 at point A for a crack thickness of  $5 \times 10^{-8}$  m.

It is interesting to note that the effect of decreasing crack thickness on pH and  $\text{Cl}^-/\text{OH}^-$  was more significant as the crack thickness was decreased from  $5 \times 10^{-7}$  m to  $5 \times 10^{-8}$  m, when compared with the changes observed as the crack thickness was decreased from  $5 \times 10^{-6}$  m to  $5 \times 10^{-7}$  m. For the smallest crack thickness (*i.e.*,  $5 \times 10^{-8}$  m), the changes in pH and  $\text{Cl}^-/\text{OH}^-$  are quite visible within the crack length, while changes in pH and  $\text{Cl}^-/\text{OH}^-$  are less pronounced within the crack length for the other two larger crack thicknesses.

The differences in simulations with different crack thicknesses can be explained by the fact that the rate of supply of oxygen decreases in narrow cracks; hence smaller amounts of oxygen would reach the crevice area to compensate for the reduction of oxygen due to the cathodic reactions, and this, in turn, would reduce the hydroxide production by the cathodic reactions in the crevice (along boundary 3). For a detailed explanation of the mechanism of decrease in pH and increase in  $\text{Cl}^-/\text{OH}^-$ , refer to Section 3.7. The same mechanism can also be used to explain why the changes along the mill scale crack (boundary 2) are larger than those along the steel surface (boundary 3) for the smallest crack thickness analyzed (*i.e.*,  $5 \times 10^{-8}$  m): less oxygen diffuses into the system from the bulk pore solution due to the narrower mill scale crack, causing oxygen to be consumed quickly by the cathodic reactions on the mill scale surfaces, as indicated in the oxygen profile in Figure 3.2c; since the production of hydroxides was dependent on the

consumption of oxygen, similar changes within the mill scale crack would also be observed for hydroxides. For the larger crack thicknesses of  $5.0 \times 10^{-7}$  and  $5.0 \times 10^{-6}$  m, more oxygen diffuse into the system from the bulk pore solution allowing a larger area of the mill scale crack and crevice to compensate for the reduction of oxygen, which leads to a more steady decline in the oxygen concentration within the mill scale crack.

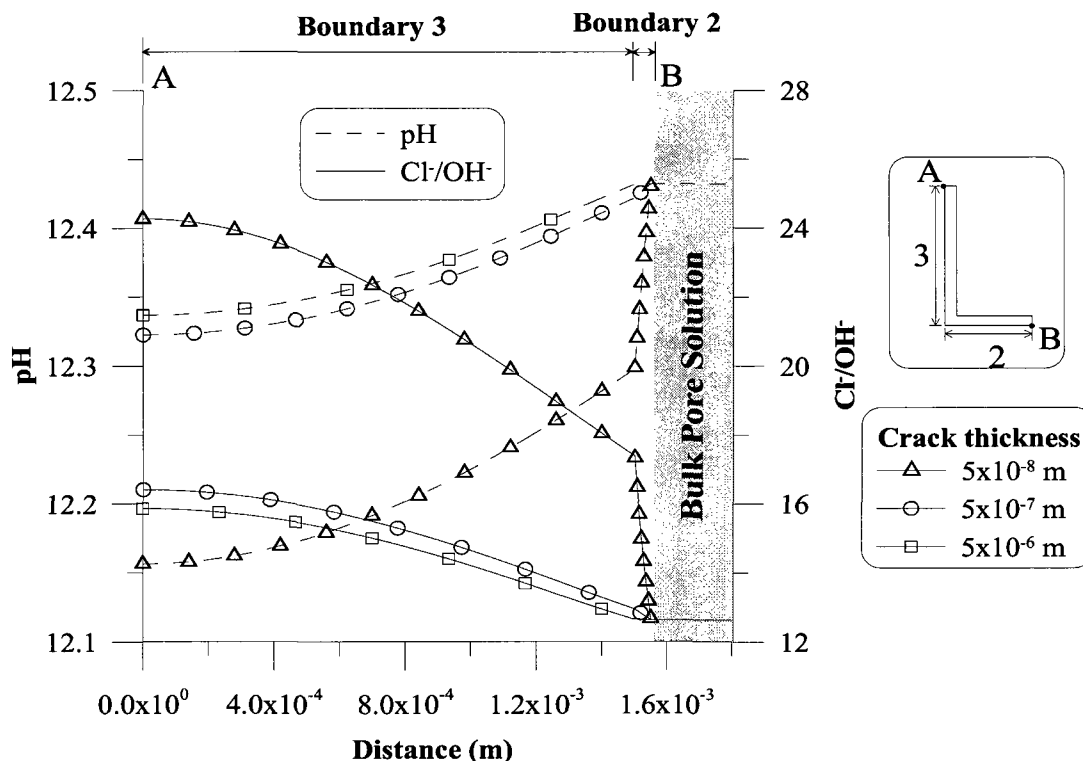


**Figure 4.8.** pH and  $\text{Cl}^-/\text{OH}^-$  for a varying crack thickness along boundaries 2 and 3 (from point B to point A) after steady-state conditions are reached. For clarity, only some of the data points are shown in the plots.

To study the effect of crevice length ( $c/2$ ), pH and  $\text{Cl}^-/\text{OH}^-$  were analyzed along boundaries 2 and 3 (from point B to point A) after steady-state conditions were reached ( $t = \sim 10^9$  s), as shown in Figure 4.9. In this figure, only the results for a crevice length of  $1.5 \times 10^{-3}$  m is presented, since the other two shorter crevice lengths (*i.e.*,  $5 \times 10^{-5}$  and  $5 \times 10^{-4}$  m) showed negligible pH drops. For example, at a crack length ( $c/2$ ) of  $5.0 \times 10^{-4}$  m, the pH decreases from 12.43 at its bulk pore solution to 12.38 at point A; and at a crevice

length of  $5.0 \times 10^{-5}$  m, there is no difference in the pH along the mill scale crack and crevice up to four significant figures. The pH drop at a crevice length of  $1.5 \times 10^{-3}$  m is not significant (pH ranges from 12.43 to 12.16) to cause depassivation, but it is nevertheless larger than the other cases investigated. The same observations can also be made for  $\text{Cl}^-/\text{OH}^-$ , which increases at a large amount from its bulk pore solution of 12.64 to 24.26 at the tip of the crevice (point A) for a crevice length of  $1.5 \times 10^{-3}$  m, while the increase in  $\text{Cl}^-/\text{OH}^-$  is small (11.83 % and 0.55 %) for other crack lengths.

These results indicate that the outcome of an increasing crevice length is a decrease in pH and an increase in  $\text{Cl}^-/\text{OH}^-$ . A longer crevice length will result in a larger steel surface, on which oxygen is consumed and eliminated from the crevice, starting from the tip of the crevice (point A) towards the opening of the crevice. As a result, there will be reduced amounts of hydroxides towards the tip of the crevice (hence lower pH), which leads to an increase in the amount of chlorides needed to maintain electro-neutrality (hence higher  $\text{Cl}^-/\text{OH}^-$ ). In addition, the increased steel surface area also causes larger amounts of iron to dissolve into the pore solution within the crevice, which react with hydroxides to form the  $\text{Fe}(\text{OH})_{2(s)}$ , thus further decreasing the hydroxide concentration inside the crevice.

In summary, the dimensions of the mill scale crack and crevice, which is illustrated in Figure 3.1, showed that the smaller crack thicknesses and longer crevice lengths provided less favourable conditions for sustaining a stable passive film on steel surfaces within mill scale crevices. Having written this, in the cases analyzed, the decrease in pH was

not large enough to establish the assumed conditions for the breakdown of the passive film.

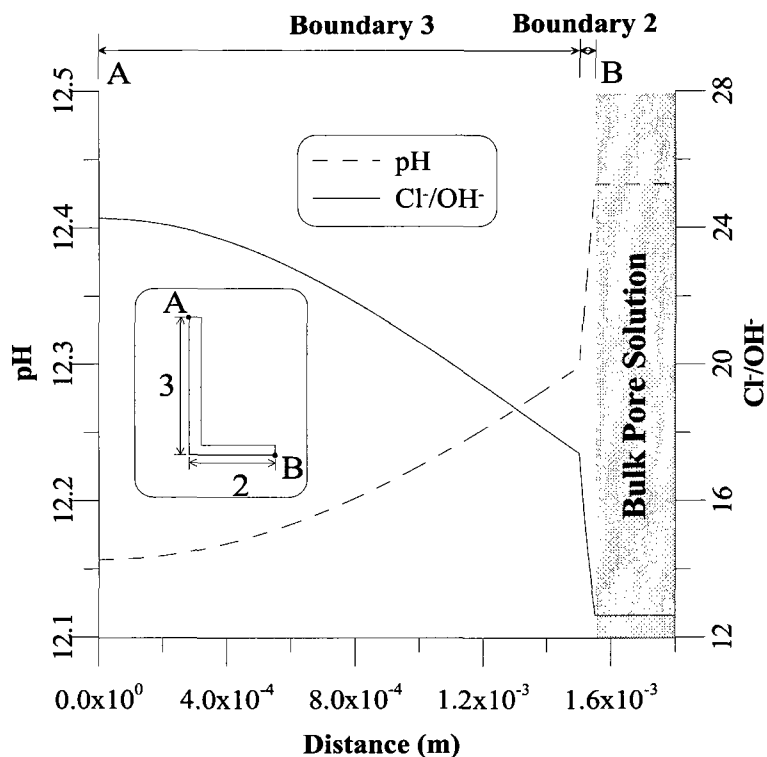


**Figure 4.9.** pH and  $\text{Cl}^-/\text{OH}^-$  for crevice length ( $c/2$ ) of  $1.5 \times 10^{-3}$  m along boundaries 2 and 3 (from point B to point A) after steady-state conditions are reached. Other two crevice lengths (*i.e.*,  $5 \times 10^{-5}$  and  $5 \times 10^{-4}$  m) are not shown because of negligible changes in pH.

#### 4.2.1.2 Effect of passive current density

The effect of passive current density on the chemical composition of the mill scale cracks and crevices is reported in this section using a domain with realistic dimensions that provided the most favourable conditions for the breakdown of the passive film in Section 4.2.1.1 (*i.e.*,  $5 \times 10^{-5}$  m for the mill scale crack length ( $l$ ),  $5 \times 10^{-8}$  m for the mill scale crack thickness ( $t/2$ ),  $1.5 \times 10^{-3}$  m for the crevice length ( $c/2$ ), and  $1 \times 10^{-6}$  m for the crevice thickness ( $t_c$ )). Other input parameters for the simulations carried out in this section are presented in Table 4.3. Three effects were investigated: (1) the effect of varying passive

current densities (on steel and mill scale surfaces) in CH solutions; (2) the effect of varying passive current densities (on steel and mill scale surfaces) in CP solutions; and (3) the effect of applying the passive current density on steel surfaces only. Indicated in Section 2.2 of the literature review is the observation that passive current density increases with an increase in the alkalinity of the solution; therefore, CH solutions were analyzed at passive current densities ranging between  $10^{-4}$  to  $10^{-3}$  A/m<sup>2</sup>, while passive current densities in the CP solutions ranged between  $10^{-3}$  to  $10^{-2}$  A/m<sup>2</sup>. The case which provided the largest drop in pH and the largest increase in Cl<sup>-</sup>/OH<sup>-</sup> was used in a simulation for which the passive current density was defined only on steel surfaces. As previously mentioned in Section 3.4.1, the literature on the subject of whether or not mill scale surfaces are conductive is not conclusive.

For CH solutions, pH and Cl<sup>-</sup>/OH<sup>-</sup> were analyzed at different passive current densities along the mill scale crack (boundary 2) and crevice (boundary 3) after steady-state conditions were reached ( $t = \sim 10^9$  s), as shown in Figure 4.10. The results presented in Figure 4.10 indicate that larger passive current densities result in larger decreases in the pH and larger increases in Cl<sup>-</sup>/OH<sup>-</sup> towards the tip of the crevice (point A). The changes in pH from the bulk pore solution to the tip of the crevice were not significant as the pH only decreases from 12.43 to 12.16 when a passive current density of  $10^{-3}$  A/m<sup>2</sup> was applied. On the other hand, Cl<sup>-</sup>/OH<sup>-</sup> increase at a range of 12.64 to 24.26 for the passive current density of  $10^{-3}$  A/m<sup>2</sup>. As smaller passive current densities were applied, the changes in for pH and Cl<sup>-</sup>/OH<sup>-</sup> were smaller.

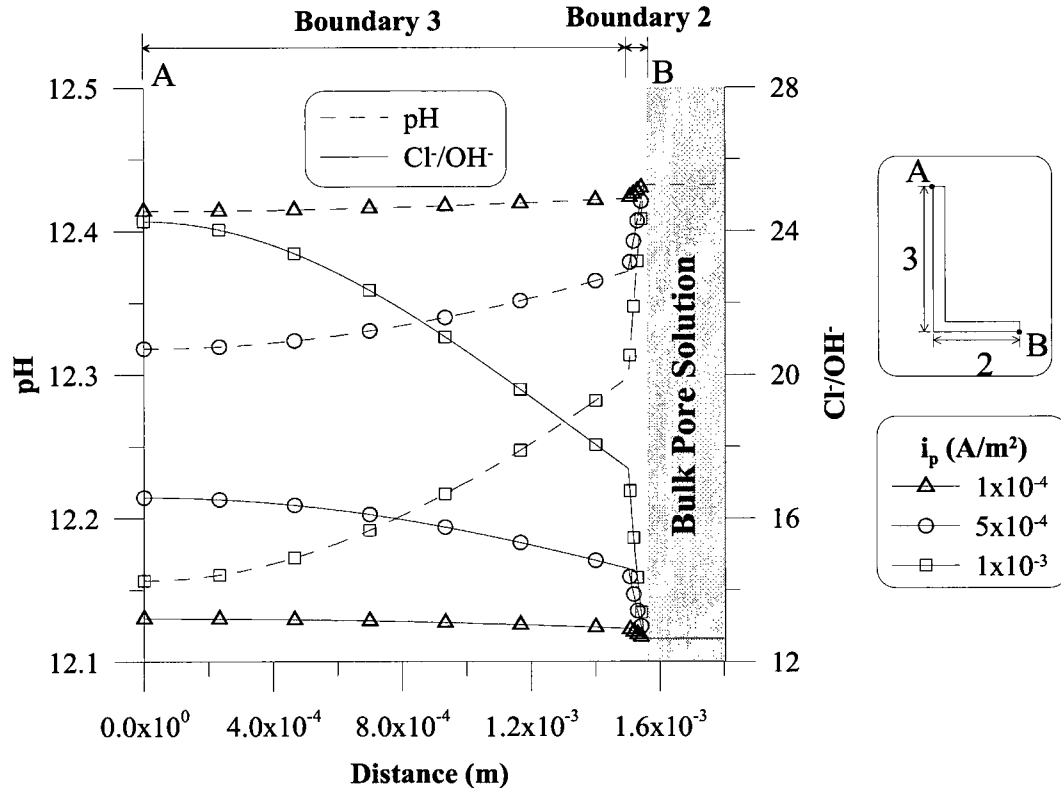


**Figure 4.10.** pH and  $\text{Cl}^-/\text{OH}^-$  at various passive current densities,  $i_p$ , in CH solutions with conductive mill scale surfaces along boundaries 2 and 3 (from point B to point A) after steady-state conditions are reached. For clarity, only some of the data points are shown in the plots.

For CP solutions, the pH and  $\text{Cl}^-/\text{OH}^-$  were analyzed at larger passive current densities ranging from  $10^{-3}$  to  $10^{-2}$   $\text{A}/\text{m}^2$  along the mill scale crack and crevice after steady-state conditions were reached ( $t = \sim 10^9$  s). These results, which are presented in Figure 4.11, provide similar trends as observed in the CH solution, shown in Figure 4.10, but to a smaller degree. For example, in the CP solution for a relatively large passive current density of  $10^{-2}$   $\text{A}/\text{m}^2$ , pH only changes from 13.33 in the bulk pore solution (point B) to 12.95 at the tip of the crevice (point A), and  $\text{Cl}^-/\text{OH}^-$  increases from 3.94 to 9.95 from point B to A.

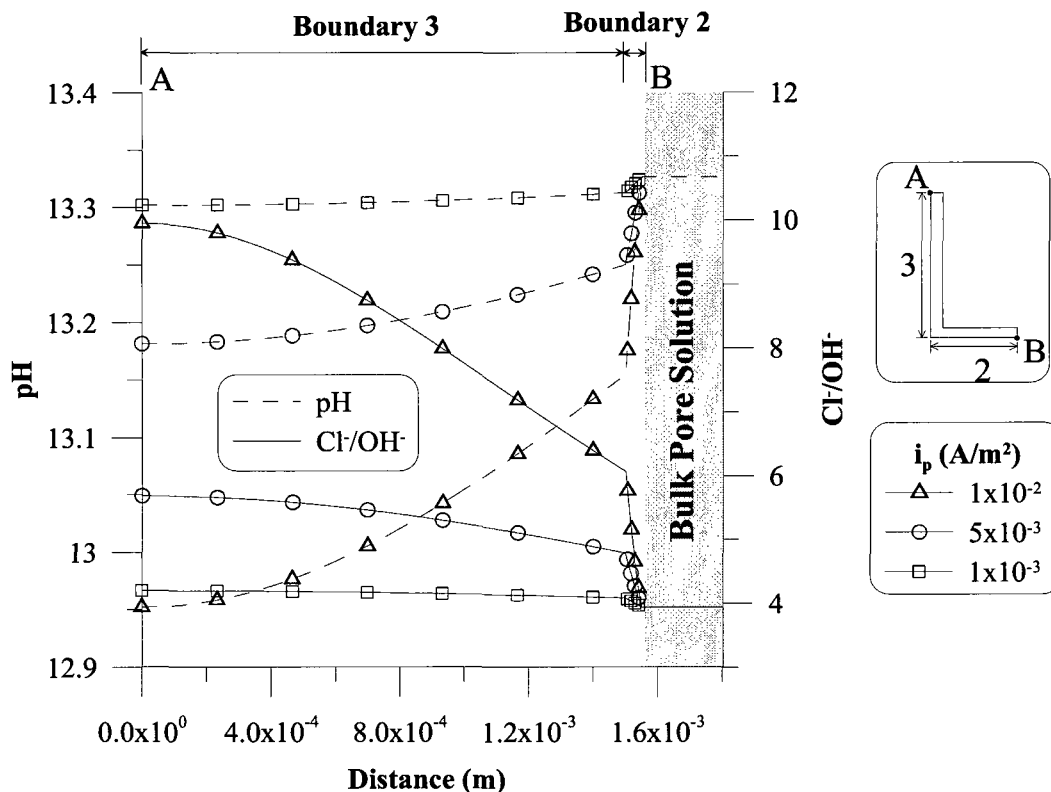


**Figure 4.11.** pH and Cl<sup>-</sup>/OH<sup>-</sup> at various passive current densities,  $i_p$ , in CP solutions with conductive mill scale surfaces along boundaries 2 and 3 (from point B to point A) after steady-state conditions are reached. For clarity, only some of the data points are shown in the plots.

The differences in simulations with different passive current densities in both solutions can be explained by the fact that larger passive current densities would increase the rate of iron dissolution and reduction reactions at the steel surface; thus, more iron ions would be present in the crevice to react with hydroxides to form  $\text{Fe}(\text{OH})_{2(s)}$ ; and the oxygen molecules would be consumed at a faster rate on the steel surface, which reduce the amount of oxygen present in the crevice area for the production of hydroxides. This, in turn, causes the pH to drop and Cl<sup>-</sup>/OH<sup>-</sup> to increase in the crevice, as described in detail in Section 3.7. When comparing the results of the CH solution with the CP solution at a constant passive current density of  $10^{-3}$  A/m<sup>2</sup>, it becomes clear how much more protective CP solutions are against the depassivation process; in the CH solution a 2.24 % drop in

pH and a 63.0 % increase in  $\text{Cl}^-/\text{OH}^-$  were observed; while in the CP solution, a 0.19 % drop in pH and a 6.31 % increase in  $\text{Cl}^-/\text{OH}^-$  were observed. This result can be explained by the fact that CP solutions have a larger ionic strength than that of the CH solution (see Tables 3.2 and 3.3) due to the additional hydroxides provided by KOH and NaOH compounds. As was mentioned in Section 3.3 and 3.8, larger ionic strengths result in an increased amount of ionic interactions (represented by effects of chemical activity), which reduce the mobility of ions in the solution. It should also be mentioned that similar hydroxide changes for CH and CP solutions would result in larger pH drops for the CH solution due to the fact that pH is a logarithmic function.

The final investigation carried out in this section involves the case presented in Figure 4.10, in which a passive current density of  $10^{-3} \text{ A/m}^2$  was applied on the steel and mill scale surfaces that provided the largest drop in pH and the largest increase in  $\text{Cl}^-/\text{OH}^-$  in the CH pore solution within the crevice. Using the same parameters, and only changing the treatment of the passive current density such that it was only applied on the steel surface, a comparison between the two cases was made. It can be observed in Figure 4.12 that the trends of both cases are similar, as both of them show pH decreasing and the  $\text{Cl}^-/\text{OH}^-$  increasing towards the tip of the crevice (point A); however, the results showed a nearly negligible pH drop and relatively small increase in  $\text{Cl}^-/\text{OH}^-$  when a passive current density was only applied on the steel surface; for example, pH only decreases by 0.65 % and  $\text{Cl}^-/\text{OH}^-$  increases by 19.07 % from point B to A when the passive current density was only applied on steel surfaces; whereas the respective changes when the passive current density was applied on both steel and mill scale surfaces were 2.24 % and 63.0 %.

The main difference between the two cases is in the surface area on which cathodic and anodic reactions can take place. In the later, the oxygen consumption and iron dissolution within the mill scale were significantly larger due to the larger surface on which cathodic reactions (oxygen consumption), and anodic reactions (iron dissolution), could take place.

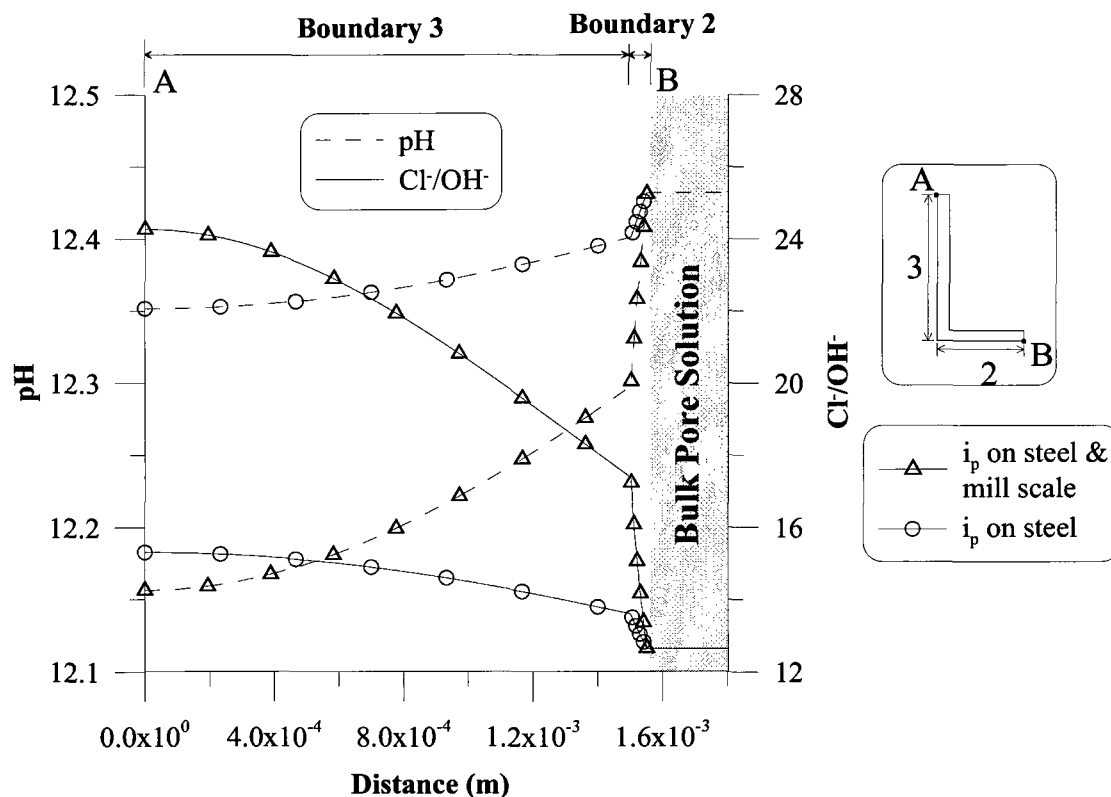


**Figure 4.12.** pH and  $\text{Cl}^-/\text{OH}^-$  for conductive and non-conductive mill scale surfaces along boundaries 2 and 3 (from point B to point A) after steady-state conditions are reached. For clarity, only some of the data points are shown in the plots.

In summary, the passive current density was shown to have an important effect on the chemistry of the pore solution with mill scale cracks and crevices; however, none of the cases studied reached conditions which would bring the pH below 10 in order to cause a breakdown of the passive film. Varying the passive current densities was shown to have a larger effect in the CH solutions than CP solutions, which have higher alkalinity. Since

the application of passive current density on both steel and mill scale surfaces causes larger drops in pH and larger increases in  $\text{Cl}^-/\text{OH}^-$ , despite the fact that there is no conclusive evidence in the literature that mill scale is conductive, simulations from now on will be carried out with passive current densities applied both on steel and mill scale surfaces.

#### *4.2.1.3 Effect of chloride in the bulk concrete pore solution*

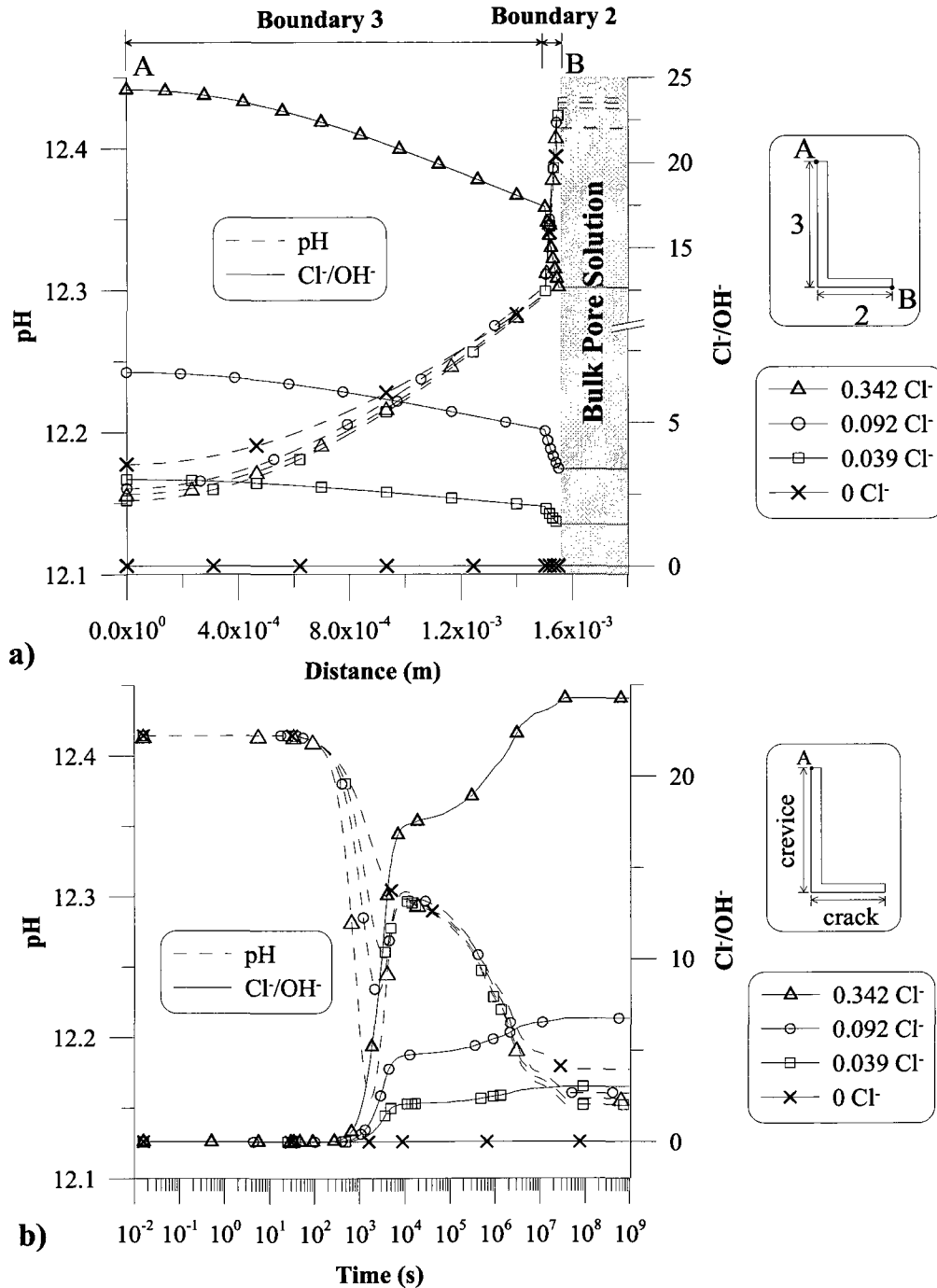
In this section, the effects of chlorides on the chemistry of the pore solution within mill scale cracks and crevices are studied for both CH and CP solutions. Although it was determined in the previous section that larger passive current densities increase the susceptibility for the breakdown of the passive film, for consistency, a constant passive current density of  $10^{-3} \text{ A/m}^2$  was used in all simulations in this section when comparing the CH and CP solutions. All other input parameters for the simulations carried out in this section are presented in Table 4.3. Due to the fact that the pH of CP solutions was approximately 1 unit larger than that of CH solutions (see Tables 3.2 and 3.3),  $\sim 10$  times the chloride concentrations were required in CP solutions to reach the same  $\text{Cl}^-/\text{OH}^-$ . In addition, it was indicated in Section 2.1 that larger chloride concentration thresholds were observed in CP solutions than that in CH solutions; thus, in this study, chloride activities were chosen in the range from 0 to 0.342 (corresponding to a  $[\text{Cl}^-]$  of 0 to 0.5 M) for CH solutions and from 0 to 0.837 (corresponding to a  $[\text{Cl}^-]$  of 0 to 1.25 M) for CP solutions.

Figure 4.13a presents the variation of pH and  $\text{Cl}^-/\text{OH}^-$  along boundaries 2 and 3 (from point B to point A) for different chloride activities in the bulk CH solution, after steady-

state conditions were reached ( $t = \sim 10^9$  s). The results presented in Figure 4.13a indicate that the addition of chloride in the bulk CH solution causes the pH to decrease and  $\text{Cl}^-/\text{OH}^-$  to increase from the bulk solution towards the tip of the crevice (point A). It is important to note that the decrease in pH is relatively small, almost negligible as compared to the drops required to observe depassivation (*i.e.*, largest pH drop ranges from 12.43 to 12.15) for all chloride activities (*i.e.*, 0.342, 0.092 and 0.039), and the pH plots for different chloride activities in the bulk CH solution are nearly on top of each other. On the other hand, the increase in  $\text{Cl}^-/\text{OH}^-$  from the bulk solution towards the tip of the crevice (point A) is relatively large; for example, when chloride activity in the bulk CH solution is 0.342,  $\text{Cl}^-/\text{OH}^-$  at the tip of the crevice (point A) increases to 24.26 while  $\text{Cl}^-/\text{OH}^-$  in the bulk solution is 12.64.

It should also be noted that, unlike its effect on pH, the activity of chlorides in the bulk solution makes a relatively large difference in the increase in  $\text{Cl}^-/\text{OH}^-$  within the mill scale crack and crevice. For example, the largest difference at the tip of the crevice (point A) among the four chloride cases occurred between the chloride activities of 0 and 0.039, in which a 0.21 % difference was observed; whereas, the differences in  $\text{Cl}^-/\text{OH}^-$  at the tip of the crevice (point A) became larger as the chloride activity increased: 76.5 % increase from 0.039  $\text{Cl}^-$  to 0.092  $\text{Cl}^-$ , and 113.1 % increase from 0.092  $\text{Cl}^-$  to 0.342  $\text{Cl}^-$ . An increase in the activity of chlorides at the bulk solution did not significantly affect the pH because the chemical activity effects (*i.e.*, ionic interactions) caused the hydroxide to remain relatively consistent as more chlorides were added to the system; this effect is shown more clearly in Table 3.2. Because the activity of hydroxides remained at a

relatively constant value as the chloride activity increased within the bulk solution, the  $Cl^-/OH^-$  would accordingly show increasing values.



**Figure 4.13.** pH and  $Cl^-/OH^-$  at different chloride activities in the bulk CH solution: (a) along boundaries 2 and 3 (from point B to point A) after steady-state conditions are reached (b) at point A over time. For clarity, only some of the data points are shown in the plots.

As it can be seen in Figure 4.13a, the largest drop in pH and the largest increase in  $\text{Cl}^-/\text{OH}^-$  occurred at the tip of the crevice (point A), where pH was determined as 12.15 when the chloride activity in the bulk CH solution was 0.039, and  $\text{Cl}^-/\text{OH}^-$  was determined as 24.26 when the chloride activity in the bulk CH solution was 0.342 (*i.e.*,  $\text{Cl}^-/\text{OH}^- = 12.64$ ). Figure 4.13b presents the variation of pH and  $\text{Cl}^-/\text{OH}^-$  at the tip of the crevice (point A) over time for different chloride activities in the bulk CH solution. It can be seen in the  $\text{Cl}^-/\text{OH}^-$  profiles of this figure that it takes the chlorides approximately  $5 \times 10^2$  s to reach point A. During this period, the pH is also relatively stable due to the relative balance between  $\text{OH}^-$  formation in the cathodic reaction on the steel surface and the  $\text{OH}^-$  consumption due to the formation of  $\text{Fe}(\text{OH})_{2(s)}$ . The decrease in pH between  $\sim 10^2$  and  $\sim 2 \times 10^3$  s is mainly the result of the cease of cathodic reaction when the oxygen near point A is completely depleted; hence, no more  $\text{OH}^-$  is produced from the cathodic reaction. In this range, the pH is decreasing at different magnitudes because chlorides are diffusing into the system at different rates; hydroxides are able to move away from the crevice area faster when more charge balancing chlorides are present to maintain the electro-neutrality at this location. The temporary increase in the pH in the range between  $\sim 2 \times 10^3$  and  $\sim 10^4$  s can be attributed to the change in chemical composition due to the increase in chloride activity in the bulk solution. The decrease in pH from  $\sim 10^4$  to  $\sim 10^8$  s can be mainly attributed to the decreasing  $\text{OH}^-$  diffusion from the bulk CH solution to the crevice as the crack and crevice are clogged with  $\text{Fe}(\text{OH})_{2(s)}$ . After  $\sim 10^8$  s the system reaches steady-state conditions for all cases.

The effect of chlorides on the chemistry of the CP solution in the mill scale crack and crevice was investigated by varying the chloride activity in the bulk solution from 0 to 0.837, as shown in Figure 4.14. The chloride activities for the CP solution were larger than those for the CH solution (see Figure 4.13) since experimental evidence, as presented in Section 2.3, shows that depassivation of rebar occurs at larger chloride thresholds in solutions with higher pH. It can be observed in Figure 4.14a that the chlorides in the bulk solution do not significantly affect the pH and  $\text{Cl}^-/\text{OH}^-$  within the crack and crevice: the decrease in pH is negligible for all cases (*i.e.*, largest pH drop ranges from 13.33 to 13.30), while the  $\text{Cl}^-/\text{OH}^-$  increases slightly (6.4 % increase) from the bulk solution towards the tip of the crevice (point A) only when high activities of chlorides are present in the bulk solution. For example, when the activity of chlorides in the bulk solution was 0.837, the  $\text{Cl}^-/\text{OH}^-$  increased to 4.20 at point A from 3.94 in the bulk pore solution. These observations can also be seen in Figure 4.14b, in which the pH and  $\text{Cl}^-/\text{OH}^-$  are presented over time at the tip of the crevice (point A), which is the point where the changes in pH and  $\text{Cl}^-/\text{OH}^-$  are most noticeable.

When comparing these results shown in Figure 4.14 with the results presented in Figure 4.13, it becomes evident that the changes in pH and  $\text{Cl}^-/\text{OH}^-$  in the CH solution are larger than those observed in the CP solution. For example, a chloride activity of 0.342 for the CH solution results in a decrease of 2.2 % in pH and an increase of 63.0 % in  $\text{Cl}^-/\text{OH}^-$ , whereas a chloride activity of 0.338 for the CP solution results in a decrease of 0.2 % in pH and an increase of 6.3 % in  $\text{Cl}^-/\text{OH}^-$ . These relatively small changes in the CP solution is mainly due to the fact that it contained highly soluble KOH and NaOH compounds,

which provide high alkalinity to the solution. In fact, as it can be observed in Tables 3.2 and 3.3, the hydroxide concentration of the CP solution is around 10 times larger than that of the CH solution. This increased amount of hydroxides in the CP solution would result in more interactions taking place among ions, which in turn would decrease the movement of ionic species in the CP solution (in particular, the movement of chlorides towards the tip of the crevice). It should also be mentioned that the pH is a logarithmic function; hence, a similar hydroxide change from the bulk pore solution (point B) to the tip of the crevice (point A) would result in a larger pH change for the CH solution than that of the CP solution.

In summary, for the constant passive density of  $10^{-3} \text{ A/m}^2$  and the given dimensions of the domain in Table 4.3, the amount of chloride in the bulk CH solution was shown to have a negligible effect on pH (*i.e.*, pH does not drop below 10) and a relatively large effect on  $\text{Cl}^-/\text{OH}^-$ . Within the crevice for all simulations,  $\text{Cl}^-/\text{OH}^-$  exceeded typical chloride thresholds, but pH remained above 10; thus, the system would not be able to sustain a local breakdown of the passive film. The CP solution investigated was more protective than the CH solution since  $\text{Cl}^-/\text{OH}^-$  exceeded the threshold value in only one simulation, in which a chloride activity at the bulk pore solution was 0.837.

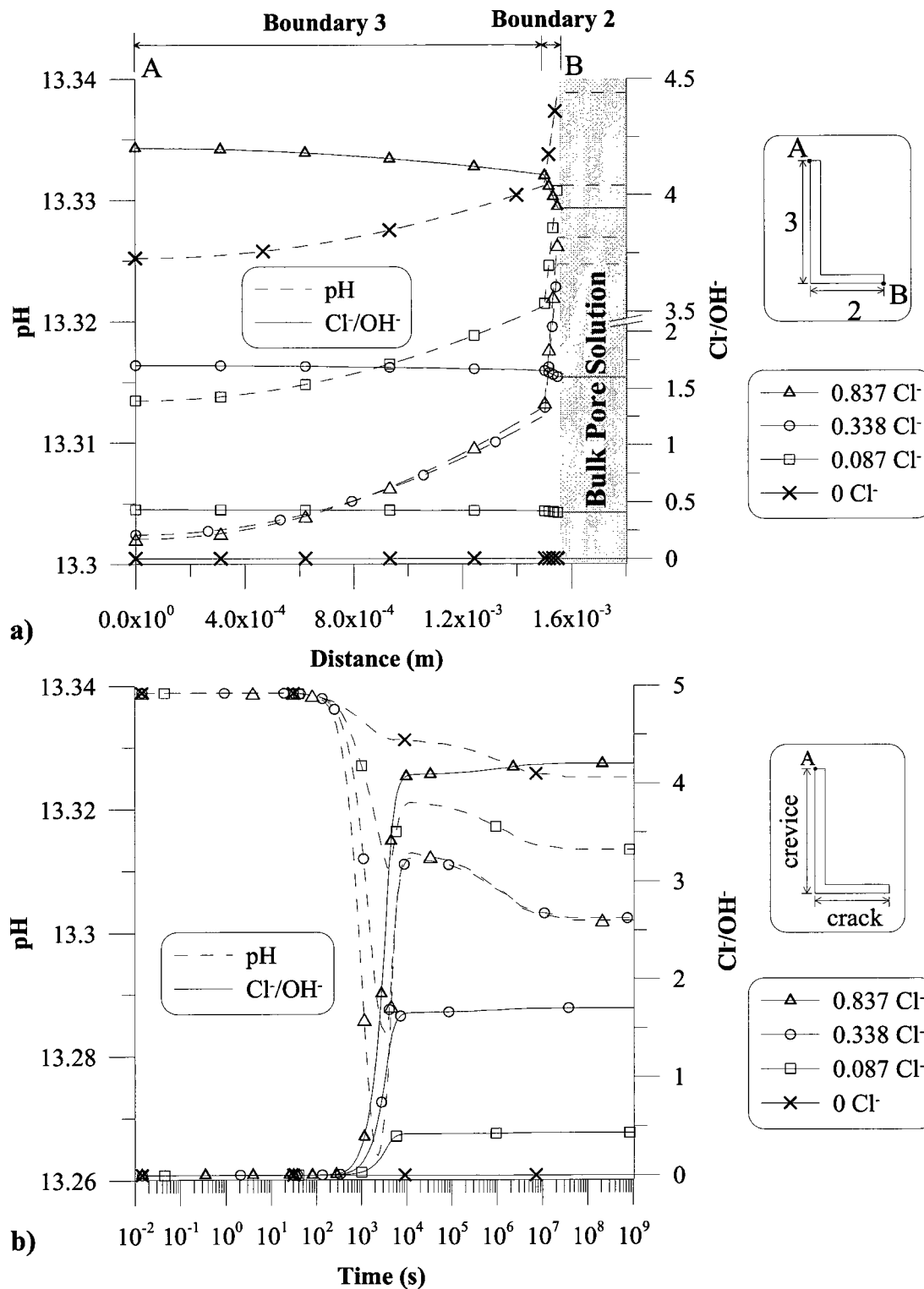


**Figure 4.14.** pH and  $\text{Cl}^-/\text{OH}^-$  at different chloride activities in the bulk CP solution: (a) along boundaries 2 and 3 (from point B to point A) after steady-state conditions are reached (b) at point A over time. For clarity, only some of the data points are shown in the plots.

#### 4.2.1.4 Effect of the diffusion coefficients of the species

Up to this point, the diffusion coefficient of the species were assumed to decrease linearly from  $10^{-9}$  m<sup>2</sup>/s to  $10^{-13}$  m<sup>2</sup>/s as the Fe(OH)<sub>2(s)</sub> concentration increases from 0 to 37,840 mol/m<sup>3</sup>. To determine the effect this change in diffusion coefficient of the species has on the chemical composition of the pore solution in the mill scale cracks and crevices, a comparison of two additional cases was considered in this section. These additional cases include diffusion coefficients of the species that decrease from  $10^{-9}$  m<sup>2</sup>/s to  $10^{-11}$  m<sup>2</sup>/s as Fe(OH)<sub>2(s)</sub> concentration increases from 0 to 37,840 mol/m<sup>3</sup>, and diffusion coefficients of species that remain constant at  $10^{-9}$  m<sup>2</sup>/s regardless of the Fe(OH)<sub>2(s)</sub> concentration. In order to observe the differences between these cases, input parameters which provided the largest drop in pH and the largest increase in Cl<sup>-</sup>/OH<sup>-</sup> in the previous sections were applied, as presented in Table 4.3. These simulations were carried out in the CH solution. A similar investigation was conducted in Section 4.1.1.2 for simulations in chloride-free solutions; therefore, it is of interest to see if similar observations can be made when chlorides are present in the solutions.

In Figure 4.15a, pH and Cl<sup>-</sup>/OH<sup>-</sup> were analyzed along boundaries 2 and 3 (from point B to point A) after steady-state conditions were reached ( $t = \sim 10^9$  s). Figure 4.15a shows pH decreasing and Cl<sup>-</sup>/OH<sup>-</sup> increasing as the diffusion coefficient of the species decrease within the domain. Decreasing the diffusion coefficient as more Fe(OH)<sub>2(s)</sub> builds up in the solution causes the species to move slower, while the reaction rates at the steel and mill scale surfaces remain the same. This effect would increase the activity of iron ions within the crevice area; as a result, more hydroxides will react with iron ions to

precipitate into  $\text{Fe}(\text{OH})_{2(s)}$ , hence, decreasing the hydroxide activity, and in turn, increasing the chloride activity within the crevice area (boundary 3). The changes in pH and  $\text{Cl}^-/\text{OH}^-$  are relatively larger between the case, in which the diffusion coefficient remains constant at  $10^{-9} \text{ m}^2/\text{s}$ , and the other two cases, in which the diffusion coefficient decreases to  $10^{-11}$  and  $10^{-13} \text{ m}^2/\text{s}$ . In fact, the pH and  $\text{Cl}^-/\text{OH}^-$  changes between  $10^{-11}$  and  $10^{-13} \text{ m}^2/\text{s}$  are shown to be negligible in the figure, as there was a 0 % difference in pH and 0.7 % difference in  $\text{Cl}^-/\text{OH}^-$  at the tip of the crevice (point A) where the differences between each simulation are at its largest. On the other hand, the differences observed between the case in which the diffusion coefficient remains constant at  $10^{-9} \text{ m}^2/\text{s}$  and the case in which the diffusion coefficient decreases to  $10^{-11} \text{ m}^2/\text{s}$  showed a 1.1 % difference in pH and 33.6 % difference in  $\text{Cl}^-/\text{OH}^-$  at the tip of the crevice (point A). The differences between the case in which  $D = 10^{-9} \text{ m}^2/\text{s}$  (*i.e.*, diffusion coefficient does not change relative to the amount of  $\text{Fe}(\text{OH})_{2(s)}$  in the pore solution) and the other two cases occurs at approximately  $10^4 \text{ s}$ , as is shown in Figure 4.15b, when the diffusion coefficient becomes the principle parameter which causes the pH to decrease and the  $\text{Cl}^-/\text{OH}^-$  to increase within the crevice.

It should be noted that the same observations that were made in chloride-free pore solutions (Section 4.1.1.2) can also be made when chlorides are added to the system: a decrease in the diffusion coefficient has a relatively large effect on the pH and  $\text{Cl}^-/\text{OH}^-$  of the pore solution chemistry, but these effects diminish as the diffusion coefficient decreases past  $10^{-11} \text{ m}^2/\text{s}$ .

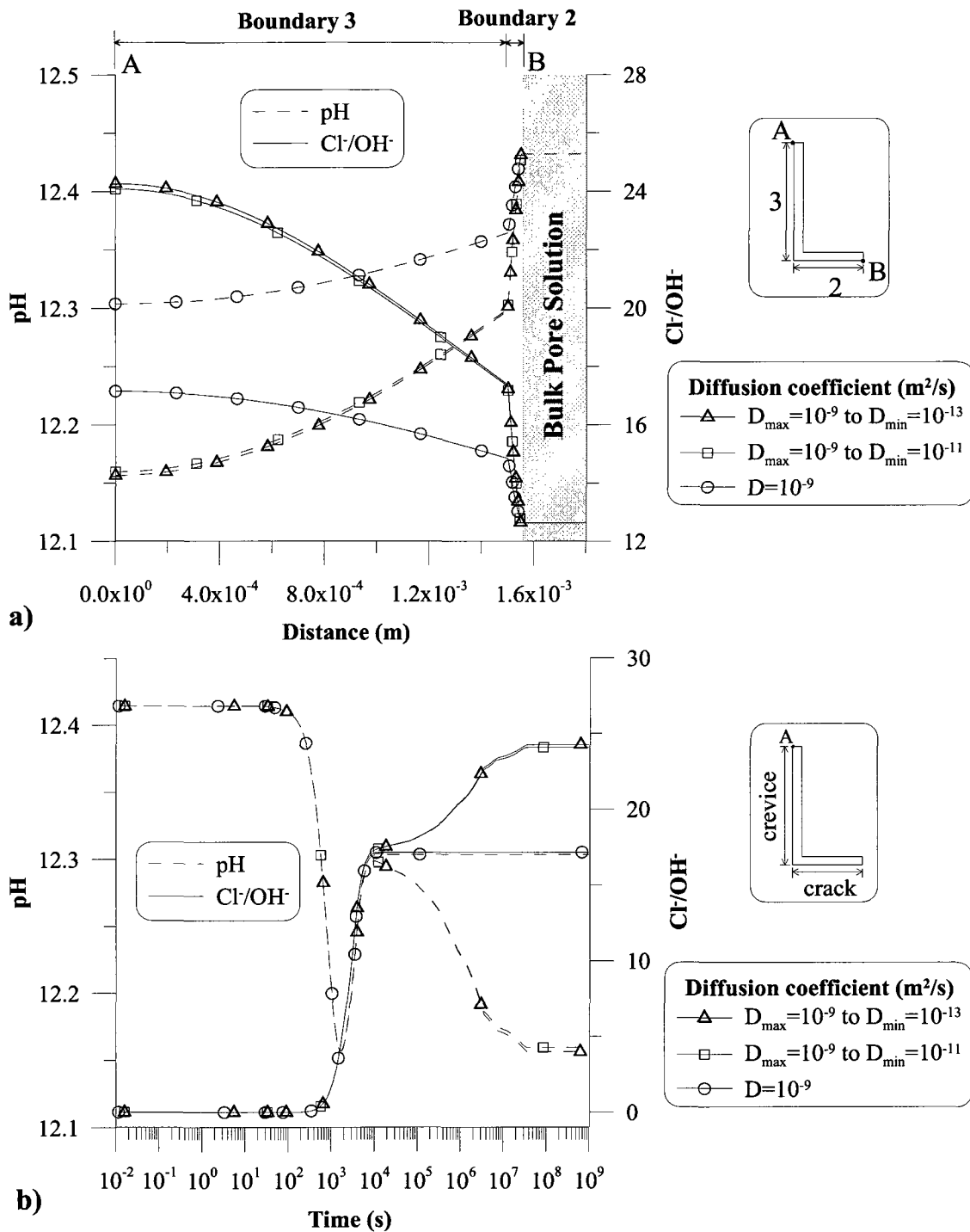


**Figure 4.15.** pH and Cl<sup>-</sup>/OH<sup>-</sup> for different diffusion coefficients that linearly decrease from  $D_{max}$  to  $D_{min}$  as solid compounds expand in the pore solution: (a) along boundaries 2 and 3 (from point B to point A) after steady-state conditions are reached (b) at point A over time. For clarity, only some of the data points are shown in the plots.

#### *4.2.1.5 Summary*

All simulations carried out in this section show that the pore solution chemistry within crevices provided conditions that were more susceptible to depassivation than the conditions in the bulk pore solution; however, none of the simulations met both criteria necessary for a local breakdown of passive film and corrosion initiation. It was mentioned in Section 2.1 of the literature review that conditions past a chloride threshold would predict the onset of corrosion. Most simulations carried out in this section exceed typically-observed chloride thresholds and reached values as high as 24.26 at the tip of the crevice, but the pH of the pore solution still did not decrease below 10 in any of the simulations. Threshold  $\text{Cl}^-/\text{OH}^-$  values higher than 24.26 are not uncommon, as threshold values were reported to range from 0.01 to 45 in Section 2.1 of the literature review; however, studies by Ghods et al. (2009d) suggest that a pH drop below 10 should have been observed for some of the cases (e.g. for cases with chloride concentrations of 1.25 M in the bulk solution). These results might suggest that the passive current density may not be constant until depassivation, as was assumed in this section, and that it might gradually increase after the threshold  $\text{Cl}^-/\text{OH}^-$  is reached (Alonso et al. 2000, Abd El Aal et al. 2009). The next section presents simulations made with this assumption.

### **4.3 Simulations in pore solutions with chlorides – variable $i_p$**

In the previous section, the chemistry of the pore solution within mill scale cracks and crevices were studied with the assumption that the passive current density remained constant until the critical conditions that are necessary for the passive film breakdown are reached, and afterwards, quickly increased to active corrosion rates, as illustrated in Figure 4.7. The movement of species due to the addition of chlorides in concrete pore solution within mill scale cracks and crevices was considered to be the principal cause for the breakdown of the passive film in the previous section; however, the critical alkalinity of the pore solution that is necessary to initiate a local breakdown of the passive film (*i.e.*,  $\text{pH} < 10$ ) was not reached because the transition from the passive to active states was ignored, during which current density increases on the steel surface as the protective passive film reduces in thickness.

As discussed in the literature review, a number of studies have observed that the passive current density remains relatively constant in the presence of small chloride concentrations (*i.e.*, when  $\text{Cl}^-/\text{OH}^-$  is smaller than a threshold), but increases after a threshold  $\text{Cl}^-/\text{OH}^-$  is reached. The increased passive current density persists until the critical conditions that are necessary for the passive film breakdown are reached, and afterwards, quickly increase to active corrosion rates. In the simulations presented in this section, as is illustrated in Figure 4.16, the passive current density,  $i_p$ , was assumed to remain constant until a  $\text{Cl}^-/\text{OH}^-$  of 3 was attained, after which the current density gradually increases to a stable value,  $i_s$ , on the steel surface. When the pH of the pore solution drops below 10, it was assumed that the critical conditions that are necessary for

the passive film breakdown are reached. The increase in the passive current density (*i.e.*, from  $i_p$  to  $i_t$ ) on the steel surface was assumed to take place linearly between the instances when  $\text{Cl}^-/\text{OH}^- = 3$  and  $\text{Cl}^-/\text{OH}^- = 5$ . This assumption was made based on the observations of other researchers in the literature review; however, additional numerical simulations on the selection of these parameters have revealed that, the starting point of the increase from  $i_p$  to  $i_t$  (*i.e.*, the threshold  $\text{Cl}^-/\text{OH}^-$ ) and the assumed range of  $\text{Cl}^-/\text{OH}^-$  during the increase (e.g.  $\text{Cl}^-/\text{OH}^- = 3$  to  $\text{Cl}^-/\text{OH}^- = 5$  in Figure 4.16) are not as important as the magnitude of  $i_t$ , given that  $\text{Cl}^-/\text{OH}^-$  in the crevice exceeds the trigger point for the increase in passive current density (*i.e.*, the threshold  $\text{Cl}^-/\text{OH}^-$ ). Figure 4.17 presents the comparison of two cases with all parameters (e.g. geometry,  $i_p$  and  $i_t$ ), except the chloride threshold and the range of increase from  $i_p$  to  $i_t$ , the same. For one of the cases, the increase from  $i_p$  to  $i_t$  takes place from  $\text{Cl}^-/\text{OH}^-$  of 3 to 5, and for the other case it takes place from  $\text{Cl}^-/\text{OH}^-$  of 5 to 10. In both cases, the threshold  $\text{Cl}^-/\text{OH}^-$  in the pore solution within the crevice was exceeded. It can be seen that, after  $2.3 \times 10^7$  s, both simulations result in similar pH and  $\text{Cl}^-/\text{OH}^-$  profiles. Therefore, it was decided in this section that all simulations would be carried out such that the increase in the passive current density (*i.e.*, from  $i_p$  to  $i_t$ ) on the steel surface was assumed to take place linearly between the instances when  $\text{Cl}^-/\text{OH}^- = 3$  and  $\text{Cl}^-/\text{OH}^- = 5$ ; and the focus would be placed mostly on other parameters such as the magnitude of  $i_t$ .

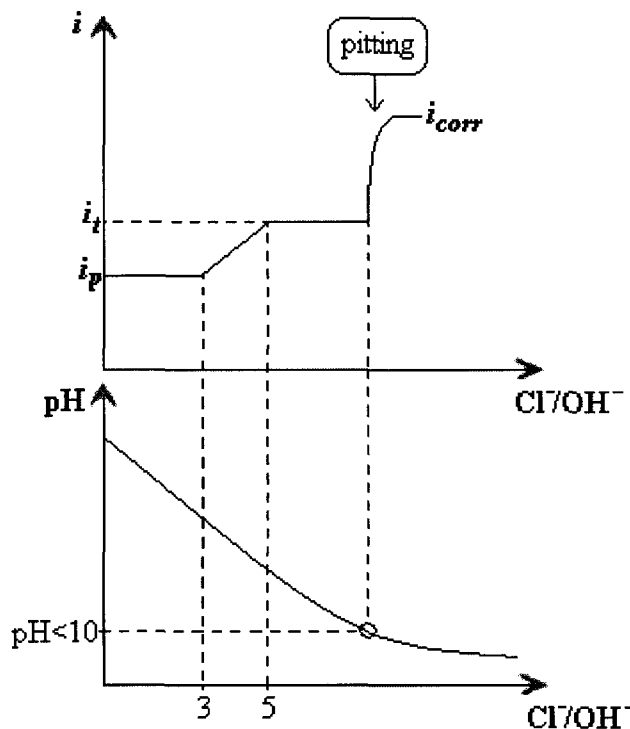


**Figure 4.16.** Assumed depassivation criterion for the simulations carried out in Section 4.3. It was assumed that the passive current density remains constant until a  $\text{Cl}^-/\text{OH}^-$  threshold of 3, after which the current density increases to a steady value until pH drops below 10; afterwards, the current density is assumed to sharply increase to active corrosion rate.

The main objective of the simulations in this section is to investigate if pH of the pore solution in the crevice would drop below 10, creating the necessary conditions for the depassivation and subsequent pitting of the steel. To determine how certain parameters influence the chemistry of the pore solution, specifically pH and  $\text{Cl}^-/\text{OH}^-$ , within mill scale cracks and crevices, the effects of the following parameters were investigated: current density after threshold,  $i_t$ , crevice length ( $c/2$ ), the chloride activity in the bulk concrete pore solution, and diffusion coefficients of the species. Table 4.4 summarizes the parameters of all simulation cases analyzed in this section. Based on experimental studies provided in the literature review (*i.e.*, Section 2.2), a passive current density,  $i_p$ , of  $10^{-3} \text{ A/m}^2$  was used in all simulations. This passive current density,  $i_p$ , remained constant

on mill scale surfaces in each simulation, while on the steel surface it gradually increased to a stable value,  $i_t$ , until depassivation. In addition, based on the results of the previous section, the geometry of the mill scale crack and crevice was mostly fixed (only crevice length was varied) such that crack length ( $l$ ) was  $5 \times 10^{-5}$  m, mill scale crack thickness ( $t_l/2$ ) was  $5 \times 10^{-8}$  m and crevice thickness ( $t_c$ ) was  $1 \times 10^{-6}$  m. These dimensions, while they still realistically represent typical mill scale cracks and crevices, provided the largest drop in pH and the largest increase in  $\text{Cl}^-/\text{OH}^-$  in the simulations of the previous section. However, the effect of crevice length on the chemistry of the pore solution was studied in this section since this parameter has been identified in Section 4.2.1.1 to considerably affect pH and  $\text{Cl}^-/\text{OH}^-$ .

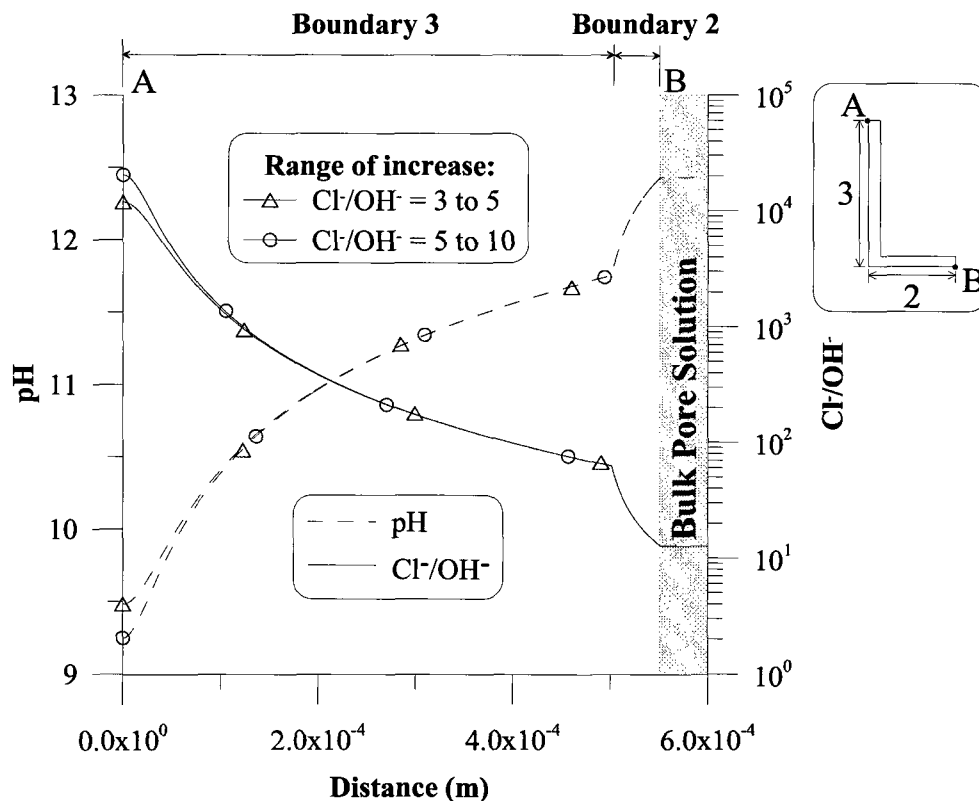


**Figure 4.17.** pH and  $\text{Cl}^-/\text{OH}^-$  in CH solutions (soln. 1 in Table 3.2) along boundaries 2 and 3 (from point B to point A) for a passive current density that linearly increases from  $i_p = 1 \times 10^{-3}$  to  $i_t = 1.7 \times 10^{-2}$   $\text{A}/\text{m}^2$  on the steel surface at different assumed ranges of  $\text{Cl}^-/\text{OH}^-$ . For clarity, only some of the data points are shown in the plots.

**Table 4.4:** Input parameters for all simulations carried out in Section 4.3.

Relevant Section	Passive current density, $i_p$ (A/m <sup>2</sup> )	Treatment of $i_p$ and $i_t$	Current density after threshold $i_t$ (A/m <sup>2</sup> )	Diffusion coefficient, $D_{max}$ to $D_{min}$ (m <sup>2</sup> /s) <sup>(a)</sup>	Activity in bulk pore solution <sup>(b)</sup>	Crevice length, $c/2$ (m)		
4.3.1.1	$1 \times 10^{-3}$	$i_p$ on steel & mill scale; $i_t$ on steel only.	$1 \times 10^{-2}$	$10^{-9}$ to $10^{-13}$	CH soln. 1 in Table 3.2	$5 \times 10^{-4}$		
			$1.5 \times 10^{-2}$					
			$1.7 \times 10^{-2}$					
			$1 \times 10^{-2}$		CP soln. 1 in Table 3.3	$1.5 \times 10^{-3}$		
			$1.7 \times 10^{-2}$					
			$3 \times 10^{-2}$					
$3.5 \times 10^{-2}$								
4.3.1.2			$1 \times 10^{-2}$	$10^{-9}$ to $10^{-13}$	CH soln. 1 in Table 3.2	CH soln. 1 in Table 3.2	$5 \times 10^{-4}$	
							$7.5 \times 10^{-4}$	
							$1 \times 10^{-3}$	
					$1.7 \times 10^{-2}$	CP soln. 1 in Table 3.3	$1.5 \times 10^{-3}$	
							$2 \times 10^{-3}$	
							$2.5 \times 10^{-3}$	
4.3.1.3			$1.7 \times 10^{-2}$	$10^{-9}$ to $10^{-13}$	CH soln. 1 in Table 3.2	CH soln. 1 in Table 3.2	$5 \times 10^{-4}$	
								CH soln. 3 in Table 3.2
					$3.5 \times 10^{-2}$	CP soln. 1 in Table 3.3	$1.5 \times 10^{-3}$	
								CP soln. 2 in Table 3.3
	CP soln. 3 in Table 3.3							
4.3.1.4	$1.5 \times 10^{-2}$	$10^{-9}$ to $10^{-13}$	CH soln. 1 in Table 3.2	CH soln. 1 in Table 3.2	$5 \times 10^{-4}$			
						$10^{-9}$ to $10^{-11}$		
							$10^{-9}$	
			$3 \times 10^{-2}$	CP soln. 1 in Table 3.3	$10^{-9}$ to $10^{-13}$	CP soln. 1 in Table 3.3	$1.5 \times 10^{-3}$	
								$10^{-9}$ to $10^{-11}$

<sup>(a)</sup> Diffusion coefficient of each species change by orders of magnitude from  $D_{max}$  to  $D_{min}$  (see Table 3.4 for specific quantities of each species)

<sup>(b)</sup> Activities linearly change from CH soln. 5 in Table 3.2 and from CP soln. 6 in Table 3.3 ( $[Cl^-] = 0$ ) to its desired solution indicated in the Table 4.4 over a 3600 s period, as discussed in Section 3.4.1

### 4.3.1 Results and discussion

#### 4.3.1.1 Effect of current density after threshold, $i_t$

For the CH solution, pH and  $\text{Cl}^-/\text{OH}^-$  along the mill scale crack (boundary 2) and crevice (boundary 3) are presented for three current densities after threshold,  $i_t$ , as shown in Figure 4.18a. Note that, the analysis for the case with  $i_t = 1.7 \times 10^{-2} \text{ A/m}^2$  was terminated early, before steady-state conditions were reached, since the pH dropped below 10; therefore, pH and  $\text{Cl}^-/\text{OH}^-$  were plotted in Figure 4.18a at a time of  $2.3 \times 10^7 \text{ s}$ , while the other two simulations (*i.e.*,  $i_t$  of  $1 \times 10^{-2}$  and  $1.5 \times 10^{-2} \text{ A/m}^2$ ) were plotted at steady-state conditions (*i.e.*,  $t = 10^9 \text{ s}$ ). All three simulations show pH decreasing and  $\text{Cl}^-/\text{OH}^-$  increasing from the bulk pore solution (point B) to the tip of the crevice (point A). The  $\text{Cl}^-/\text{OH}^-$  in the bulk pore solution was 12.64, which means that the threshold value (*i.e.*,  $\text{Cl}^-/\text{OH}^-$  of 3) was reached within the pore solution for all simulations and that the constant passive current density was able to gradually increase on the steel surface to a stable value,  $i_t$ . This effect was shown more clearly in Figure 4.18b, in which variations of pH and  $\text{Cl}^-/\text{OH}^-$  at the tip of the crevice (point A) over time are presented for different current densities after threshold.

It can be seen in Figure 4.18b for all three simulations that  $\text{Cl}^-/\text{OH}^-$  increased at the same rate when  $\text{Cl}^-/\text{OH}^-$  was smaller than the threshold (since all parameters were equal), but after the threshold, they began to deviate from each other. The deviations in the simulations became more significant as the current density after threshold,  $i_t$ , increased; for example, there was one order of magnitude difference between the results of the cases with  $i_t$  of  $1 \times 10^{-2} \text{ A/m}^2$  and  $1.5 \times 10^{-2} \text{ A/m}^2$  at steady-state conditions (*i.e.*,  $t = 10^9 \text{ s}$ ), but for

$i_t$  of  $1.7 \times 10^{-2} \text{ A/m}^2$ ,  $\text{Cl}^-/\text{OH}^-$  increased drastically by four orders of magnitude as compared with the case with  $i_t$  of  $1.5 \times 10^{-2} \text{ A/m}^2$ . Although the differences in pH were not as significant, similar observations can be made, as there was only a 5 % difference in pH between the cases with  $i_t$  of  $1 \times 10^{-2} \text{ A/m}^2$  and  $1.5 \times 10^{-2} \text{ A/m}^2$  at steady-state, but pH dropped below 10 in the simulation with  $i_t = 1.7 \times 10^{-2} \text{ A/m}^2$ . Specifically, at point A, pH decreased to 12.01 at  $i_t = 1 \times 10^{-2} \text{ A/m}^2$  (3.43 % reduction from point B), 11.41 at  $i_t = 1.5 \times 10^{-2} \text{ A/m}^2$  (8.56 % reduction from point B) and below 10 at  $i_t = 1.7 \times 10^{-2} \text{ A/m}^2$  (> 21 % reduction from point B).

For the CP solution, the current densities after threshold,  $i_t$ , were analyzed at values ranging from  $1 \times 10^{-2}$  to  $3.5 \times 10^{-2} \text{ A/m}^2$ , as presented in Figure 4.19. Since  $\text{Cl}^-/\text{OH}^-$  in the bulk pore solution was 3.94, a stable current density after threshold,  $i_t$ , was reached for all cases investigated. It can be seen in Figure 4.19b that the threshold  $\text{Cl}^-/\text{OH}^-$  of 3 was reached for each simulation at  $\sim 4 \times 10^3 \text{ s}$ , after which pH and  $\text{Cl}^-/\text{OH}^-$  profiles began to deviate from each other. For the simulation with  $i_t$  of  $3.5 \times 10^{-2} \text{ A/m}^2$ , the analysis was terminated before steady-state conditions were reached since pH dropped below 10; hence for this case, the results shown in Figure 4.19a were plotted at a time of  $2.7 \times 10^6 \text{ s}$ , at which the pH was approximately 9.5 at the tip of the crevice; the other cases shown in this figure reached steady-state conditions after  $\sim 10^9 \text{ s}$ . It is shown in Figure 4.19a that the pH dropped and  $\text{Cl}^-/\text{OH}^-$  increased at greater magnitudes towards the tip of the crevice (point A) as the current density after threshold increased on the steel surface; for example, at an  $i_t$  of  $1.7 \times 10^{-2} \text{ A/m}^2$  (*i.e.*,  $i_t$  for which pH dropped below 10 in the CH solution), the pH drop was insignificant as the pH varied from 13.33 at point B to 13.01

at point A (2.43 % reduction); whereas, at an  $i_t$  of  $3 \times 10^{-2} \text{ A/m}^2$ , the pH drop became more significant as it dropped to 12.30 at point A (8.04 % reduction), and to values below 10 (*i.e.*, > 28.6 % reduction) after a slight increase in  $i_t$  (to  $3.5 \times 10^{-2} \text{ A/m}^2$ ). The changes in  $\text{Cl}^-/\text{OH}^-$  were more significant than the change in pH; for example,  $\text{Cl}^-/\text{OH}^-$  increased from 3.94 to values greater than  $10^4$  for  $i_t = 3.5 \times 10^{-2} \text{ A/m}^2$ .

It should be noted that pH and  $\text{Cl}^-/\text{OH}^-$  plots presented in Figure 4.19 were similar to the time plots shown in the previous section (*i.e.*, Sections 4.2.1.3 and 4.2.1.4); however, the changes were more significant in this section due to the additional changes caused by the increase in the passive current density on the steel surface from  $i_p$  to  $i_t$ . An increase in the current density would increase the rate of iron dissolution and reduction reactions at the steel surface; thus, more iron ions would be present in the crevice to react with the hydroxides to form  $\text{Fe}(\text{OH})_{2(s)}$ ; and oxygen molecules would be consumed at a faster rate on the steel surface, which would reduce the amounts of oxygen present in the crevice area for the production of hydroxides.

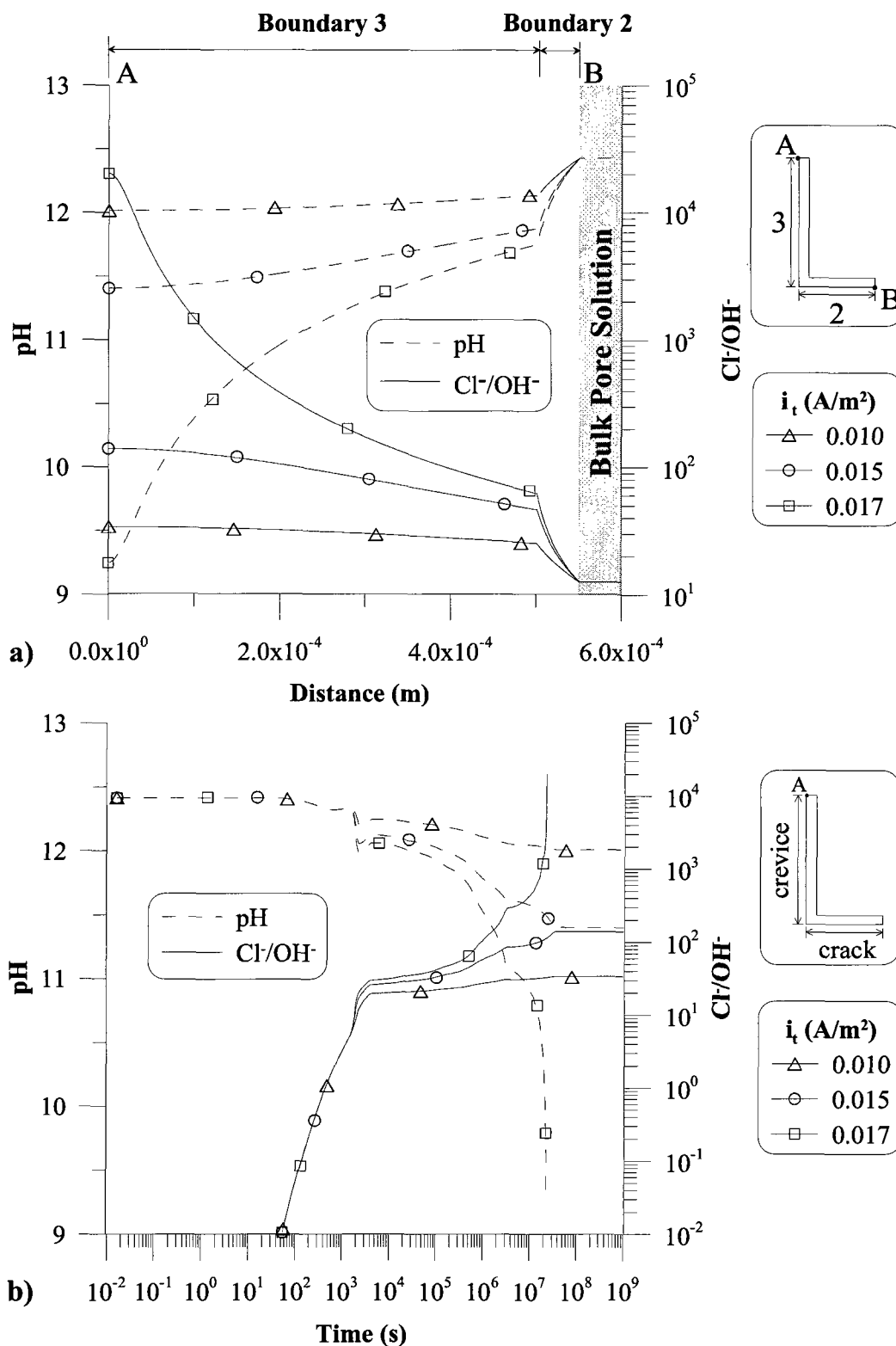


**Figure 4.18.** pH and  $Cl^-/OH^-$  at various current densities after threshold,  $i_t$ , in CH solutions: (a) along boundaries 2 and 3 (from point B to point A) (b) at point A over time. For clarity, only some of the data points are shown in the plots.

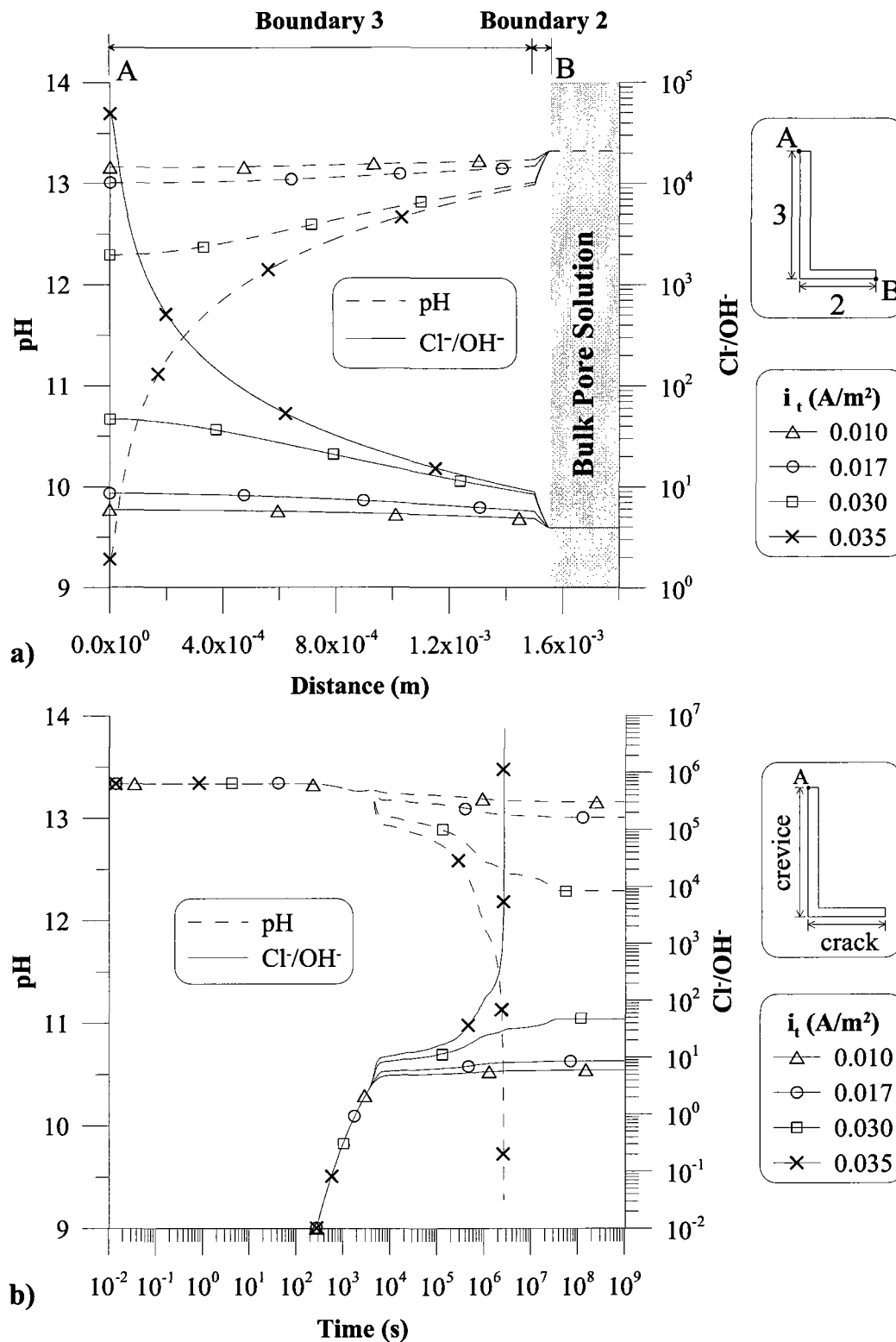


**Figure 4.19.** pH and  $\text{Cl}^-/\text{OH}^-$  at various current densities after threshold,  $i_t$ , in CP solutions: (a) along boundaries 2 and 3 (from point B to point A) (b) at point A over time. For clarity, only some of the data points are shown in the plots.

In summary, for the particular cases analysed in this study, an  $i_t$  of  $1.7 \times 10^{-2} \text{ A/m}^2$  and an  $i_t$  of  $3.5 \times 10^{-2} \text{ A/m}^2$  were required to observe pH drops below 10 in the CH and CP solutions, respectively. Although a larger current density after threshold was needed to bring the pH below 10 for the CP solutions than in CH solutions, which was due to the high alkalinity provided of the CP solutions, the trends in pH and  $\text{Cl}^-/\text{OH}^-$  showed similarities in both pore solutions: pH and  $\text{Cl}^-/\text{OH}^-$  were shown to be sensitive to changes in current density, especially near a pH of 10 at which  $\text{Cl}^-/\text{OH}^-$  was shown to increase drastically by orders of magnitude.

#### *4.3.1.2 Effect of crevice length*

When the effect of crevice length was analyzed for cases with a constant passive current density in the previous section (Section 4.2.1.1), it was shown that an increase in crevice length would result in a decrease in pH and an increase in  $\text{Cl}^-/\text{OH}^-$  within the crevice area (along boundary 3). It was expected that the same relationship would be found for the present case; hence, the main purpose of this section was to determine the critical crevice length necessary to sustain a local breakdown of the passive film (*i.e.*,  $\text{pH} < 10$  and  $\text{Cl}^-/\text{OH}^- > 3$ ) in the crevice area for CH and CP solutions. The input parameters for the simulations carried out in this section are presented in Table 4.4. A current density after threshold,  $i_t$ , of  $1 \times 10^{-2}$  and  $1.7 \times 10^{-2} \text{ A/m}^2$  was applied for the CH and CP solutions, respectively, because in Section 4.3.1.1 these current densities were shown to cause insignificant changes in pH.

The pH and  $\text{Cl}^-/\text{OH}^-$  along the mill scale crack (boundary 2) and steel surface (boundary 3) for the CH solution are shown in Figure 4.20. In this figure, the results of three crevice lengths (*i.e.*,  $c/2 = 5 \times 10^{-4}$  m,  $7.5 \times 10^{-4}$  m and  $1 \times 10^{-3}$  m) were presented for a bulk pore solution with a pH of 12.43 and  $\text{Cl}^-/\text{OH}^-$  of 12.64. For the analysis of the  $5 \times 10^{-4}$  m crevice length (see Figure 4.20a), a  $\text{Cl}^-/\text{OH}^-$  of 33.85 was shown at the tip of the crevice (point A), but the pH drop was only 12.01 at steady-state conditions (*i.e.*,  $t = 10^9$  s); hence both criteria to sustain a local passive film breakdown were not met. For the analysis of the  $7.5 \times 10^{-4}$  m crevice length both criteria were met: a  $\text{Cl}^-/\text{OH}^-$  above 3 and a pH value below 10 were reached, as is illustrated in Figure 4.20b. This plot was taken at a time of  $1.8 \times 10^7$  s when the pH reached  $\sim 9.5$  and  $\text{Cl}^-/\text{OH}^-$  increased from the bulk solution by 3 orders of magnitude. Following this simulation, it is no surprise that the analysis of the  $1 \times 10^{-3}$  m crevice length (see Figure 4.20c) also reached a  $\text{Cl}^-/\text{OH}^-$  above 3 and a pH value below 10; however, this plot reached a pH of  $\sim 9.5$  at an earlier time of  $1 \times 10^5$  s.

For the CP solution, the simulations were carried out at crevice lengths ( $c/2$ ) of  $1.5 \times 10^{-3}$ ,  $2 \times 10^{-3}$  and  $2.5 \times 10^{-3}$  m, as shown in Figure 4.21. The bulk pore solution for each crevice length investigated had a pH of 13.33 and a  $\text{Cl}^-/\text{OH}^-$  of 3.94. As shown in Figure 4.21a, for the case with a crevice length of  $1.5 \times 10^{-3}$  m, the pH decreased to 13.01 and  $\text{Cl}^-/\text{OH}^-$  increased to 8.62 at steady-state conditions (*i.e.*,  $t = 10^9$  s). Although the chloride threshold condition was met, this case would not experience a sustained breakdown in the passive film as the pH drop did not go below 10. The same can be said for the steady-state results shown in Figure 4.21b, in which a pH is shown to decrease to 12.63 for the case with a crevice length of  $2 \times 10^{-3}$  m. For the crevice length of  $2.5 \times 10^{-3}$  m (see Figure

4.21c), on the other hand,  $\text{Cl}^-/\text{OH}^-$  was shown to go well above 3 and pH was shown to drop below 10 at the tip of the crevice (point A) at a time of  $8.4 \times 10^5$  s.

In summary, the crevice length necessary to sustain a local breakdown of the passive film for the particular cases analyzed, as shown in Table 4.4, was  $7.5 \times 10^{-4}$  m for the CH solution ( $i_t = 1 \times 10^{-2}$  A/m<sup>2</sup>) and  $2.5 \times 10^{-3}$  m for the CP solution ( $i_t = 1.7 \times 10^{-2}$  A/m<sup>2</sup>). Ghods et al. (2009c) did not observe crevice lengths larger than  $1.5 \times 10^{-3}$  m in their SEM studies; however, these microscopic studies were only conducted on certain areas of the rebar surface, in particular where pitting was observed. A more detailed microscopic analysis of crevices could reveal longer crevice lengths.

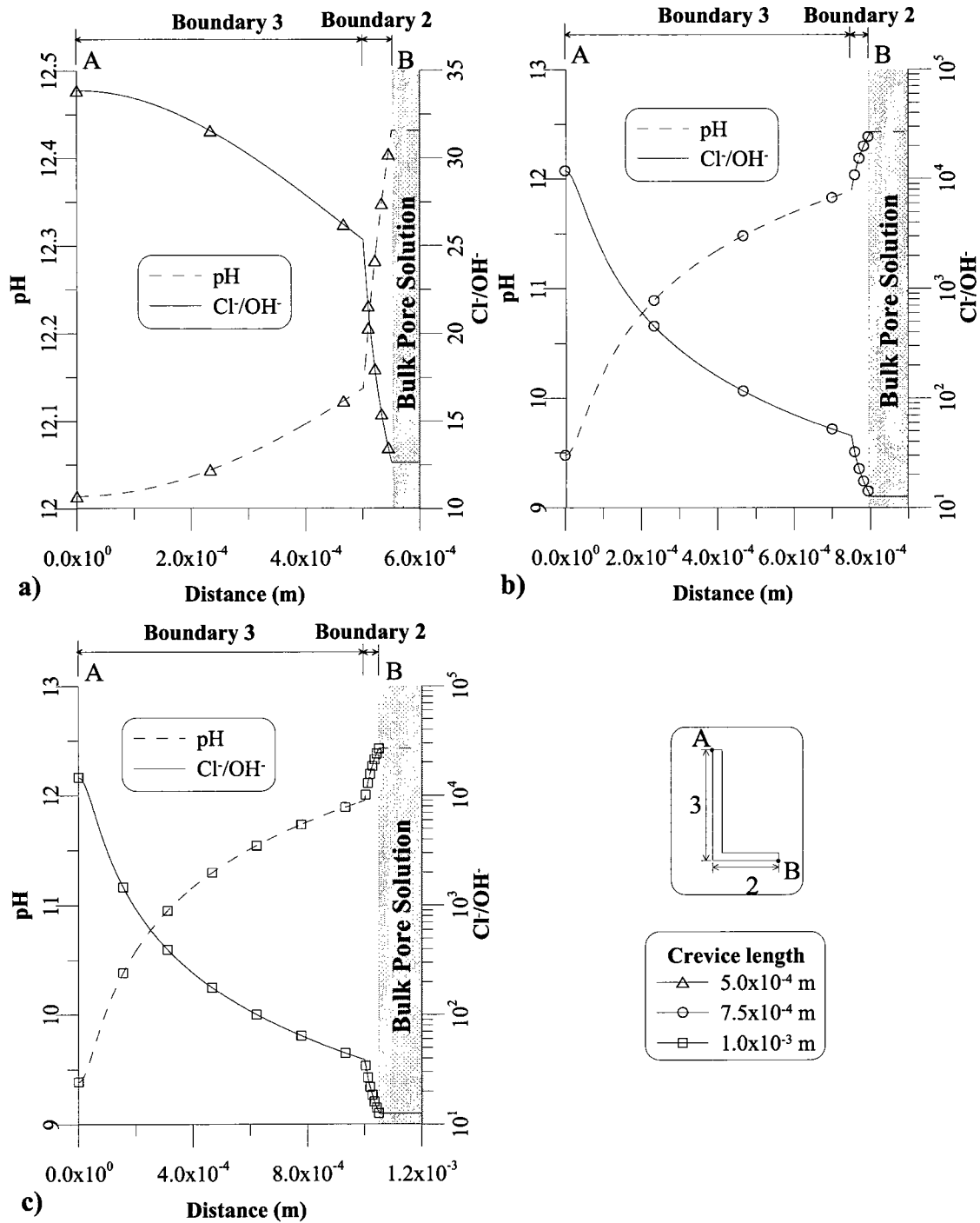


**Figure 4.20.** pH and  $\text{Cl}^-/\text{OH}^-$  for varying crevice lengths in CH solutions along boundaries 2 and 3 (from point B to point A). For clarity, only some of the data points are shown in the plots.

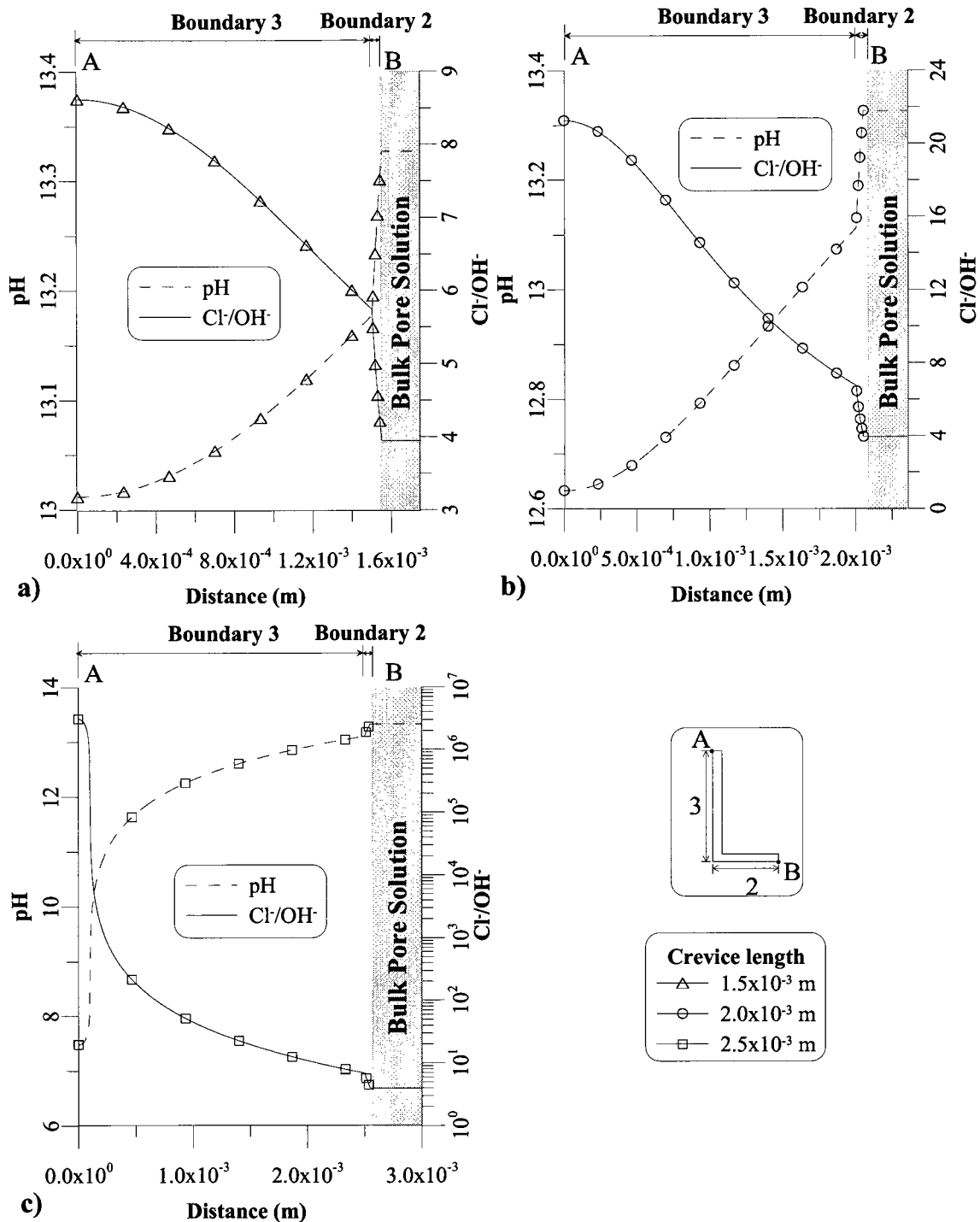


**Figure 4.21.** pH and  $\text{Cl}^-/\text{OH}^-$  for varying crevice lengths in CP solutions along boundaries 2 and 3 (from point B to point A). For clarity, only some of the data points are shown in the plots.

#### 4.3.1.3 Effect of the amount of chloride in the bulk concrete pore solution

The addition of chlorides did not significantly contribute to a drop in alkalinity within the crevice area in the previous section (Section 4.2.1.3), in which simulations were carried out using a constant passive current density. In fact, the pH plots along the mill scale crack (boundary 2) and crevice (boundary 3) were nearly on top of each other in most of the simulations. By implementing a current density at the steel surface that increases after a threshold, a different outcome was expected. The input parameters for the simulations carried out in this section are presented in Table 4.4. A current density after threshold,  $i_t$ , of  $1.7 \times 10^{-2}$  and  $3.5 \times 10^{-2}$  A/m<sup>2</sup> was applied for the CH and CP solutions, respectively, because in Section 4.3.1.1 these current densities were shown to cause the pH drop below 10 at high chloride activity levels (*i.e.*, 0.342 Cl<sup>-</sup> for CH solutions and 0.837 Cl<sup>-</sup> for CP solutions).

Figure 4.22 shows the pH and Cl<sup>-</sup>/OH<sup>-</sup> along the mill scale crack (boundary 2) and crevice length (boundary 3) at three different chloride activities in the bulk CH pore solution: 0.342, 0.075 and 0.039 (*i.e.*, solutions no. 1, 3 and 4 in Table 3.2). In Figure 4.22, the two largest chloride activities in the bulk solution produced results with pH below 10 and Cl<sup>-</sup>/OH<sup>-</sup> above 3 at the tip of the crevice (point A). The results of these two simulations are shown to be nearly equivalent to each other in Figure 4.22a, but the times at which the plots were made were different: the case with a chloride activity of 0.075 reached a pH of  $\sim 9.5$  at a time of  $1.1 \times 10^7$  s, while the case with a chloride activity of 0.342 reached a pH of  $\sim 9.5$  at a time of  $2.3 \times 10^7$  s. The times at which a pH  $\sim 9.5$  was reached for each simulation was shown more clearly in Figure 4.18b, in which variations

of pH and  $\text{Cl}^-/\text{OH}^-$  at the tip of the crevice (point A) over time are presented. The difference in the times between the two simulations can be attributed to the time taken to reach a stable current density after threshold ( $i_t$ ). Since  $\text{Cl}^-/\text{OH}^-$  in the bulk solution for the 0.342  $\text{Cl}^-$  simulation (*i.e.*,  $\text{Cl}^-/\text{OH}^- = 12.64$ ) was larger than the  $\text{Cl}^-/\text{OH}^-$  of the 0.075  $\text{Cl}^-$  simulation (*i.e.*,  $\text{Cl}^-/\text{OH}^- = 2.76$ ), a stable  $i_t$  value (hence a  $\text{Cl}^-/\text{OH}^-$  of 3) was reached earlier for the case with a chloride activity of 0.342. This explains why the 0.342  $\text{Cl}^-$  simulation deviates from the other two simulations by larger margins at a time of  $\sim 10^3$  s. It is interesting to note that the 0.075  $\text{Cl}^-$  simulation attained a  $\text{Cl}^-/\text{OH}^-$  of 3 at a later time of  $7.4 \times 10^4$  s, but still reached a pH  $\sim 9.5$  before the 0.342  $\text{Cl}^-$  simulation. This can be explained by the fact that the 0.075  $\text{Cl}^-$  simulation had nearly reached its stable condition at the time passive current density increased on the steel surface, which caused drastic changes in pH and  $\text{Cl}^-/\text{OH}^-$ . For the 0.342  $\text{Cl}^-$  simulation, other mechanisms were occurring within the crevice at the time passive current density increased to  $i_t$  on the steel surface, which caused the changes to be more moderate. For the simulation in Figure 4.22a, with a chloride activity of 0.039 at the bulk solution (point B),  $\text{Cl}^-/\text{OH}^-$  increases from 1.45 from the bulk pore solution (point B) to 1.65 at the tip of the crevice (point A); this result indicates that a constant passive current density ( $i_p$ ) of  $1 \times 10^{-3} \text{ A/m}^2$  was always applied on the steel surface because the threshold value of 3 was never reached. As a result, the pH shows negligible changes from the bulk pore solution to the tip of the crevice (*i.e.*, pH changes from 12.43 at point B to 12.38 at point A).

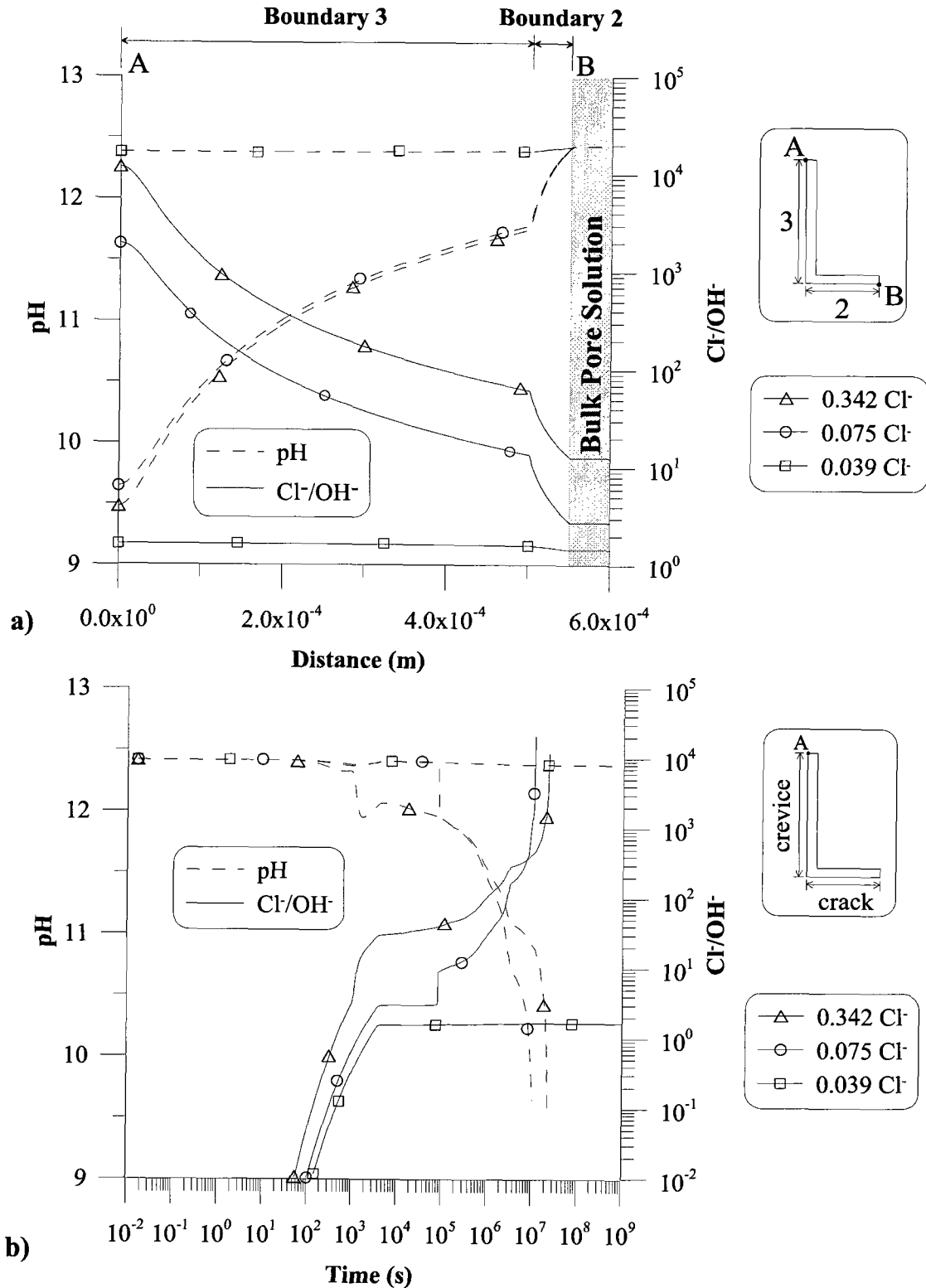


**Figure 4.22.** pH and  $\text{Cl}^-/\text{OH}^-$  at different chloride activities in CH solution: (a) along boundaries 2 and 3 (from point B to point A) (b) at point A over time. For clarity, only some of the data points are shown in the plots.

For the CP solution, pH and  $\text{Cl}^-/\text{OH}^-$  along the mill scale crack (boundary 2) and crevice (boundary 3) were analyzed at three different chloride activities in bulk pore solution: 0.837, 0.671 and 0.504 (*i.e.*, solutions no. 1, 2 and 3 in Table 3.3). The results of these simulations are shown in Figure 4.23a. At chloride activities of 0.837 and 0.671, the pH decreased below 10 and  $\text{Cl}^-/\text{OH}^-$  was well above the threshold value of 3. This indicates that both these simulations would be able to sustain a local passive film breakdown. Similarly to the simulations in the CH solution, the results of the two simulations, which caused pH to drop below 10, were nearly equivalent; however the times at which these simulations were plotted were different. As was shown in Figure 4.23b, the 0.837  $\text{Cl}^-$  simulation reached a pH  $\sim 9.5$  at a time of  $2.7 \times 10^6$  s, while the 0.671  $\text{Cl}^-$  simulation reached a pH  $\sim 9.5$  at a time of  $4.9 \times 10^6$  s. This is mainly because the chloride activity simulation of 0.837 ( $\text{Cl}^-/\text{OH}^-$  was 3.94 at point B) was able to reach a stable current density after threshold before the chloride activity simulation of 0.671 ( $\text{Cl}^-/\text{OH}^-$  was 3.17 at point B). For the simulation in Figure 4.23 with a chloride activity of 0.504 in the bulk solution (point B), a negligible pH drop was shown at steady-state conditions (*i.e.*, pH changes from 13.33 at point B to 13.30 at point A) because  $\text{Cl}^-/\text{OH}^-$  never reached the threshold of 3 within the pore solution ( $\text{Cl}^-/\text{OH}^-$  changes from 2.39 at point B to 2.54 at point A); hence a passive current density of  $1 \times 10^{-3}$  A/m<sup>2</sup> was only applied on the steel surface throughout the solution process.

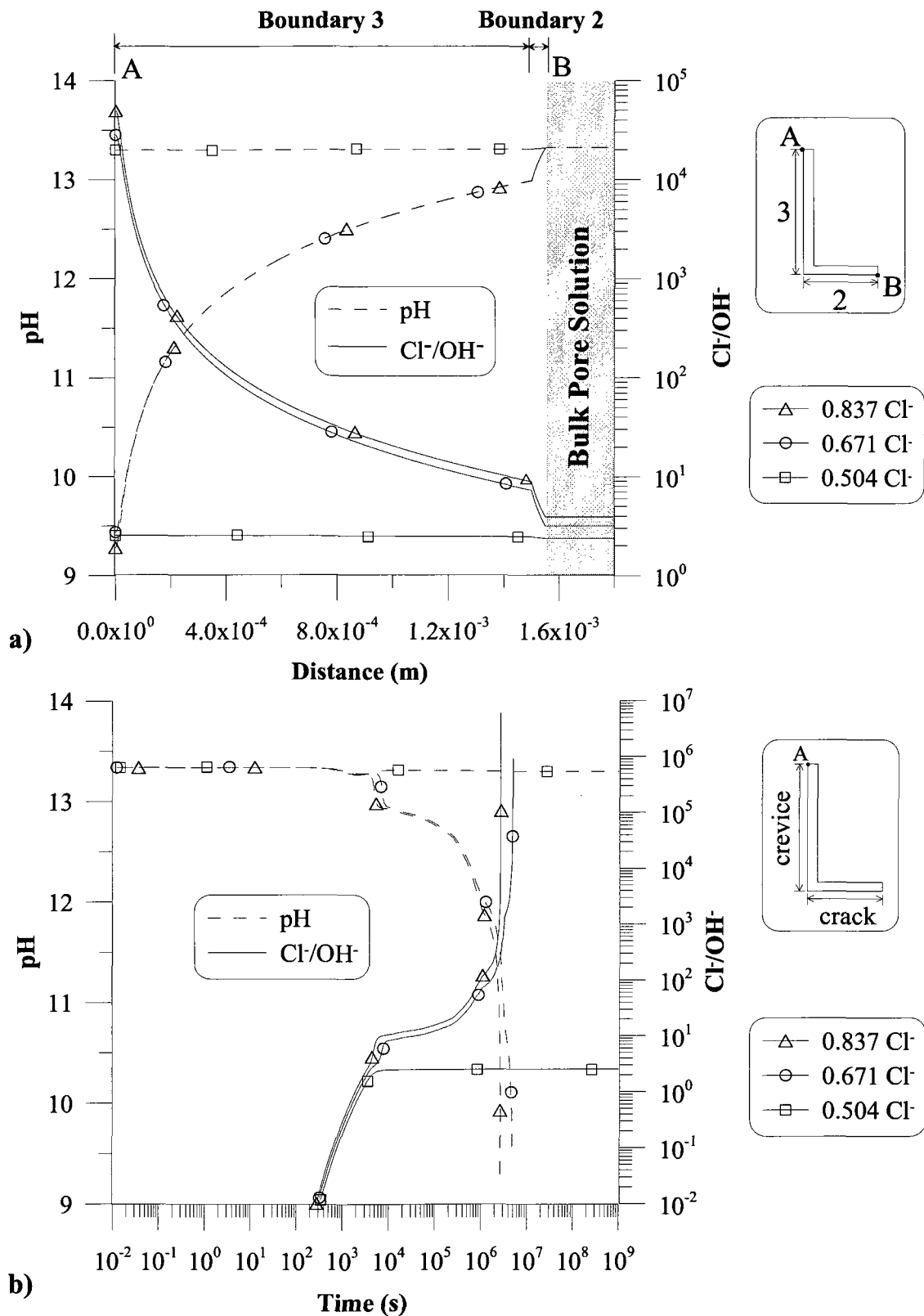


**Figure 4.23.** pH and  $\text{Cl}^-/\text{OH}^-$  at different chloride activities in CP solution: (a) along boundaries 2 and 3 (from point B to point A) (b) at point A over time. For clarity, only some of the data points are shown in the plots.

In summary, a chloride activity of 0.075 (corresponding to a chloride concentration of 0.1 M) in CH solution and a chloride activity of 0.671 (corresponding to a chloride concentration of 1.0 M) in CP solution were the critical chloride activities necessary to sustain a local breakdown of the passive film and initiate pitting for the particular cases analyzed; it should be noted that these chloride activities are within the range of chloride thresholds reported by Ghods et al. (2009d). In this section, the addition of chlorides was shown to have nearly negligible effects before a threshold value was reached; however, after the threshold, the alkalinity of the pore solution significantly decreased, which in turn caused  $\text{Cl}^-/\text{OH}^-$  to increase. These results match the observations of Alonso et al. (2000), González et al. (2005) and Abd El Aal et al. (2009), as discussed in Section 2.2 of the literature review.

#### *4.3.1.4 Effect of the diffusion coefficients of the species*

The effect of a diffusion coefficient that decreases linearly from  $D_{max}$  ( $10^{-9}$  m<sup>2</sup>/s) to  $D_{min}$  ( $10^{-11}$  or  $10^{-13}$  m<sup>2</sup>/s) as  $\text{Fe}(\text{OH})_{2(s)}$  increases from 0 to 37,840 mol/m<sup>3</sup> at any given point in the solution domain was studied in Sections 4.1.1.2 and 4.2.1.4. In both of these sections, two cases were considered: (1) a diffusion coefficient that decreased from  $10^{-9}$  m<sup>2</sup>/s to  $10^{-11}$  m<sup>2</sup>/s and (2) a diffusion coefficient that decreased from  $10^{-9}$  m<sup>2</sup>/s to  $10^{-13}$  m<sup>2</sup>/s as  $\text{Fe}(\text{OH})_{2(s)}$  built up in the solution. Both these cases showed a significant effect on the chemistry of the pore solution, but the difference between them was negligible. In this section, the same two cases were analyzed, as well as a case in which the diffusion coefficient of the species remains constant at  $10^{-9}$  m<sup>2</sup>/s regardless of the build up of  $\text{Fe}(\text{OH})_{2(s)}$ , for both CH and CP solutions. The input parameters for the simulations

carried out in this section are presented in Table 4.4. Current densities after threshold ( $i_t$ ) of  $1.5 \times 10^{-2}$  and  $3 \times 10^{-2}$  A/m<sup>2</sup> were applied for the CH and CP solutions, respectively, because in Section 4.3.1.1 these current densities were shown to cause the largest pH drops without dropping below 10. It was important to analyze the simulations in this section above a pH of 10 because a comparison of the different diffusion cases needed to be carried out and results below a pH of 10 did not reach steady-state conditions when the analyses were terminated.

The pH and Cl<sup>-</sup>/OH<sup>-</sup> results were analyzed at steady-state conditions (*i.e.*,  $t = 10^9$  s) along the mill scale crack (boundary 2) and crevice (boundary 3), as shown in Figure 4.24. Examination of Figure 4.24 showed that pH and Cl<sup>-</sup>/OH<sup>-</sup> variations from the bulk solution (point B) to the tip of the crevice (point A) were significantly affected by a diffusion coefficient that decreased from  $10^{-9}$  m<sup>2</sup>/s to  $10^{-11}$  m<sup>2</sup>/s as Fe(OH)<sub>2(s)</sub> built up; however, the difference was insignificant between this case and the case in which the diffusion coefficient decreased from  $10^{-9}$  m<sup>2</sup>/s to  $10^{-13}$  m<sup>2</sup>/s. In fact, there is only a 7.7 % difference in Cl<sup>-</sup>/OH<sup>-</sup> and a 0.3 % difference in pH at the tip of the crevice area (point A) where the variation is at its largest. Similar differences were observed in Figure 4.25 for the CP solutions. An 8.0 % difference in Cl<sup>-</sup>/OH<sup>-</sup> and a 0.3 % difference in pH were indicated in this figure at the tip of the crevice area (point A). These results confirm that a diffusion coefficient of  $10^{-11}$  m<sup>2</sup>/s and below would cause no significant effect on the system; however, based on the large variances at the tip of the crevice between the case of a constant diffusion coefficient of  $10^{-9}$  m<sup>2</sup>/s and the case of a diffusion coefficient that

decreases from  $10^{-9} \text{ m}^2/\text{s}$  to  $10^{-11} \text{ m}^2/\text{s}$ , as was shown in Figures 4.24 and 4.25, the effect  $\text{Fe}(\text{OH})_{2(s)}$  has on the transport properties cannot be ignored.

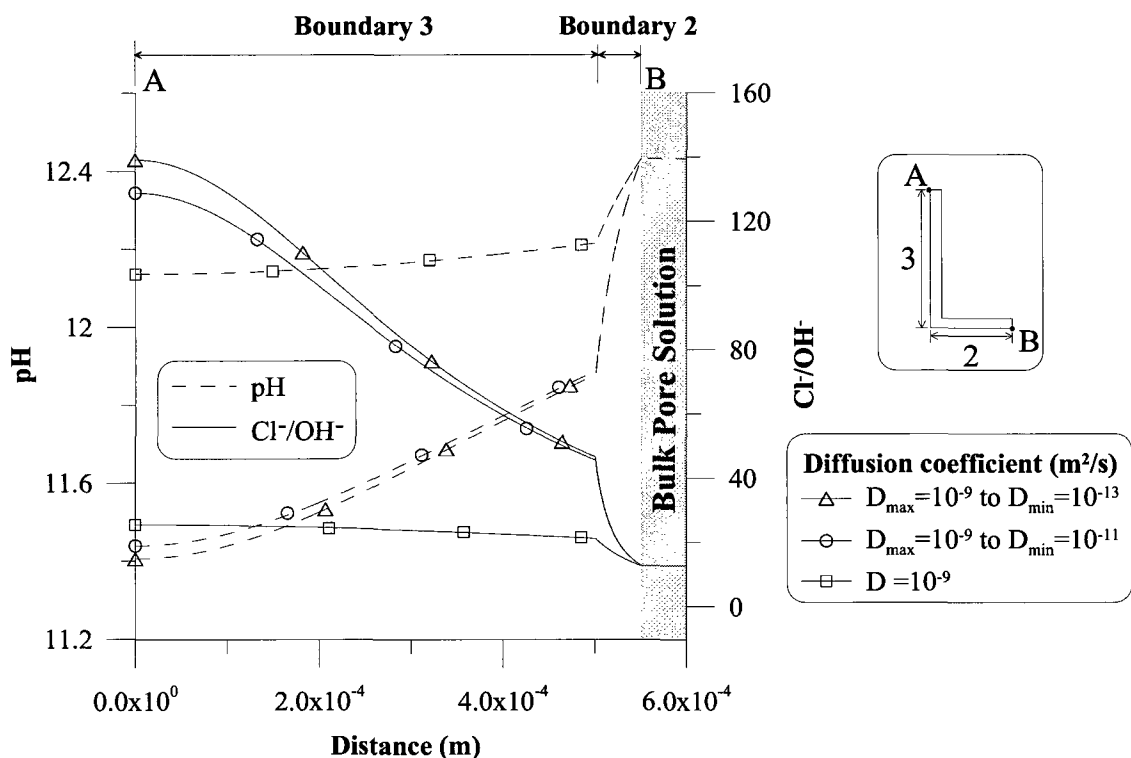


**Figure 4.24.** pH and  $\text{Cl}^-/\text{OH}^-$  for different diffusion coefficients in CH solutions that linearly decrease from  $D_{\max}$  to  $D_{\min}$  as solid compounds expand in the pore solution along boundaries 2 and 3 (from point B to point A). For clarity, only some of the data points are shown in the plots.

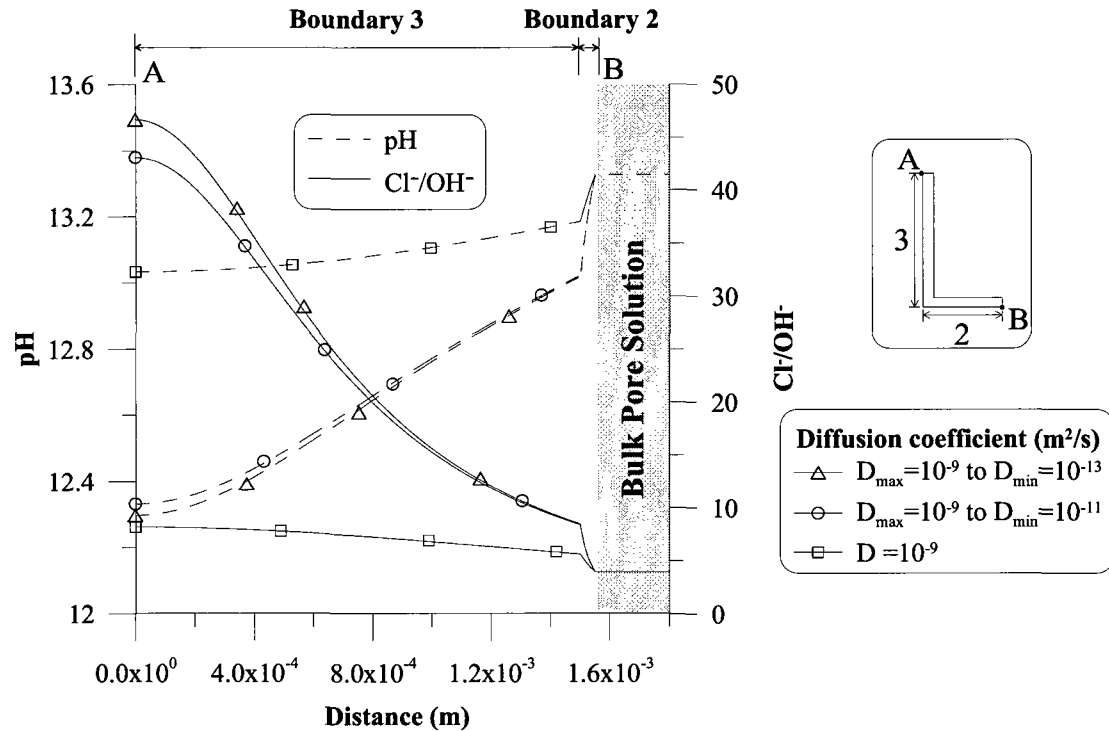


**Figure 4.25.** pH and Cl<sup>-</sup>/OH<sup>-</sup> for different diffusion coefficients in CP solutions that linearly decrease from  $D_{max}$  to  $D_{min}$  as solid compounds expand in the pore solution along boundaries 2 and 3 (from point B to point A). For clarity, only some of the data points are shown in the plots.

#### 4.3.1.5 Summary

The numerical model presented in this section was capable of showing conditions for the sustained local breakdown of the passive film and subsequent pitting of the steel, as a pH below 10 and a Cl<sup>-</sup>/OH<sup>-</sup> above the threshold value of 3 were shown in many of the simulations investigated. This result suggests that the increase in the passive current density on the steel surface beyond the threshold was an important parameter that should not be ignored in the depassivation process. In fact, the investigation of the current density after threshold in Section 4.3.1.1 showed how sensitive the chemistry of the pore solution was to changes in the current density. Investigation of other parameters such as the chloride activity in the bulk concrete pore solution matched observations discussed in the literature review, as small chloride concentrations (*i.e.*, smaller than a threshold) had

no significant effect on the chemistry of the pore solution. The chloride activities necessary to sustain a local breakdown of the passive film in this study are within the range of chloride thresholds reported by Ghods et al. (2009d).

## 5) Conclusions and Future Work

The passive oxide film that forms on the rebar surface due to the highly alkaline environment provided by concrete protects rebar against corrosion until chloride concentrations beyond a threshold are reached. A number of researchers have attributed the variability and uncertainty associated with chloride thresholds to the surface conditions of carbon steel rebar, in particular, to the presence of mill scale on the steel surface. Microscopic studies carried out by Ghods et al. (2009c) demonstrated that mill scales on carbon steel rebars are not uniform in morphology and contained randomly distributed transverse cracks connecting the exposed surface of the rebar to the crevices between the mill scale layer and the underlying steel. It was suggested that the pore solution chemistry in the crevices between the mill scale and the steel surface may be different from that of the bulk pore solution, and this difference may create the necessary conditions for the breakdown of the passive film on the steel surface within a mill scale crevice when chlorides are present. The random nature of the size and distribution of these mill scale cracks and crevices may be partly responsible for the variability and uncertainty associated with chloride thresholds of carbon steel rebars in concrete. The main goal of this study was to test this hypothesis using a numerical approach.

The numerical investigation that was carried out in this thesis involved the solution of coupled extended Nernst-Planck and Poisson's equations under constraints imposed by the chemical reactions and equilibrium requirements in a domain that represented typical mill scale cracks and crevices. The parameters of the numerical investigation involved the

geometry of the domain, pore solution chemistry, the passive current density of the steel and the transport properties of the modelled species. The pore solutions investigated in this study contained species that are present in typical concrete pore solutions; *i.e.*,  $\text{OH}^-$ ,  $\text{Fe}^{2+}$ ,  $\text{Ca}^{2+}$ ,  $\text{Cl}^-$ ,  $\text{Na}^+$ ,  $\text{K}^+$ , and  $\text{O}_{2(\text{g})}$ . In this study, the critical conditions that are necessary for the passive film to breakdown have been assumed to occur when  $\text{Cl}^-/\text{OH}^-$  exceeded a threshold of 3 and pH dropped below 10.

The diversity of the species investigated required the use of a coupled, non-linear and transient solution algorithm, which was implemented using a commercial software package called COMSOL Multiphysics<sup>TM</sup>. Simulations were carried out under three scenarios: (1) simulations in chloride-free pore solutions; (2) simulations in pore solutions with chlorides when the passive current density is constant until depassivation; and (3) simulations in pore solutions with chlorides when the passive current density increases after a predetermined chloride threshold is reached. The main conclusions of the research are presented in the following section.

## **5.1 Conclusions**

The numerical simulations showed that the pore solution chemistry in the crevices between the mill scale and the steel surface was different from that of the bulk pore solution: local acidification (*i.e.*, a drop in pH) and increase in  $\text{Cl}^-/\text{OH}^-$  were observed in all simulations, albeit to different degrees. The largest drop in pH and the largest increase in  $\text{Cl}^-/\text{OH}^-$  consistently occurred at the tip of the crevice, which was the farthest point of the crevice from the bulk solution.

Simulations in chloride-free pore solutions show that the chemistry of the pore solution within mill scale crevices does not change enough to cause the loss of conditions that lead to the formation and maintenance of stable passive films on the steel surface. However, in the presence of chlorides,  $Cl^-/OH^-$  of the pore solution in the crevices were generally larger than reported chloride thresholds, while the pH dropped below 10 under certain conditions.

Simulations in pore solutions with chlorides when the passive current density was assumed to be constant until depassivation showed  $Cl^-/OH^-$  exceeding the typical chloride thresholds within the crevice, but the pH did not drop below 10 in any of the simulations, even for the case for which  $Cl^-/OH^-$  was 24.26 at the tip of the crevice. Threshold  $Cl^-/OH^-$  values higher than 24.26 are not uncommon, as chloride thresholds have been reported to range from 0.01 to 45 in the literature review; however, studies by Ghods et al. (2009d) suggest that a pH drop below 10 should have been observed for some of the cases (e.g. for cases with chloride concentrations of 1.25 M in the bulk solution). Therefore, these simulations suggest that the passive current density may not be constant after  $Cl^-/OH^-$  exceeds the threshold, as reported by a number of experimental works that have been presented in the literature review.

Simulations in pore solutions with chlorides when the passive current density was assumed to increase after a assumed chloride threshold showed that the chemistry of the pore solution within mill scale crevices reached conditions for the sustained local

breakdown of the passive film and subsequent pitting of the steel: pH values below 10 and  $\text{Cl}^-/\text{OH}^-$  values above 3 were obtained in many simulations. This observation suggests that the increase in the passive current density on the steel surface beyond a chloride threshold may be a fact, as reported by a number of researchers; therefore it should not be ignored in the depassivation process. In fact, the parametric investigation of the current density after threshold showed that the chemistry of the pore solution (in particular pH and  $\text{Cl}^-/\text{OH}^-$ ) were sensitive to slight changes in this parameter. The geometry of the domain (*i.e.*, crack and mill scale dimensions) has been found to affect the chemistry of the pore solution within crevices, in which the smaller crack thicknesses and longer crevice lengths provided less favourable conditions for sustaining a stable passive film on steel surfaces within mill scale crevices. The investigation of the effect of chloride activity in the bulk concrete pore solution matched observations discussed in the literature review: small chloride concentrations (*i.e.*, smaller than a threshold) had no significant effect on the chemistry of the pore solution within crevices.

## **5.2 Recommendations for future work**

The following is a list of possible directions for future work that have been identified in the course of the present study:

- The developed model can be improved by adding other reactions to accurately represent more conditions in typical concrete pore solution. In particular, the chemical reactions involving sulphates (*i.e.*,  $\text{SO}_4$ ) can be considered by including the solid phases of ettringite, monosulphates and gypsum (Glasser et al. 2008).

- Microscopic studies carried out by Ghods et al. (2009a) have shown that mill scale on rebar surfaces forms non-uniformly with numerous cracks connecting crevices to the free surface. It is of interest to see what effects these variable geometric characteristics would have on the chemistry of the concrete pore solution within mill scale crevices; therefore, numerical simulations in different domain geometries are recommended.
- It is also of interest to correlate the critical levels of local acidification and increased  $\text{Cl}^-/\text{OH}^-$  values with dimensionless (e.g. crevice thickness-to-crevice length ratio) geometric properties of mill scale crevices. For this, further parametric investigations that focus on the dimensions of mill scale crevices are necessary.
- There are no published data on the ion interaction parameters of iron and calcium ions with hydroxide species, which are required to apply the Pitzer Ion Interaction model (Pitzer 1991) to accurately calculate activities in solutions with ionic strengths up to  $6000 \text{ mol/m}^3$ . A determination of these parameters would be valuable for studying rebar corrosion in highly alkaline concrete pore solutions with high ionic strength; therefore, an experimental study for the determination of these parameters is recommended.
- Although there is strong evidence that mill scale is conductive (Fujii et al. 1999, Marcotte 2001), hence the passive current density can be assumed to be present on mill scale surfaces, the literature on this subject is still not conclusive and further experimental studies are necessary to clarify this uncertainty.

- The literature on the pattern of increase (*i.e.*, sudden vs. gradual) of the passive current density of carbon steel rebar beyond a certain chloride threshold is not conclusive; hence, experimental studies are needed to describe the current density trend from passive to active states more clearly.

## 6) References

- Abd El Aal, E. E., Abd El Wanees, S., Diab, A., and Abd El Haleem, S. M. (2009). "Environmental factors affecting the corrosion behavior of reinforcing steel III. Measurement of pitting corrosion currents of steel in  $\text{Ca}(\text{OH})_2$  solutions under natural corrosion conditions." *Corrosion Science*, 51(8), 1611–1618.
- Alavi, A., and Cottis, R. A. (1983). *Embrittlement by the localised crack environment*, Proc. Conf., Philadelphia, PA, U.S.A.
- Alavi, A., and Cottis, R. A. (1987). "The determination of pH, potential and chloride concentration in corroding crevices on 304 stainless steel and 7475 aluminium alloy." *Corrosion Science*, 27(5), 443-451.
- Alonso, C., Andrade, C., Castellote, M., and Castro, P. (2000). "Chloride threshold values to depassivate reinforcing bars embedded in a standardized OPC mortar." *Cement and Concrete Research*, 30(7), 1047–1055.
- Alonso, C., Castellote, M., and Andrade, C. (2002). "Chloride threshold dependence of pitting potential of reinforcements." *Electrochimica Acta*, 47(21), 3469–3481.
- Andrade, C., and Page, C. L. (1986). "Pore solution chemistry and corrosion in hydrated cement systems containing chloride salts: a study of cation specific effects." *British Corrosion Journal*, 21(1), 49–53.
- Angst, U., Elsener, B., Larsen, C. K., and Vennesland, Ø. (2009). "Critical chloride content in reinforced concrete — A review." *Cement and Concrete Research*, 39(12), 1122–1138.

- Ann, K. Y., and Song, H. W. (2007). "Chloride threshold level for corrosion of steel in concrete." *Corrosion Science*, 49(11), 4113–4133.
- Bamforth, P. B., Price, W. F., and Emerson, M. (1997). *An International Review of Chloride Ingress into Structural Concrete*, Thomas Telford, London.
- Barbarulo, R., Marchand, J., Snyder, K. A., and Prené, S. (2000). "Dimensional analysis of ionic transport problems in hydrated cement systems – Part 1. Theoretical considerations." *Cement and Concrete Research*, 30(12), 1955-1960.
- Bertolini, L., Elsener, B., Pedferri, P., and Polder, R. (2004). *Corrosion of Steel in Concrete*, WILEY-VCH Verlag GmbH & Co. KGaA, Weinheim.
- Breit, W. (1998). "Critical chloride content — investigations of steel in alkaline chloride solutions." *Materials and Corrosion*, 49(8), 539–550.
- Castellote, M., Andrade, C., and Alonso, C. (2002). "Accelerated simultaneous determination of the chloride depassivation threshold and of the non-stationary diffusion coefficient values." *Corrosion Science*, 44(11), 2409–2424.
- Chang, H., Park, Y., and Hwang, W. (2000). "Initiation modeling of crevice corrosion in 316L stainless steels." *Journal of Materials Processing Technology*, 103(2), 206-217.
- Chin, D. T. and Sabde, G. M. (2000). "Modeling transport process and current distribution in a cathodically protected crevice." *Corrosion*, 56(8), 783-793.
- Chuan G. (2005). "A disposable biosensor array for monitoring human metabolic parameters and its applications." *PhD Thesis, University of Cincinnati, U.S.A.*
- COMSOL Multiphysics. (2008). /COMSOL Multiphysics : Version 3.5/, Stockholm, Sweden, COMSOL AB.

- Davies, C. W. (1967). *Electrochemistry*, W. Clowes and Sons, London.
- Dean, J.A. (1999). *Lange's Handbook of Chemistry*, 15th Edition, Table 3.2: Physical Constants of Inorganic Compounds, McGraw-Hill, New York.
- Debye, P., and Hückel, E. (1923). "The theory of electrolytes. I. Lowering of freezing point and related phenomena." *Physikalische Zeitschrift*, 24, 185-192.
- Esmailpoursaee, A. (2007). "An analysis of the factors influencing electrochemical measurements of the condition of reinforcing steel in concrete structures." *PhD Thesis Dissertation, University of Waterloo, Waterloo, Canada*.
- Ferrell, R. T., and Himmelblau, D. M. (1967). "Diffusion coefficients of nitrogen and oxygen in water." *Journal of Chemical and Engineering Data*, 12(1), 111-115.
- Fontana, M. G. (1986). *Corrosion Engineering*, McGraw Hill, New York.
- Fujii, T., Groot, F. M. F., Sawatzky, G. A., Voogt, F. C., Hibma, T., and Okada, K. (1999). "In situ XPS analysis of various iron oxide films grown by NO<sub>2</sub>-assisted molecular-beam epitaxy." *Physical Review B*, 59(4), 3195-3202.
- Ghods, P., Isgor, O. B., and Pour-Ghaz, M. (2007). "A practical method for calculating the corrosion rate of uniformly depassivated reinforcing bars in concrete." *Materials and Corrosion*, 58(4), 265-272.
- Ghods, P., Isgor, O. B., and McRae, G. (2008a). *Investigation of the passive film characteristics of steel in concrete using electrochemical tests*, Passivity and Localized Corrosion, NACE International Conference & Expo, New Orleans, Louisiana, U.S.A.

- Ghods, P., Isgor, O. B., and Pour-Ghaz, M. (2008). "Experimental verification and application of a practical corrosion model for uniformly depassivated steel in concrete." *Materials and Structures*, 41(7), 1211-1223.
- Ghods, P. (2009). "Multi-scale investigation of the formation and breakdown of passive films on steel in concrete." *PhD Thesis Dissertation (unexamined copy)*, Carleton University, Ottawa, Canada.
- Ghods, P., Karadakis, K., Isgor, O. B., and McRae, G. (2009a). *Modeling the effect of mill scale on the local depassivation of steel rebar in concrete*, NACE International, Atlanta, Georgia, U.S.A.
- Ghods, P., Isgor, O. B., McRae, G., Gu, G. P., and Li, J. (2009b). *Effect of surface condition on the chloride-induced depassivation of rebar in concrete*, 12th Int. Conference on Fracture, Ottawa, Canada.
- Ghods, P., Isgor, O. B., McRae, G., Li, J., and Gu, G. P. (2009c). "SEM investigation of mill scale and its effect on the chloride-induced depassivation of black steel Rebar." (*Submitted*).
- Ghods, P., Isgor, O. B., McRae, G., and Gu, G. P. (2009d). "Electrochemical investigation of chloride-induced depassivation of black steel rebar under simulated service conditions." (*Submitted*).
- Ghods, P., Isgor, O. B., McRae, G., and Miller, T. (2009e). "The effect of concrete pore solution composition on the quality of passive oxide films on black steel reinforcement." *Cement & Concrete Composites*, 31(1), 2-11.
- Glass, G. K., and Buenfeld, N. R. (2000a). "Chloride-induced corrosion of steel in concrete." *Progress in Structural Engineering and Materials*, 2(4), 448-458.

- Glass, G. K., and Buenfeld, N.R. (2000b). "The influence of chloride binding on the chloride induced corrosion risk in reinforced concrete." *Corrosion Science*, 42(2), 329-344.
- Glass, G. K., Reddy, B., and Buenfeld, N. R. (2000). "The participation of bound chloride in passive film breakdown on steel in concrete." *Corrosion Science*, 42(11), 2013-2021.
- Glasser, F. P., Marchand, J., and Samson, E. (2008). "Durability of concrete - degradation phenomena involving detrimental chemical reactions." *Cement and Concrete Research*, 38(2), 226-246.
- Goñi, S., and Andrade, C. (1990). "Synthetic concrete pore solution chemistry and rebar corrosion rate in the presence of chlorides." *Cement and Concrete Research*, 20(4), 525-539.
- González, J. A., Miranda, J. M., Birbilis, N., and Feliu, S. (2005). "Electrochemical techniques for studying corrosion of reinforcing steel: limitations and advantages." *Corrosion*, 61(1), 37-50.
- Hansson, C. M., Frolund, T., and Markussen, J. B. (1985). "The effect of chloride cation type on the corrosion of steel in concrete by chloride salts." *Cement and Concrete Research*, 15(1), 65-73.
- Hansson, M., and Sørensen, B. (1990). *Corrosion Rates of Steel in Concrete* (eds. N.S. Berke, V. Chaker and D. Whiting), ASTM STP 1065, 3-16.
- Harb, J. N., and Alkire, R. C. (1991). "Transport and reaction during pitting corrosion of Ni in 0.5M NaCl - I. Stagnant fluid." *Journal of the Electrochemical Society*, 138(9), 2594-2600.

- Hausmann, D. A. (1967). "Steel corrosion in concrete – How does it occur." *Materials Protection*, 6(11), 19–23.
- Heppner, K. L., Evitts, R. W., and Postlethwaite, J. (2004). "Effect of the crevice gap on the initiation of crevice corrosion in passive metals." *Corrosion*, 60(8), 718-729.
- Hindmarsh, A. C., Brown, P. N., Grant, K. E., Lee, S. L., Serban, R., Shumaker, D. E., and Woodward, C. S. (2005). "Sundials: suite of nonlinear and differential/algebraic equation solvers." *ACM Transactions on Mathematical Software*, 31(3), 363-396.
- Hurley, M. F., and Scully, J. R. (2006). "Threshold chloride concentrations of selected corrosion-resistant rebar materials compared to carbon steel." *Corrosion*, 62(10), 892-904.
- Hussain, S. E., Rasheeduzzafar, A., Al-Musallam, A., and Al-Gahtani, A. S. (1995). "Factors affecting threshold chloride for reinforcement corrosion in concrete." *Cement and Concrete Research*, 25(7), 1543–1555.
- Isgor, O. B., and Razaqpur, A. G. (2006). "Modelling steel corrosion in concrete structures." *Materials and Structures*, 39(3), 291–302.
- Jain, J., and Neithalath, N. (2009). "Analysis of calcium leaching behavior of plain and modified cement pastes in pure water." *Cement & Concrete Composites*, 31(3), 176–185.
- Jones, D. A. (1996). *Principles and Prevention of Corrosion*, Second Edition, Prentice Hall, New Jersey.

- Lambert, P., Page, C. L., and Vassie, P. R. W. (1991). "Investigations of reinforcement corrosion. 2. Electrochemical monitoring of steel in chloride-contaminated concrete." *Materials and Structures*, 24(5), 351–358.
- LeVeque, R. J. (2005). *Numerical Methods for Conservative Laws*, 2nd ed. Edition, Birkhäuser, Basel.
- Li, L. Y., and Page, C. L. (1998). "Modelling of electrochemical chloride extraction from concrete: Influence of ionic activity coefficients." *Computational Material Science*, 9(3), 303-308.
- Li, L., and Sagüés, A. A. (2001). "Chloride corrosion threshold of reinforcing steel in alkaline solutions — open-circuit immersion tests." *Corrosion*, 57(1), 19–28.
- Li, L., and Sagüés, A. A. (2002). "Chloride corrosion threshold of reinforcing steel in alkaline solutions—cyclic polarization behavior." *Corrosion*, 58(4), 305-316.
- Mammoliti, L. (1995). "Evaluation of corrosion inhibitors in synthetic concrete pore solutions." *M.Sc. Thesis, University of Waterloo, Waterloo, Canada*.
- Mammoliti, L. T., Brown, L. C., Hansson, C. M., and Hope, B. B. (1996). "The influence of surface finish of reinforcing steel and pH of the test solution on the chloride threshold concentration for corrosion initiation in synthetic pore solutions." *Cement and Concrete Research*, 26(4), 545–550.
- Manera, M., Vennesland, Ø., and Bertolini, L. (2008). "Chloride threshold for rebar corrosion in concrete with addition of silica fume." *Corrosion Science*, 50(2), 554–560.
- Marchand, J. (2001). "Modeling the behavior of unsaturated cement systems exposed to aggressive chemical environments." *Materials and Structures*, 34(4), 195-200.

- Marcotte, T. D. (2001). "Characterization of chloride-induced corrosion products that form in steel-reinforced cementitious materials." *PhD Thesis, Mechanical Engineering, University of Waterloo, Waterloo, Canada.*
- Marinoni, N., Pavese, A., Voltolini, M., and Merlini, M. (2008). "Long-term leaching test in concretes: An x-ray powder diffraction study." *Cement & Concrete Composites*, 30(8), 700–705.
- Mohammed, T. U., and Hamada, H. (2006). "Corrosion of steel bars in concrete with various steel surface conditions." *ACI Materials Journal*, 103(4), 233–242.
- Moreno, M., Morris, W., Alvarez, M. G., and Duffó, G. S. (2004). "Corrosion of reinforcing steel in simulated concrete pore solutions: effect of carbonation and chloride content." *Corrosion Science*, 46(11), 2681–2699.
- Morris, W., Vico, A., and Vázquez, M. (2004). "Chloride induced corrosion of reinforcing steel evaluated by concrete resistivity measurements." *Electrochimica Acta*, 49(25), 4447–4453.
- Oh, B. H., Jang, S. Y., and Shin, Y. S. (2003). "Experimental investigation of the threshold chloride concentration for corrosion initiation in reinforced concrete structures." *Magazine of Concrete Research*, 55(2), 117–124.
- Page, C. L. (1975). "Mechanism of corrosion protection in reinforced concrete marine structures." *Nature*, 258(11), 514–515.
- Page, C. L., Short, N. R., and Holden, W. R. (1986). "The influence of different cements on chloride-induced corrosion of reinforcing steel." *Cement and Concrete Research*, 16(1), 79–86.

- Perez, N. (2004). *Electrochemistry and Corrosion Science*, Kluwer Academic Publishers, Boston.
- Pettersson, K. (1995). *Chloride threshold value and the corrosion rate in reinforced concrete*, Proc. of the Nordic Seminar, Lund, Sweden.
- Pillai, R. G., and Trejo, D. (2005). "Surface condition effects on critical chloride threshold of steel reinforcement." *ACI Materials Journal*, 102(2), 103-109.
- Pitzer, K. S. (1991). *Activity Coefficients in Electrolyte Solution*, 2<sup>nd</sup> Edition, CRC Press, Boston.
- Poupard, O., Aït-Mokhtar, A., and Dumargue, P. (2004). "Corrosion by chlorides in reinforced concrete: determination of chloride concentration threshold by impedance spectroscopy." *Cement and Concrete Research*, 34(6), 991–1000.
- Poursaei, A., and Hansson, C. M. (2007). "Reinforcing steel passivation in mortar and pore solution." *Cement and Concrete Research*, 37(7), 1127–1133.
- Pour-Ghaz, M., Isgor, O. B., and Ghods, P. (2009). "The effect of temperature on the corrosion of steel in concrete. Part 1: Simulated polarization resistance tests and model development." *Corrosion Science*, 51(2), 415-425.
- Rajagopalan, K. S., Venu, K., and Balakrishnan, K. (1962). "Anodic polarization studies in neutral and alkaline solutions containing corrosion inhibitors. I. NaOH–NaCl system." *Journal of the Electrochemical Society*, 109(2), 81–87.
- Ramachandran, V. S. (1995). *Concrete Admixtures Handbook - Properties, Science, and Technology (2nd Edition)*. William Andrew Publishing/Noyes, New Jersey.

- Reddy, B., Glass, G. K., Lim, P. J., and Buenfeld, N. R. (2002). "On the corrosion risk presented by chloride bound in concrete." *Cement & Concrete Composites*, 24(1), 1-5.
- Revie, R. W. (2000). *Uhlig's Corrosion Handbook (2nd Edition)*, John Wiley & Sons, New York.
- Roberge, P. R. (2000). *Handbook of Corrosion Engineering*, McGraw-Hill, New York.
- Roberts, W. L. (1983). *Hot Rolling of Steel (Manufacturing Engineering and Materials Processing)*, Marcel Dekker Inc., New York.
- Rubin, J. (1983). "Transport of reacting solutes in porous media: relation between mathematical nature of problem formulation and chemical nature of reactions." *Water Resources Research*, 19(5), 1231-1252.
- Samson, E., and Marchand, J. (1999). "Numerical solution of the extended Nernst-Planck model." *Journal of Colloid and Interface Science*, 215(1), 1-8.
- Samson, E., Marchand, J., and Beaudoin, J. J. (1999a). "Describing ion diffusion mechanisms in cement-based materials using the homogenization technique." *Cement and Concrete Research*, 29(8), 1341-1345.
- Samson, E., Lemaire, G., Marchand, J., and Beaudoin, J. J. (1999b). "Modeling chemical activity effects in strong ionic solutions." *Computational Materials Science*, 15(3), 285-294.
- Samson, E., Marchand, J., Robert, J. L., and Bournazel, J. P. (1999c). "Modelling ion diffusion mechanisms in porous media." *International Journal for Numerical Methods in Engineering*, 46(12), 2043-2060.

- Samson, E., Marchand, J., and Beaudoin, J. J. (2000). "Modeling the influence of chemical reactions on the mechanisms of ionic transport in porous materials – An overview." *Cement and Concrete Research*, 30(12), 1895-1902.
- Samson, E., and Marchand, J. (2007). "Modeling the transport of ions in unsaturated cement-based materials." *Computers and Structures*, 85(23-24), 1740-1756.
- Saremi, M., and Mahallati, E. (2002). "A study on chloride-induced depassivation of mild steel in simulated concrete pore solution." *Cement and Concrete Research*, 32(12), 1915–1921.
- Schenk, O., Gärtner, K., and Fichtner, W. (1999). "Efficient sparse LU factorization with left-right looking strategy on shared memory multiprocessors." *BIT Numerical Mathematics*, 40(1), 158-176.
- Schenk, O., and Gärtner, K. (2004). "Solving unsymmetric sparse systems of linear equations with PARDISO." *Future Generation Computer Systems*, 20(3), 475-487
- Schenk, O., and Nguyen, D. P. (2007). *PARDISO Solver Project*, software PARDISO. <<http://www.pardiso-project.org/>> (accessed in May, 2009).
- Schiessl, P., and Lay, S. (2005). *Corrosion in Reinforced Concrete Structures* (ed. H. Böhni ), Woodhead Publishing Limited, Cambridge, 91–134.
- Sharland, S. M., and Tasker, P. W. (1988). "A mathematical model of crevice and pitting corrosion. I. The physical model." *Corrosion Science*, 28(6), 603-620.
- Sharland, S. M., Jackson, C. P., and Diver, A. J. (1989). "A finite-element model of the propagation of corrosion crevices and pits." *Corrosion Science*, 29(9), 1149-1166.

- Sikora, E., and Macdonald, D. D. (2002). "Nature of the passive film on nickel." *Electrochimica Acta*, 48(1), 69-77.
- Trejo, D., and Pillai, R. G. (2003). "Accelerated chloride threshold testing: Part I - ASTM A 615 and A 706 reinforcement." *ACI Materials Journal*, 100(6), 519-527.
- Uhlig, H. H., and Revie, R. W. (1985). *Corrosion and Corrosion Control: an Introduction to Corrosion Science and Engineering*, Third Ed., John Wiley & Sons, New York.
- Vankeerberghen, M. (2004). "Critical characteristic dimension or geometry for determining the susceptibility of a crevice to crevice corrosion." *Corrosion*, 60(8), 707-717.
- Venu, K., Balakrishnan, K., and Rajagopalan, K. S. (1965). "A potentiokinetic polarization study of the behaviour of steel in NaOH-NaCl system." *Corrosion Science*, 5(1), 59-69.
- Yonezawa, T., Ashworth, V., and Procter, R. P. M. (1988). "Pore solution composition and chloride effects on the corrosion of steel in concrete." *Corrosion*, 44(7), 489-499.
- Zimmermann, L. (2000). "Korrosionsinitiiender chloridgehalt von stahl in beton." *Dissertation, ETH Nr. 13870, ETH Zürich, Switzerland.*

## Appendix A: Solution Process of COMSOL™

This Appendix presents an explanation of the solution process taken by COMSOL Multiphysics™ in solving the boundary-value problem defined in Sections 3.1 to 3.5. To solve all governing equations simultaneously for each species being considered in this model, COMSOL Multiphysics™ uses the Galerkin formulation of the finite element method (FEM). First, the software collects all the equations and boundary conditions into one large system of partial differential equations (PDE) and boundary conditions in a *generic form*, which is well suited for nonlinear problems:

$$e_a \frac{\partial^2 u}{\partial t^2} + d_a \frac{\partial u}{\partial t} + \nabla \cdot \Gamma = F_s \quad \text{in } \Omega \quad (\text{A.1})$$

$$-\mathbf{n} \cdot \Gamma = G + \left( \frac{\partial R_d}{\partial u} \right)^T \mu \quad \text{on } \partial\Omega \quad (\text{A.2})$$

$$R_d = 0 \quad \text{on } \partial\Omega \quad (\text{A.3})$$

where  $e_a$  is the mass coefficient,  $\partial^2 u / \partial t^2$  is the mass matrix for dependent variable  $u$ ,  $d_a$  is the damping/mass coefficient,  $\partial u / \partial t$  is the damping matrix for dependent variable  $u$ ,  $\Gamma$  is the flux vector,  $F_s$  is the source term, and  $R_d$  and  $G$  are general coefficients. The term  $\mu$  in equation (A.2), refers to the Lagrange multiplier that is multiplied to the transpose of the constraint matrix so that the model becomes solvable when constraints (*i.e.*, Dirichlet boundary conditions) are imposed on the dependent variables. Equations (A.1), (A.2) and (A.3) represent the PDE's governing the processes in the domain of analysis, the Neumann boundary conditions and the Dirichlet boundary conditions, respectively. The next step includes converting all equations into a system of linear

equations ( $Ax = b$ ) using a *weak solution form*; the *weak form* is produced by multiplying the corresponding *generic form* by a test function and integrating it over the domain ( $\Omega$ ) with respect to an infinitesimal area ( $dA$ ), or over the domain boundary ( $\partial\Omega$ ) with respect to an infinitesimal length along the boundary ( $ds$ ) (LeVeque 2005).

Linear system solvers in COMSOL Multiphysics™ are classified in two categories: direct or iterative. Three direct solvers were considered to solve for the system of linear equations: PARDISO, UMFPACK and SPOOLES; and three iterative solvers were taken into account: GMRES, FGMRES, BiCGStab. From the list of direct solvers, PARDISO was the obvious choice because it is more efficient than SPOOLES and often uses less memory than UMFPACK. The SPOOLES direct solver uses less memory than PARDISO, but is less numerically stable and slower. The available computer memory was sufficient to handle the cases being run in this research; hence, the only criterion was the computational speed for models with high degrees of freedom. Iterative solvers require less memory resources and have faster computing times for models with high degrees of freedom, but they are less stable and it is important to adjust the settings carefully in order to see any advantageous effects. Due to the fact that stability issues were the main obstacle when solving for the highly nonlinear problems in this research, the PARDISO direct solver (Schenk and Nguyen 2009), which uses some variant of Gaussian elimination, outweighed all other linear system solvers.

The solution process for the system of linear equations ( $Ax = b$ ), consists of six distinct steps:

1. Starting solver: Control parameters are setup.

2. Assembling sparsity pattern: The solver performs an unsymmetrical permutation:  $A_1 = D_r P_r A D_c$ , where  $P_r$  is a row permutation matrix that maximizes the magnitude of the diagonal entries, and the terms  $D_r$  and  $D_c$  are diagonal scaling matrices that scale the matrix so the diagonals entries are equal to one and off-diagonals entries are less than or equal to one (Schenk and Gärtner 2004).
3. Assembling matrices: The solver uses the Nested dissection ordering technique to find a symmetric permutation  $P_{fill}$  to preserve sparsity ( $A_2 = P_{fill} A_1 P_{fill}^T$ ), where  $P_{fill}$  is based on the structure  $P_r A_1 + P_r^T A_1^T$  (Schenk and Gärtner 2004).
4. Matrix factorization: Numerical factorization of the sparse matrix  $A_2 = Q_r L U Q_c$  that computes the lower ( $L$ ) and upper triangular matrix ( $U$ ), where  $Q_r$  and  $Q_c$  are diagonal block supernode pivoting permutations (Schenk et al. 1999).
5. Constraint handling: The solver uses an elimination constraint handling method to remove the Lagrange multiplier if the constraints ( $R_d = 0$ ) are linear and time independent, and if the constraint force Jacobian ( $(\partial R_d / \partial u)^T$ ) is constant.
6. Solving linear system: PARDISO solves for the system of linear equations  $Ax = b$ .

The convergence criterion in each iteration for all dependent variables was determined based on the weighted Euclidean norm:

$$err = \left( \frac{1}{N} \sum_{i=1}^N \left( \frac{|E_i|}{W_i} \right)^2 \right)^{1/2} \quad (\text{A.4})$$

where  $err$  is the relative error,  $N$  is the number of degrees of freedom,  $E_i$  is the estimated error in the solution vector during the time step, and  $W_i$  is defined as:

$$W_i = \max(|U_i|, S_i) \quad (\text{A.5})$$

where  $U_i$  is the true solution vector and  $S_i$  is the scaling factor. The solver can automatically assign values for the scaling factor based on the magnitudes of the Jacobian and mass matrices, but this option was not chosen because the dependent variables in the model have large differences in their magnitudes which might result in ill-conditioned matrices. To improve this situation, the scaling factor was set to the initial values of the variables because the initial values give a very accurate estimate of the scales of the variables. When dealing with highly nonlinear problems, convergence might be impossible with initial conditions that are inconsistent with the boundary conditions. In order to provide the most accurate initial conditions, the COMSOL Multiphysics™ software modifies the given initial values of all the degrees of freedom using the Backward-Euler method to guarantee consistency with the constraints of the system.

The maximum allowed relative error ( $err$ ) in each time step is specified by a user-defined relative tolerance, which was set at 0.001 for the simulations in this research. When this convergence criterion is satisfied, and all the dependent variables are initially solved, an implicit differential-algebraic (IDA) solver (Hindmarsh et al. 2005), which uses variable order backward differentiation formula (BDF), is applied for the time stepping method. BDF is a multistep formula that computes an approximation to a derivative variable ( $\dot{y} = dy/dt$ ) at time  $t_n$  using an interpolating polynomial whose order ranges from 1 to 5 (Hindmarsh et al. 2005):

$$\sum_{i=1}^q \alpha_{n,i} y_{n-i} = h_n \dot{y}_n \quad (\text{A.6})$$

In equation (A.6),  $q$  refers to the order of the polynomial,  $y_n$  and  $\dot{y}_n$  are the computed approximations at time  $t_n$ ,  $h_n$  represents the time step size  $t_n - t_{n-1}$ , and  $\alpha_{n,i}$  represents a coefficient which is determined by the order and the history of the step sizes. By applying the BDF formula (A.6) to the differential-algebraic system of equations, a nonlinear algebraic system that is to be solved at each time step is produced (Hindmarsh et al. 2005). The time steps were accepted if the following condition was satisfied:

$$\left( \frac{1}{N} \sum_i \left( \frac{|E_i|}{A_i + R_i |U_i|} \right)^2 \right)^{1/2} < 1 \quad (\text{A.7})$$

where  $A_i$  is the absolute tolerance for DOF  $i$  and  $R_i$  is the relative tolerance. If this condition (A.7) is not satisfied, a new smaller time step is chosen by the solver. The absolute and relative tolerances were set at 0.0001 and 0.001, respectively. These tolerance parameters were important in the determination of the time steps. For this reason, the accuracy of the model was checked by performing a mesh analysis, as was shown in the Appendix C, and by making sure that the algebraic equations (*i.e.*, electrical-neutrality and solubility relations) displayed no significant errors over time during the solution. Based on this assessment and the magnitude of these tolerance values, the concentration of each variable would be accurate to three decimal places at each time step. The time stepping algorithm was able to take small time steps to resolve the transient effects (addition of chlorides or changing the current density), and it was also able to increase time steps by a factor of two or less at stable conditions.

## Appendix B: Model Implementation in COMSOL™

The steps taken to implement a typical boundary-value problem defined in Chapter 3 in COMSOL™ are presented in this Appendix. To correctly define the governing equations in COMSOL™, adjustments needed to be made to the form of the extended Nernst-Planck equation and the modified Davies equation. The adjusted forms of the extended Nernst-Planck equation (B.1) and modified Davies equation (B.2) are as follows:

$$\frac{\partial c_{is}}{\partial t} + \frac{\partial c_i}{\partial t} + \nabla \cdot \left( \underbrace{-D_i \nabla c_i}_{\text{Diffusion}} - \underbrace{\frac{D_i z_i F}{RT} c_i \nabla \phi}_{\text{Electrical coupling}} - \underbrace{D_i c_i (\nabla \gamma_i / \gamma_i)}_{\text{chemical activity effects}} \right) = 0 \quad (\text{B.1})$$

$$\gamma_i = \exp \left( -\frac{Az_i^2 \sqrt{I}}{1 + a_i B \sqrt{I}} + \frac{(0.2 - 4.17 \times 10^{-5} I) Az_i^2 I}{\sqrt{1000}} \right) \quad (\text{B.2})$$

In addition, to prevent oxygen within the domain to become negative (due to the consumption of oxygen on the cathodic surfaces), a Heaviside function was introduced to smooth the oxygen concentration near zero. The applied Heaviside function was equal to 1 when the oxygen concentration was positive and smoothes the transition to 0 within the interval  $-0.001 < c_{O_2} < 0.001$  when the oxygen concentration becomes zero (or negative). This smoothing function was applied to the Neumann boundary conditions for oxygen (equation B.3) and for hydroxide (equation B.4) on the surface of the steel because there will be no hydroxide production when there is no oxygen present in the pore solution:

$$\mathbf{n} \cdot \mathbf{N}_{O_2} = -\left(\frac{i_p}{4F}\right) * flch_s(c_{O_2}, 0.001) \quad (\text{B.3})$$

$$\mathbf{n} \cdot \mathbf{N}_{\text{OH}^-} = \left(\frac{i_p}{F}\right) * \text{flc1hs}(c_{\text{O}_2}, 0.001) \quad (\text{B.4})$$

A step-by-step procedure of the model described in Chapter 4.3 for CH solution no.3 in Table 3.2 is provided in this Appendix. The steps taken to implement this model into COMSOL Multiphysics™ were very similar to the solution procedure found in the Model Library chapter of the Comsol Multiphysics™ manual. For this reason, a similar outline, solution process and typographical convention were applied. The typographical conventions that appear in the solution procedure below are the following:

- Words in “quotations” indicate keyboard entries in the user interface
- Words in **boldface** font indicate that the given words appear exactly the same on the user interface
- The symbol > indicates a menu item

## MODEL NAVIGATOR

- 1 In the **Model Navigator**, select **2D** in the **Space dimension** list.
- 2 In the **COMSOL Multiphysics > PDE Modes** folder, select **PDE General Form**.  
Make sure **Lagrange – Quadratic** is selected in the **Elements** list.
- 3 Click the **Multiphysics** button.
- 4 Before adding each application mode, name it and its dependent variable according to the following table:

<b>Application mode name</b>	<b>Dependent variable</b>
potential	phi
ionic	c1 c2 c3 c4 c5 c6
solid	c7 c8
activity	gam1 gam2 gam3 gam4 gam5

Type the name of the application mode and the dependent variable in the **Application mode name** and **Dependent variables** edit fields, respectively.

- 5 Click **Add** to add each of the application modes to the model.
- 6 When you have added the four application modes, click **OK** to exit the **Model Navigator** and continue modelling

## OPTIONS AND SETTINGS

- 1 From the **Options** menu, choose **Axes/Grid Settings**.
- 2 Enter grid spacings from the table below. To enter the grid spacings, first click the **Grid** tab and click to clear the **Auto** check box.

<b>Grid</b>	
<b>x spacing</b>	1e-5
<b>Extra x</b>	-1e-6
<b>y spacing</b>	1e-5
<b>Extra y</b>	5e-8 5e-4

3 Click **OK**.

4 Define the following constants in the **Options > Constants** dialog box:

Name	Expression	Description
D1	5.28e-9	m <sup>2</sup> /s
D2	0.719e-9	m <sup>2</sup> /s
D3	0.792e-9	m <sup>2</sup> /s
D4	2.03e-9	m <sup>2</sup> /s
D5	1.33e-9	m <sup>2</sup> /s
D6	2.2e-9	m <sup>2</sup> /s
z1	-1	-
z2	2	-
z3	2	-
z4	-1	-
z5	1	-
z6	0	-
F	96488	C/mol
R	8.3143	J/mol/K
T	298	K
epsilon	7.092e-10	C <sup>2</sup> /N/m <sup>2</sup>
n1	1	-
n2	2	-
n6	4	-
c1o	31.311	mol/m <sup>3</sup>
c2o	1.39e-10	mol/m <sup>3</sup>
c3o	15.656	mol/m <sup>3</sup>
c4o	0	mol/m <sup>3</sup>
c5o	0	mol/m <sup>3</sup>
c6o	0.15	mol/m <sup>3</sup>
c7o	0	mol/m <sup>3</sup>
c8o	0	mol/m <sup>3</sup>
K1	5500	mol <sup>3</sup> /m <sup>9</sup>
K2	4.87e-8	mol <sup>3</sup> /m <sup>9</sup>
ip	0.001	A/m <sup>2</sup>
a1	3.5e-10	m
a2	6e-10	m
a3	6e-10	m
a4	3e-10	m
a5	4e-10	m

5 Click **OK**.

**6 Define the following expressions in the Options > Expressions > Scalar Expressions**

dialog box:

<b>Name</b>	<b>Expression</b>
ox	flc1hs(c6,0.001)
N1x	$-D1(c8)*c1x-z1*F*(D1(c8)/R/T)*c1*phix-D1(c8)*c1*(gam1x/gam1)$
N1y	$-D1(c8)*c1y-z1*F*(D1(c8)/R/T)*c1*phiy-D1(c8)*c1*(gam1y/gam1)$
N2x	$-D2(c8)*c2x-z2*F*(D2(c8)/R/T)*c2*phix-D2(c8)*c2*(gam2x/gam2)$
N2y	$-D2(c8)*c2y-z2*F*(D2(c8)/R/T)*c2*phiy-D2(c8)*c2*(gam2y/gam2)$
N3x	$-D3(c8)*c3x-z3*F*(D3(c8)/R/T)*c3*phix-D3(c8)*c3*(gam3x/gam3)$
N3y	$-D3(c8)*c3y-z3*F*(D3(c8)/R/T)*c3*phiy-D3(c8)*c3*(gam3y/gam3)$
N4x	$-D4(c8)*c4x-z4*F*(D4(c8)/R/T)*c4*phix-D4(c8)*c4*(gam4x/gam4)$
N4y	$-D4(c8)*c4y-z4*F*(D4(c8)/R/T)*c4*phiy-D4(c8)*c4*(gam4y/gam4)$
N5x	$-D5(c8)*c5x-z5*F*(D5(c8)/R/T)*c5*phix-D5(c8)*c5*(gam5x/gam5)$
N5y	$-D5(c8)*c5y-z5*F*(D5(c8)/R/T)*c5*phiy-D5(c8)*c5*(gam5y/gam5)$
N6x	$-D6(c8)*c6x$
N6y	$-D6(c8)*c6y$
I	$abs(0.5*(z1^2*c1+z2^2*c2+z3^2*c3+z4^4*c4+z5^2*c5))$
A	$(sqrt(2)*F^2*1.602e-19)/(8*pi*(epsilon*R*T)^1.5)$
B	$sqrt(2*F^2/epsilon/R/T)$
G1	$((-A*z1^2*sqrt(I))/(1+a1*B*sqrt(I)))+((0.2-4.17e-5*I)*A*z1^2*I/sqrt(1000))$
G2	$((-A*z2^2*sqrt(I))/(1+a2*B*sqrt(I)))+((0.2-4.17e-5*I)*A*z2^2*I/sqrt(1000))$
G3	$((-A*z3^2*sqrt(I))/(1+a3*B*sqrt(I)))+((0.2-4.17e-5*I)*A*z3^2*I/sqrt(1000))$
G4	$((-A*z4^2*sqrt(I))/(1+a4*B*sqrt(I)))+((0.2-4.17e-5*I)*A*z4^2*I/sqrt(1000))$
G5	$((-A*z5^2*sqrt(I))/(1+a5*B*sqrt(I)))+((0.2-4.17e-5*I)*A*z5^2*I/sqrt(1000))$

**7 Click OK.**

**8 From the Options menu, choose Functions.**

**9 In the Functions dialog box, click the New button.**

**10 In the New Function dialog box, type “ip” in the Function name edit field, and click on Interpolation, then click OK.**

**11 In the Functions dialog box, change the Interpolation method to Linear and the Extrapolation method to Constant, then fill in the table according to the following table:**

Function name	ip	
	$c_{Cl^-}/c_{OH^-}$	$f(c_{Cl^-}/c_{OH^-})$
	3	0.001
	5	0.017

12 Click **Apply**

13 Repeat steps 9 to 12 for D1 to D6 according to the following table:

D1-D6	D1	D2	D3	D4	D5	D6
c8	f(c8)	f(c8)	f(c8)	f(c8)	f(c8)	f(c8)
0	$5.28 \times 10^{-9}$	$0.72 \times 10^{-9}$	$0.79 \times 10^{-9}$	$2.03 \times 10^{-9}$	$1.33 \times 10^{-9}$	$2.2 \times 10^{-9}$
37840	$5.28 \times 10^{-13}$	$0.72 \times 10^{-13}$	$0.79 \times 10^{-13}$	$2.03 \times 10^{-13}$	$1.33 \times 10^{-13}$	$2.2 \times 10^{-13}$

14 Repeat steps 9 to 12 for c1o to c5o according to the following table:

Function name	c1o-c5o	c1o	c2o	c3o	c4o	c5o
	t	f(t)	f(t)	f(t)	f(t)	f(t)
	0	31.311	$1.39 \times 10^{-10}$	15.656	0	0
	3600	35.773	$1.58 \times 10^{-10}$	17.887	100	100

15 Click **OK**

## GEOMETRY MODELLING

1 From the **Draw** menu, choose **Specify Objects > Line**

2 In the **Line** dialog box, apply the following coordinates:

Coordinates							
x	$-1 \times 10^{-6}$	$-1 \times 10^{-6}$	0	0	$5 \times 10^{-5}$	$5 \times 10^{-5}$	$-1 \times 10^{-6}$
y	0	$5 \times 10^{-4}$	$5 \times 10^{-4}$	$5 \times 10^{-8}$	$5 \times 10^{-8}$	0	0

3 In the **Style** menu, choose **Closed polyline (solid)** to create a solid object that the software labels **CO1**

4 Click **OK**.

- 5 From the **Options** menu, choose **Zoom > Zoom Extends** to show the full geometry
- 6 From the **Options** menu, choose **Zoom > Zoom Window**. In the drawing area, use the mouse to define a small zoom window at the bottom left corner of the geometry. This will adjust the coordinate system to focus on the corner of the geometry in the work area.
- 7 From the **Draw** menu, choose **Draw Objects > Line**
- 8 In the drawing area, create the first line by clicking the (x, y) coordinates (0, 5e-8) and then (-1e-6, 5e-8), then click the right mouse button.

## PHYSICS SETTINGS

### *Subdomain Settings – PDE, General Form (potential)*

- 1 Select **PDE, General Form (potential)** from the **Multiphysics** menu
- 2 From the **Physics** menu, choose **Subdomain settings**
- 3 In the **Subdomain Settings** dialog box, select subdomains **1** and **2**
- 4 Click on the **Coefficients** tab
- 5 Enter “[ $-\phi_{ix}$   $-\phi_{iy}$ ]” in the **Flux vector** edit field, “ $(F/\epsilon)*(-c_1+2*c_2+2*c_3-c_4+c_5)$ ” in the **Source term** edit field, “0” in the **Mass coefficient** edit field, and “0” in the **Damping/Mass coefficient** edit field.
- 6 Click the **Init** tab
- 7 Enter “0” for  $\phi(t_0)$  and  $\phi_{it}(t_0)$
- 8 Click **OK**.

***Boundary Conditions - PDE, General Form (potential)***

- 1 Open the **Boundary settings** dialog box from the **Physics** menu
- 2 Click on the **Coefficients** tab
- 3 In the **Boundary Settings** dialog box, select boundaries **1-3, 5-7** and then select **Neumann boundary condition** in the **Boundary conditions** area. Make sure boundary **4** is highlighted in grey (inactive boundary).
- 4 Enter “0” for the coefficient **G**
- 5 Select boundary **8** and then select **Dirichlet boundary condition** in the **Boundary conditions** area.
- 6 Enter “0” for the coefficient **G** and “-phi” for the coefficient **R**.
- 7 Click **OK**.

***Subdomain Settings – PDE, General Form (ionic)***

- 1 Select **PDE, General Form (ionic)** from the **Multiphysics** menu
- 2 From the **Physics** menu, choose **Subdomain settings**
- 3 In the **Subdomain Settings** dialog box, select subdomains **1** and **2**
- 4 Click on the respective tab and enter the expressions below:

<b>Tab</b>	$\Gamma$	<b>F</b>	$\mathbf{e}_a$	$\mathbf{d}_a$
	[ N1x N1y ]	-c7t	[ 0 0 0 0 0 0 ]	[ 1 0 0 0 0 0 ]
	[ N2x N2y ]	-c8t	[ 0 0 0 0 0 0 ]	[ 0 1 0 0 0 0 ]
	[ N3x N3y ]	0	[ 0 0 0 0 0 0 ]	[ 0 0 1 0 0 0 ]
	[ N4x N4y ]	0	[ 0 0 0 0 0 0 ]	[ 0 0 0 1 0 0 ]
	[ N5x N5y ]	0	[ 0 0 0 0 0 0 ]	[ 0 0 0 0 1 0 ]
	[ N6x N6y ]	0	[ 0 0 0 0 0 0 ]	[ 0 0 0 0 0 1 ]

5 Click on the **Init** tab and enter the expressions below:

Variable	Initial value
$c1(t_0)$	$c1_0$
$c2(t_0)$	$c2_0$
$c3(t_0)$	$c3_0$
$c4(t_0)$	$c4_0$
$c5(t_0)$	$c5_0$
$c6(t_0)$	$c6_0$

The remaining components will be zero

6 Click **OK**.

### *Boundary Conditions - PDE, General Form (ionic)*

1 Open the **Boundary settings** dialog box from the **Physics** menu

2 In the **Boundary Settings** dialog box enter the following boundary conditions with respect to their boundaries:

Boundary	1, 3	2	5 - 7	8
<b>Type</b>	<b>Neumann boundary condition</b>	<b>Neumann boundary condition</b>	<b>Neumann boundary condition</b>	<b>Dirichlet boundary condition</b>
<b>G</b>	[ (ip(c4/c1)/n1/F)*ox (ip(c4/c1)/n2/F) 0 0 0 (-ip(c4/c1)/n6/F)*ox ]	[ 0 0 0 0 0 ]	[ (ip/n1/F)*ox (ip/n2/F) 0 0 0 (-ip/n6/F)*ox ]	[ 0 0 0 0 0 ]
<b>R</b>	-	-	-	[-c1+c1o(t) -c2+c2o(t) -c3+c3o(t) -c4+c4o(t) -c5+c5o(t) -c6+c6o]

Make sure boundary 4 is highlighted in grey (inactive boundary).

3 Click **OK**.

***Subdomain Settings – PDE, General Form (solid)***

- 1 Select **PDE, General Form (solid)** from the **Multiphysics** menu
- 2 From the **Physics** menu, choose **Subdomain settings**
- 3 In the **Subdomain Settings** dialog box, select subdomains **1** and **2**
- 4 Click on the respective tab and enter the expressions below:

<b>Tab</b>	$\Gamma$	<b>F</b>	$e_a$	$d_a$
	[ 0 0 ]	$0.5*c7-c8$	[ 0 0 ]	[ 0 0 ]
	[ 0 0 ]	$K2/(gam2*c2)-(gam1*c1)^2$	[ 0 0 ]	[ 0 0 ]

- 5 Click on the **Init** tab and enter the expressions below:

<b>Variable</b>	<b>Initial value</b>
$c7(t_0)$	$c7_0$
$c8(t_0)$	$c8_0$

The remaining components will be zero

- 6 Click **OK**.

***Boundary Conditions - PDE, General Form (solid)***

- 1 Open the **Boundary settings** dialog box from the **Physics** menu
- 2 Click on the **Type** tab.
- 3 In the **Boundary Settings** dialog box, select boundaries **1-3, 5-7** and then select **Neumann boundary condition** in the **Boundary condition type** area. Make sure boundary **4** is highlighted in grey (inactive boundary).
- 4 Click on the **G** tab.
- 5 Enter “0” for all spaces in the **G coefficient** area
- 6 Click on the **Type** tab

7 Select boundary **8** and then select **Dirichlet boundary condition** in the **Boundary condition type** area.

8 Enter “-c7+c7o” for the top space and “-c8+c8o” for the bottom space in the **R coefficient** area.

9 Click **OK**.

***Subdomain Settings – PDE, General Form (activity)***

1 Select **PDE, General Form (activity)** from the **Multiphysics** menu

2 From the **Physics** menu, choose **Subdomain settings**

3 In the **Subdomain Settings** dialog box, select subdomains **1** and **2**

4 Click on the respective tab and enter the expressions below:

<b>Tab</b>	$\Gamma$	<b>F</b>	$\mathbf{e}_a$	$\mathbf{d}_a$
	[ 0 0 ]	-gam1+exp(G1)	[ 0 0 0 0 0 ]	[ 0 0 0 0 0 ]
	[ 0 0 ]	-gam2+exp(G2)	[ 0 0 0 0 0 ]	[ 0 0 0 0 0 ]
	[ 0 0 ]	-gam3+exp(G3)	[ 0 0 0 0 0 ]	[ 0 0 0 0 0 ]
	[ 0 0 ]	-gam4+exp(G4)	[ 0 0 0 0 0 ]	[ 0 0 0 0 0 ]
	[ 0 0 ]	-gam5+exp(G5)	[ 0 0 0 0 0 ]	[ 0 0 0 0 0 ]

5 Click on the **Init** tab and enter the expressions below:

<b>Variable</b>	<b>Initial value</b>
<b>gam1(t<sub>0</sub>)</b>	0.8291
<b>gam2(t<sub>0</sub>)</b>	0.5212
<b>gam3(t<sub>0</sub>)</b>	0.5212
<b>gam4(t<sub>0</sub>)</b>	0.8243
<b>gam5(t<sub>0</sub>)</b>	0.8336

The remaining components will be zero

6 Click **OK**.

***Boundary Conditions - PDE, General Form (activity)***

- 1** Open the **Boundary settings** dialog box from the **Physics** menu
- 2** Click on the **Type** tab.
- 3** In the **Boundary Settings** dialog box, select boundaries **1-3, 5-8** and then select **Neumann boundary condition** in the **Boundary condition type** area. Make sure boundary **4** is highlighted in grey (inactive boundary).
- 4** Click on the **G** tab.
- 5** Enter “0” for all spaces in the **G coefficient** area
- 6** Click **OK**.

**MESH GENERATION**

- 1** From the **Mesh** menu, choose **Free Mesh Parameters**
- 2** In the **Free Mesh Parameters** dialog box, set **Element growth rate** to “1.1” and the **Resolution of narrow regions** to “3”. These changes will set the maximum rate at which the element size can grow to 10 % and controls the number of layers of elements in narrow regions to 3.
- 3** Click **OK**.
- 4** From the **Mesh** menu, choose **Initialize Mesh**.

**COMPUTING THE SOLUTION**

- 1** Go to the **Solve** menu and select **Solver Manager**.
- 2** In the **Solver Manager** dialog box, click the **Initial Value** tab. Make sure that **Initial value expression** and **Use setting from Initial value frame** are selected.

- 3 Click **OK**.
- 4 Go to the **Solve** menu and select **Solver Parameters**.
- 5 In the **Solver Parameters** dialog box, click the **General tab**.
- 6 In the **Solver** menu, choose **Time dependent**
- 7 In the **Time stepping** area, type “range(0,100,1e9)” in the **Times** edit field. Make sure a **Relative tolerance** of “0.001” and an **Absolute tolerance** of “0.0001” is entered.
- 8 In the **Linear system solver** list, select **Direct(PARDISO)**.
- 9 Click the **Time Stepping** tab.
- 10 In **Times to store in output** list, select **Time steps from solver**.
- 11 In the **Initial time step** menu, click to clear the **Auto** check box and input a value of “0.001.”
- 12 Click on the **Advanced** tab.
- 13 In the **Type of scaling** list, select **Initial value based**.
- 14 Click **OK**.
- 15 From the **Solve** menu, choose **Solve Problem** to start the simulation.

## Appendix C: Mesh Analysis

This Appendix presents the procedure taken to determine the finite element mesh that was used in the simulations carried out in this thesis. Based on the type of finite element selected, the COMSOL Multiphysics™ software can generate a mesh automatically; however, it was important to choose the proper element type and size because the accuracy and the efficiency of the solution were directly influenced by these factors. To determine which mesh was more computationally efficient for a given domain, mesh analysis was performed with and without chemical activity effects, due to the higher computational requirements of the models when activity effects were included.

### ***C.1 Simulations with chemical activity effects included***

The analysis presented in this section was carried out on a domain with the following dimensions: mill scale crack length ( $l$ ) =  $5 \times 10^{-5}$  m; mill scale crack thickness ( $t_l/2$ ) =  $5 \times 10^{-7}$  m; crevice length ( $c/2$ ) =  $2.5 \times 10^{-4}$  m; crevice thickness ( $t_c$ ) =  $1 \times 10^{-6}$  m. The simulations were carried out in the CH solution; the chloride concentration in the bulk CH solution was  $500 \text{ mol/m}^3$ . Initial activities in the CH solution (solution no. 1) are given in Table 3.2. A constant passive current density,  $i_p$ , of  $10^{-2} \text{ A/m}^2$  was applied on steel and mill scale surfaces. Diffusion coefficients of species were assumed to linearly decrease from  $D_{max}$  to  $D_{min}$ , as per Table 3.4. All these parameters were chosen to obtain large variances in the concentration of the species between the bulk pore solution and the

pore solution at the tip of the crevice, while keeping the model within the computational power of the available computer.

The model analyzed in this section was discretized using either Lagrange quadratic triangular elements or Lagrange quadratic square elements, which use second order interpolation functions. When triangular elements were used, the mesh analysis began with 3 layers of elements across the crevice and mill scale crack lengths. After solving this model, the mesh was refined with 4 layers of elements, and then refined again with 6 layers across the crevice and mill scale crack lengths. The purpose of this mesh analysis was to increase the accuracy through mesh refinement in order to see if the solution was converging to stable non-oscillating concentrations. The mesh analysis also consisted of a single square element case with 3 layers of elements across the mill scale crack and 6 layers of elements across the crevice length. Only one mesh case was considered using square elements because finer elements would increase the computational requirements above the limits of the available computer and coarser elements would not yield accurate results. Three layers of elements were the minimum requirement for each mesh case because the two outside layers would be required to represent the boundary conditions, while another layer in the middle was needed to model the internal domain. The characteristics of each mesh case analyzed in this section were shown in Table C.1.

The mesh comparison presented in Table C.1 indicates that the gain in accuracy from mesh refinement results in increased computational times, which was a major factor in determining which mesh case should be used for the simulations in this research. The

computing time of the system was directly influenced by the number of degrees of freedom (dof). In particular, a critical threshold was found at around 600,000 dof after which an increase in the number of dof significantly increased the computing time required to solve the model by a factor of  $\sim 10$ .

**Table C.1:** Comparison of finite element meshes when activity effects were included.

Mesh case	Finite element	Element layers	CPU time (sec) <sup>(b)</sup>	Minimum element quality <sup>(c)</sup>	Matrix description (# dof, # elements)
1	Square	3, 6 <sup>(a)</sup>	169730	1.0000	(606074, 9918)
2	Triangular	3	1917	0.8284	(148974, 4562)
3	Triangular	4	2493	0.8724	(254772, 8089)
4	Triangular	6	13018	0.8284	(553406, 18248)

<sup>(a)</sup> 3 layers of elements across the mill scale crack and 6 layers of elements across the crevice length

<sup>(b)</sup> Computer specifications: Dell Precision PWS690, Intel(R) Xeon(R) CPU, 5150 @ 2.66 GHz, 4.0 GB of RAM

<sup>(c)</sup> Mesh quality was provided by the mesh generator of COMSOL Multiphysics™

Triangular elements were more computationally efficient than square elements because they are able to increase in size with an increase in domain size, while square elements must remain the same size throughout in order to maintain the mesh quality. COMSOL Multiphysics™ computes the mesh quality ( $q$ ) for triangular and square elements using equations (C.1) and (C.2), respectively.

$$q = \frac{4\sqrt{3}A_e}{h_1^2 + h_2^2 + h_3^2} \quad (\text{C.1})$$

$$q = \frac{4A_e}{h_1^2 + h_2^2 + h_3^2 + h_4^2} \quad (\text{C.2})$$

where  $A_e$  is the area of the element and  $h_i$  represents the side lengths of the element. The mesh quality ranges from 0 (low mesh quality) to 1 (high mesh quality). A mesh quality that is greater than 0.3 should not affect the quality of the solution; however, to be conservative, all meshes tested in this study had a mesh quality of 0.8 or higher.

The concentration of each species was analyzed at steady-state conditions (*i.e.*, at  $t = 10^9$  s) along the mill scale crack (boundary 2) and steel surface (boundary 3) for all four mesh cases shown in Table C.1, and are shown in Figures C.1 and C.2. Examination of these figures shows that the largest differences among different mesh cases occurred at the tip of the crevice (point A); hence, a more detailed comparison was also prepared at this point, as presented in Table C.2. As shown in Figures C.1 and C.2, the solution did not change substantially from one mesh case to another when the mesh was refined. In fact, the concentration of each species in Table C.2 were compared by taking the maximum and minimum values produced by the four mesh cases at the tip of the crevice (point A) and finding the percent difference between these two values; the largest percent difference was found to be only 3.35% for the  $\text{Fe}^{2+}$  species. Therefore, it was concluded that, the mesh case 2 (*i.e.*, 3 layers of triangular elements) provided accurate solutions with the highest computational efficiency.

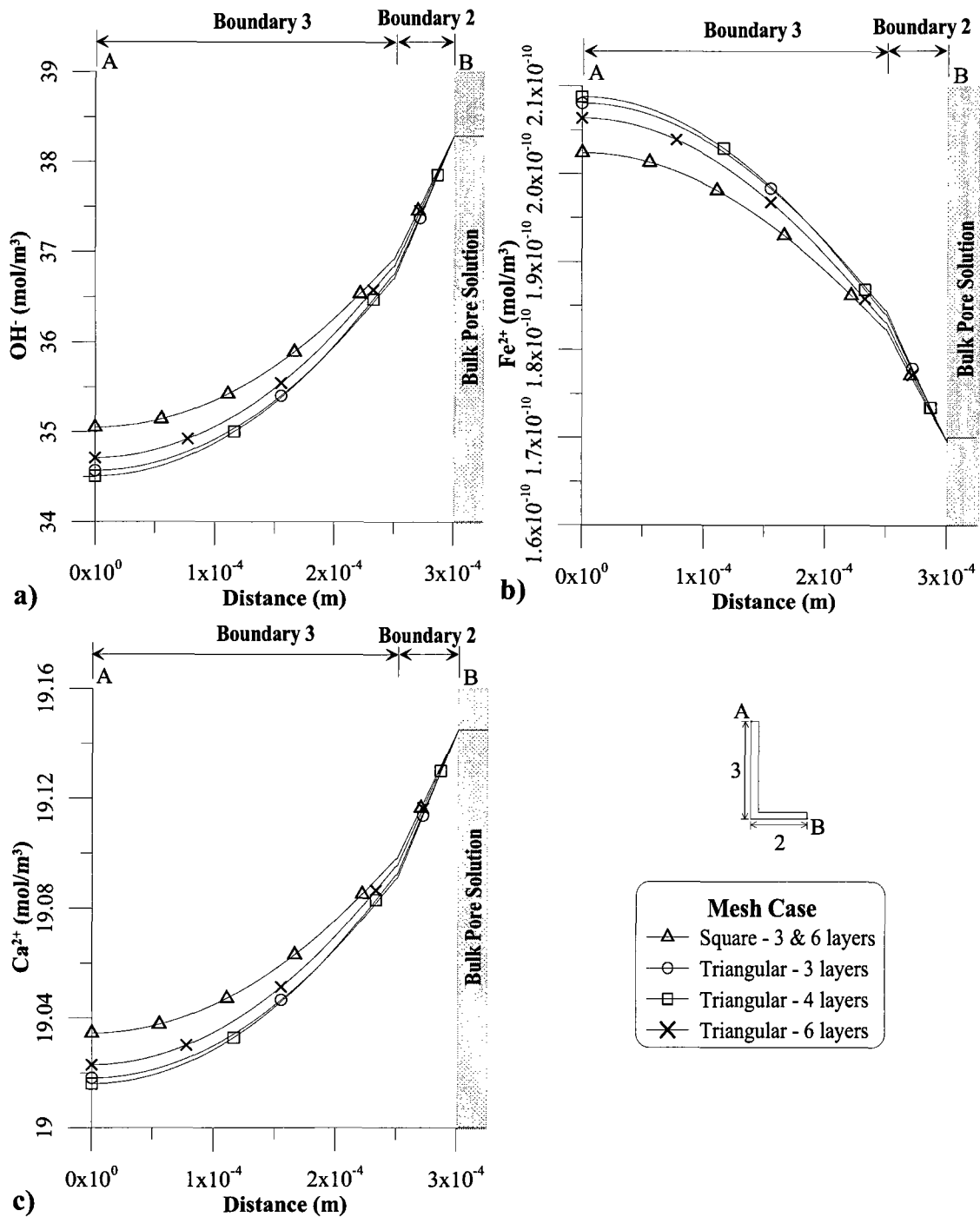


**Figure C.1.** Mesh comparison of four different mesh types along the center of the mill scale crack (boundary 2) and along the steel surface (boundary 3) when steady-state conditions are reached for: (a)  $\text{OH}^-$  (b)  $\text{Fe}^{2+}$  (c)  $\text{Ca}^{2+}$ . Chemical activity effects were included. For clarity, only some of the data points are shown in the plots.

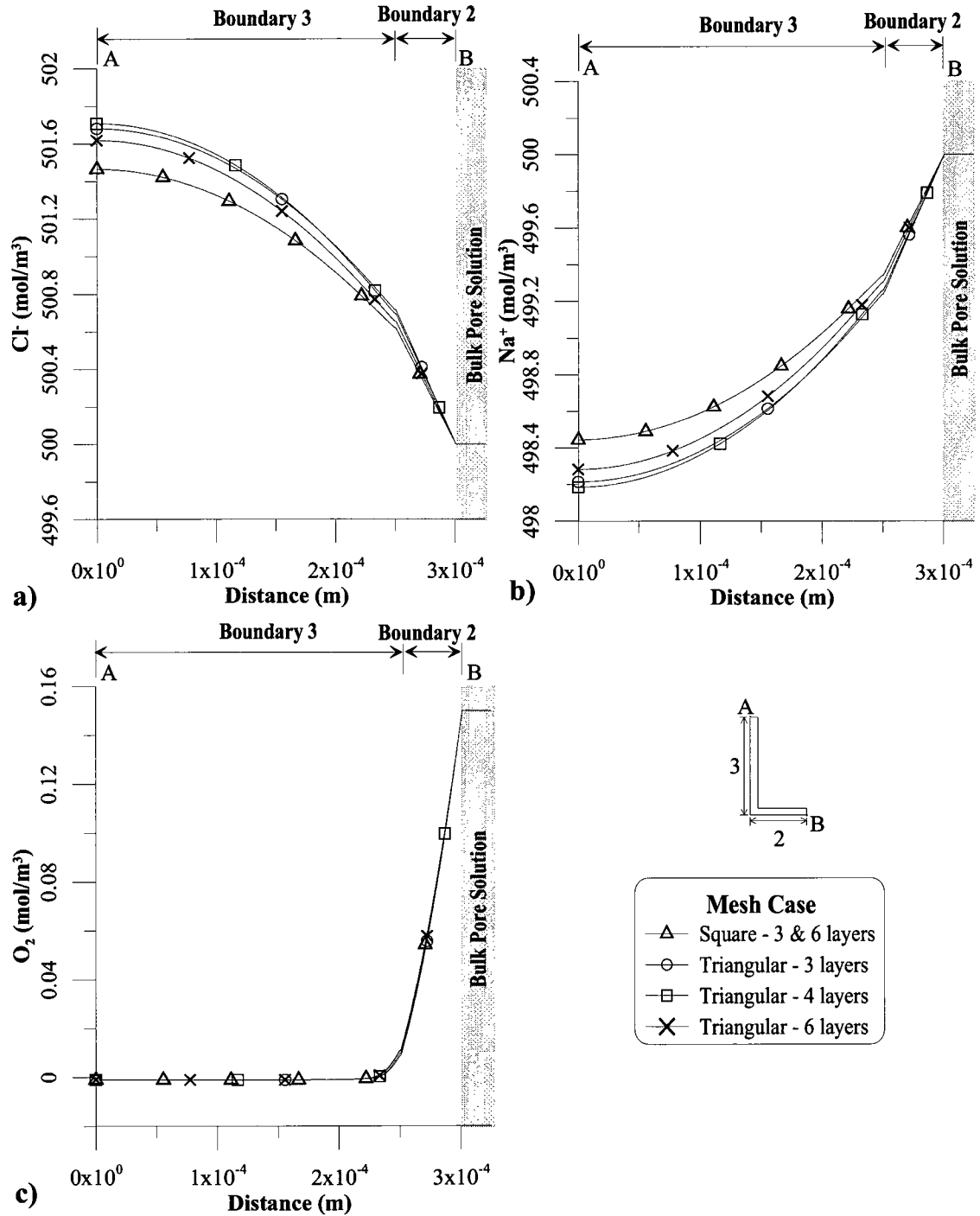


**Figure C.2.** Mesh comparison of four different mesh types along the center of the mill scale crack (boundary 2) and along the steel surface (boundary 3) when steady-state conditions are reached for: (a)  $\text{Cl}^-$  (b)  $\text{Na}^+$  (c)  $\text{O}_2$ . Chemical activity effects were included. For clarity, only some of the data points are shown in the plots.

**Table C.2:** Concentrations at the tip of the crevice when activity effects were included.

mol/m <sup>3</sup>	Mesh case <sup>(a)</sup>				% Difference <sup>(b)</sup>
	1	2	3	4	
$c_{OH^-}$	35.047	34.568	34.507	34.709	1.54
$c_{Fe^{2+}}$	$2.02 \times 10^{-10}$	$2.08 \times 10^{-10}$	$2.09 \times 10^{-10}$	$2.06 \times 10^{-10}$	3.35
$c_{Ca^{2+}}$	19.034	19.018	19.016	19.023	0.09
$c_{Cl^-}$	501.465	501.682	501.709	501.618	0.05
$c_{Na^+}$	498.443	498.213	498.184	498.281	0.05
$c_{O_2}$	$-9.95 \times 10^{-4}$	$-9.95 \times 10^{-4}$	$-9.96 \times 10^{-4}$	$-9.95 \times 10^{-4}$	0.10

<sup>(a)</sup> See Table C.1 for details on the properties of each mesh case

<sup>(b)</sup> A comparison between the maximum and minimum concentrations produced by the four mesh cases was used to calculate for the percent difference

## **C.2 Simulations with chemical activity effects ignored**

It was important to verify that larger variances in the concentrations between the bulk pore solution (point B) and the tip of the crevice (point A) would not cause significant differences among different meshes. Furthermore, a more detailed comparison between the meshes with square elements and meshes with triangular elements were required. Therefore, additional simulations were carried out with chemical activity effects ignored (*i.e.*, chemical activity removed from equation (3.10)) to gain more computational flexibility: the crevice length ( $c/2$ ) of the domain was increased to  $4 \times 10^{-4}$  m for these simulations. The characteristics of each mesh case analyzed are shown in Table C.3.

The mesh comparison presented in Table C.3 indicates that an increase in the number of dof results in longer computing times: the new triangular mesh case with 8 layers of elements across the mill scale crack and crevice lengths produced the longest computing time of 77,083 s (*i.e.*,  $t = 21.4$  h).

**Table C.3:** Mesh comparison properties when activity effects were ignored.

Mesh case	Finite element	Element layers	CPU time (sec) <sup>(b)</sup>	Minimum element quality	Matrix description (# dof, # elements)
1	Square	3, 6 <sup>(a)</sup>	19494	1.0000	(599517, 15300)
2	Triangular	3	811	0.8957	(137025, 6530)
3	Triangular	4	2016	0.8816	(233316, 11523)
4	Triangular	6	3181	0.8957	(509121, 26120)
5	Triangular	8	77083	0.8816	(881451, 46092)

<sup>(a)</sup> 3 layers of elements across the mill scale crack and 6 layers of elements across the crevice length

<sup>(b)</sup> Computer specifications: Dell Precision PWS690, Intel(R) Xeon(R) CPU, 5150 @ 2.66 GHz, 4.0 GB of RAM

The concentration profile of each species was analyzed along the mill scale crack (boundary 2) and steel surface (boundary 3) when steady-state was reached (*i.e.*, at  $t = 10^9$  s) for all five mesh cases indicated in Table C.3, and are presented in Figures C.3 and C.4. These five mesh cases were also compared in Table C.4 at the tip of the crevice (point A) at which the largest differences for each mesh case were compared.

Figures C.3 and C.4 show that larger variances in the concentration of species from the bulk pore solution (point B) to the tip of the crevice (point A) did not cause significant differences among different mesh cases. In fact, an examination of the concentration of species at the tip of the crevice, as shown in Table C.4, showed a maximum percent difference of 15.79 % for the  $\text{Fe}^{2+}$  species, while the other species were below 10 %. It was expected that iron would be the least accurate of all the species because the numerical model was only accurate to three decimal places (based on tolerances presented in Appendix A); this inaccuracy in iron was not a concern. Figures C.3 and C.4

also confirm that the triangular element mesh with 6 layers was more accurate than the square element case, since the new 8-layer triangular element case moved closer to the triangular case with 6 layers. From the results of this second mesh analysis, mesh case 2 (*i.e.*, triangular mesh case with 3 layers of elements) remains the best choice because of its ability to produce the fastest solution times, while obtaining accurate concentrations.

**Table C.4:** Concentrations at the tip of the crevice when activity effects were ignored.

mol/m <sup>3</sup>	Mesh case <sup>(a)</sup>					% Difference <sup>(b)</sup>
	1	2	3	4	5	
$c_{OH^-}$	15.030	14.005	13.792	14.229	14.480	8.23
$c_{Fe^{2+}}$	$2.16 \times 10^{-10}$	$2.48 \times 10^{-10}$	$2.56 \times 10^{-10}$	$2.41 \times 10^{-10}$	$2.32 \times 10^{-10}$	15.79
$c_{Ca^{2+}}$	10.967	10.946	10.942	10.951	10.956	0.24
$c_{Cl^-}$	503.465	503.959	504.062	503.851	503.730	0.12
$c_{Na^+}$	496.559	496.072	495.971	496.178	496.298	0.12
$c_{O_2}$	$-9.98 \times 10^{-4}$	$-9.98 \times 10^{-4}$	$-9.98 \times 10^{-4}$	$-9.98 \times 10^{-4}$	$-9.98 \times 10^{-4}$	0.04

<sup>(a)</sup> See Table C.3 for details on the properties of each mesh case

<sup>(b)</sup> A comparison between the maximum and minimum concentrations produced by the five mesh cases were used to calculate for the percent difference

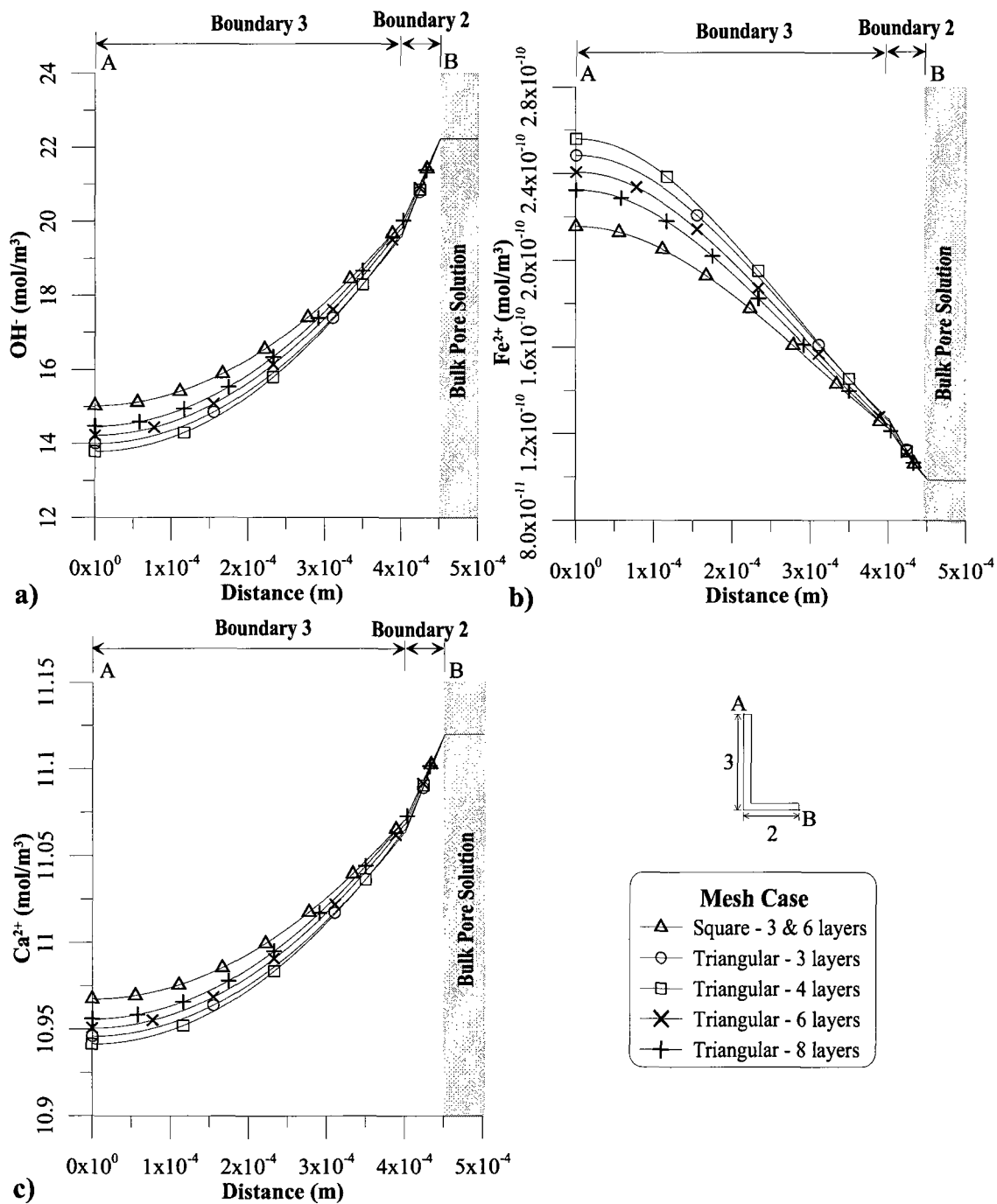


**Figure C.3.** Mesh comparison of five different mesh types along the center of the mill scale crack (boundary 2) and along the steel surface (boundary 3) when steady-state conditions are reached for: (a)  $\text{OH}^-$  (b)  $\text{Fe}^{2+}$  (c)  $\text{Ca}^{2+}$ . Activity effects were ignored. For clarity, only some of the data points are shown in the plots.

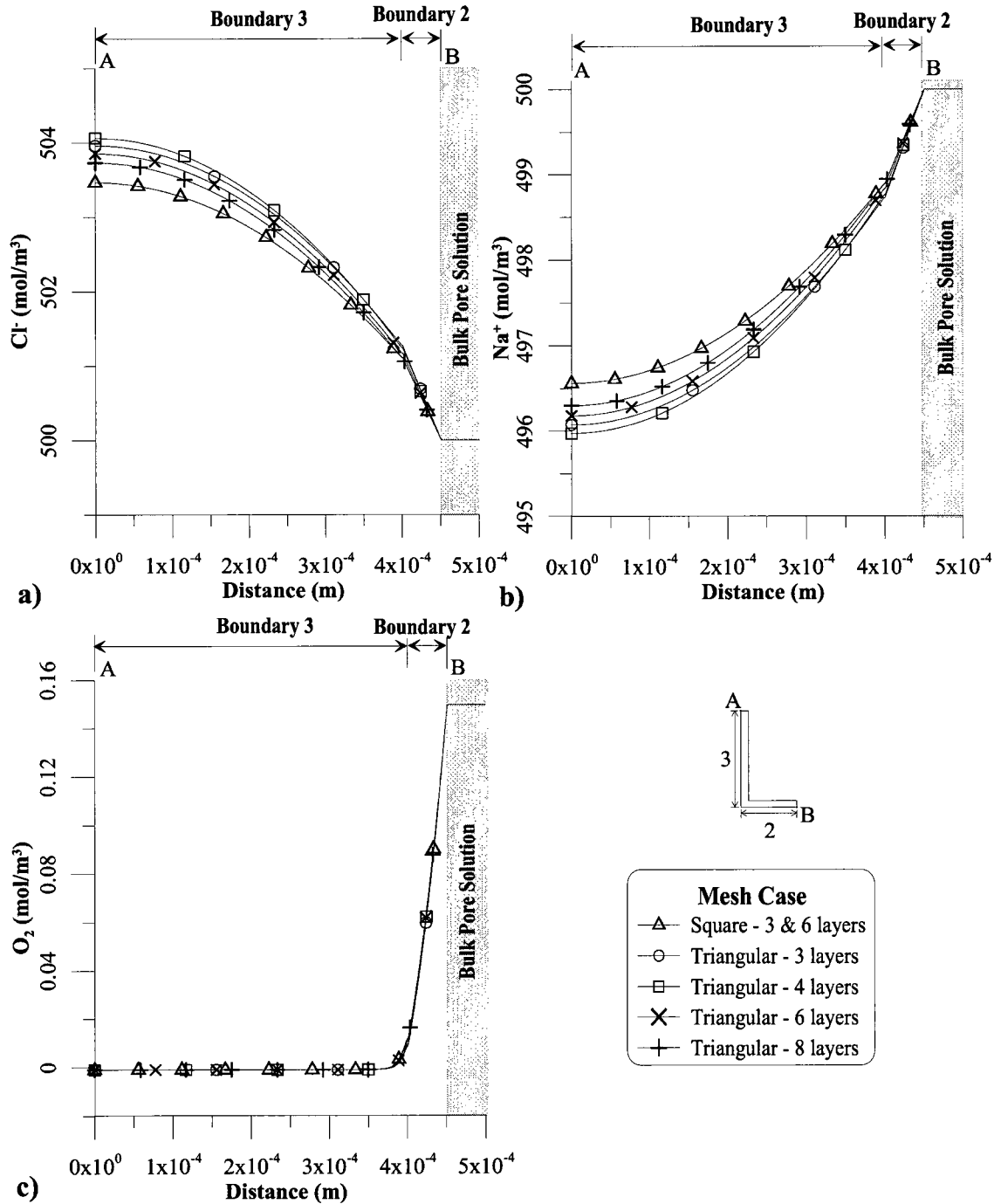


**Figure C.4.** Mesh comparison of five different mesh types along the center of the mill scale crack (boundary 2) and along the steel surface (boundary 3) when steady-state conditions are reached for: (a) Cl<sup>-</sup> (b) Na<sup>+</sup> (c) O<sub>2</sub>. Activity effects were ignored. For clarity, only some of the data points are shown in the plots.

When the hydroxide concentration in the pore solution approaches zero, the pH of the pore solution logarithmically decreases below 10. This sensitivity around the pH of 10 was the reason for another mesh analysis. The only adjustment made for these simulations was for the dimension of the crevice length ( $c/2$ ), which was increased to  $7 \times 10^{-4}$  m in order to reduce hydroxide concentrations as much as possible. Only two mesh cases were compared for this final case: the 3-layer triangular element case and the 6-layer triangular element case. From previous simulations, it was clear that the mesh with 3 layers of triangular elements was the most computationally efficient, while the mesh with 6 layers of triangular elements had potentially better accuracy. The characteristics of both mesh cases are shown in Table C.5, and the concentration profiles of the hydroxides along the mill scale crack (boundary 2) and steel surface (boundary 3) are illustrated in Figure C.5 at steady-state conditions (*i.e.*, at  $t = 10^9$  s).

**Table C.5:** Mesh comparison when activity effects were ignored.

Mesh case	Element layers	CPU time (sec) <sup>(a)</sup>	Minimum element quality	Matrix description (# dof, # elements)	$c_{OH^-}$ at tip of crevice (mol/m <sup>3</sup> )	pH at tip of crevice	% Difference
1	3	2805	0.8274	(217233, 10346)	0.238	10.377	4.09
2	6	49486	0.8274	(806913, 41384)	0.632	10.801	

<sup>(a)</sup>Computer specifications: Dell Precision PWS690, Intel(R) Xeon(R) CPU, 5150 @ 2.66 GHz, 4.0 GB of RAM

The hydroxide concentration profiles for both mesh cases shown in Figure C.5 were nearly equivalent to each other. Furthermore, the pH values at the tip of the crevice (point A), as shown in Table C.5, only showed a 4.09 % difference between the two mesh cases.

These results reinforce the fact that the triangular element case with 3 layers of elements was accurate even at low hydroxide concentrations (*i.e.*,  $[\text{OH}^-]$  near  $0 \text{ mol/m}^3$ ) for which small changes in the hydroxides cause significant drops in pH due to its logarithmic nature.

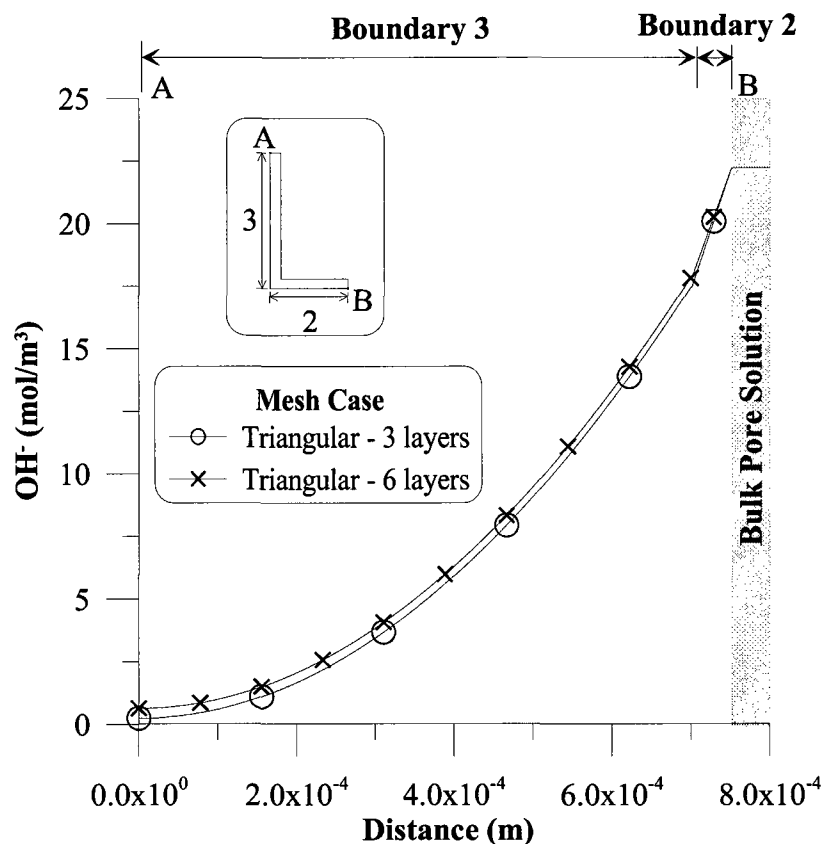


**Figure C.5.** Mesh comparison of two different mesh types along the center of the mill scale crack (boundary 2) and along the steel surface (boundary 3) when steady-state conditions are reached for  $\text{OH}^-$  species and activity effects were ignored. For clarity, only some of the data points are shown in the plots.

### C.3 Concluding remarks

The 3-layer triangular elements across the mill scale crack and crevice lengths were chosen as the mesh for all simulations carried out in this thesis because it was the most computationally efficient case. The concentrations were found to be accurate, even for

large changes from the bulk pore solution to the tip of the crevice, and the computational times were faster than those of all other mesh cases considered. Figure C.6 shows how the COMSOL Multiphysics<sup>TM</sup> software discretized the domain using triangular elements with 3 layers of elements.

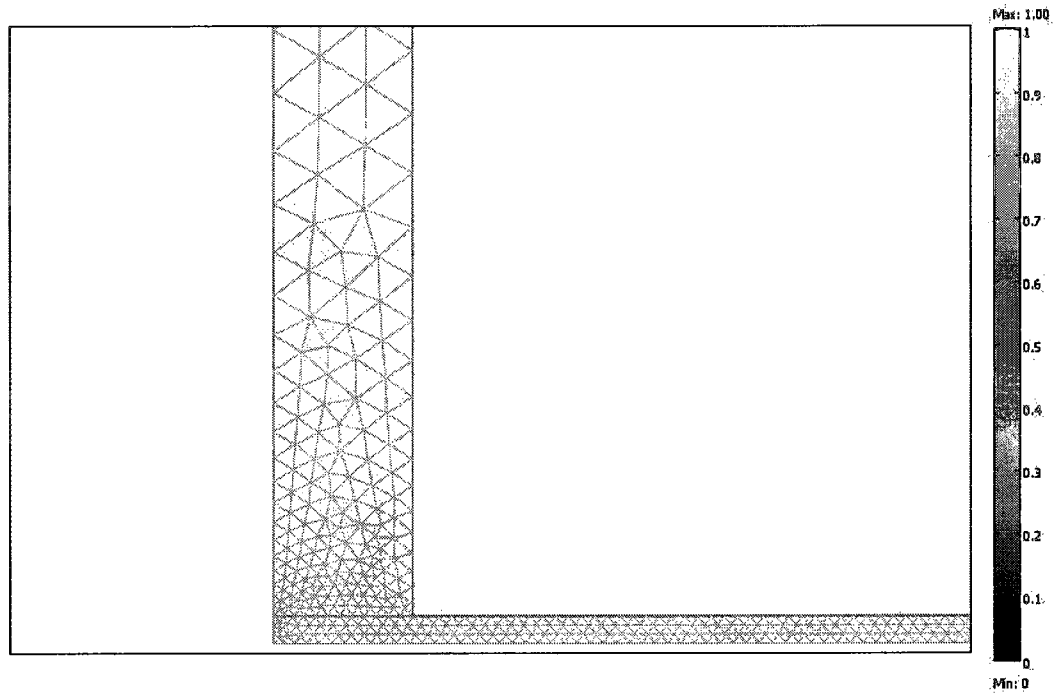


**Figure C.6.** Mesh used for all simulations in this thesis. Shaded colour scheme ranges from 1 (high quality) to 0 (low quality).